PONTIFICIA UNIVERSIDAD CATÓLICA DE CHILE
ESCUELA DE INGENIERÍA

COMPUTATIONAL MODELING OF CARDIAC ELECTROPHYSIOLOGY IN HEART FAILURE: AN IN-SILICO APPROACH TO UNDERSTANDING BIOMATERIAL INJECTION THERAPY

WILLIAM ALBERTO RAMÍREZ BENITEZ

Thesis submitted to the Office of Graduate Studies
in partial fulfillment of the requirements for the degree of
Doctor in Engineering Sciences

Advisor:
DANIEL HURTADO

Santiago de Chile, March 2021

PONTIFICIA UNIVERSIDAD CATÓLICA DE CHILE
ESCUELA DE INGENIERÍA

COMPUTATIONAL MODELING OF CARDIAC ELECTROPHYSIOLOGY IN HEART FAILURE: AN IN-SILICO APPROACH TO UNDERSTANDING BIOMATERIAL INJECTION THERAPY

WILLIAM ALBERTO RAMÍREZ BENITEZ

Members of the Committee:
DANIEL HURTADO
CRISTOBAL BERTOGLIO
DIEGO CELENTANO
DUVAN HENAO MANRIQUE
ALESSIO GIZZI
JUAN DE DIOS ORTUZAR

Thesis submitted to the Office of Graduate Studies
in partial fulfillment of the requirements for the degree of
Doctor in Engineering Sciences

Santiago de Chile, March 2021

Dedicado a mi madre Leticia y a mi esposa Ana María

ACKNOWLEDGEMENTS

Throughout this thesis and my Ph.D. development, I have received considerable support and assistance from many people.

I would like to thank first my supervisor, Professor Daniel Esteban Hurtado Sepúlveda, whose expertise and advice have been invaluable during these years working on this research. Your feedback on this thesis has been highly constructive and has substantially increased the quality of it.

I would like to acknowledge Professor Alessio Gizzi, from Università Campus Biomedico di Roma, for his valuable guidance and patient support throughout my internship. You provided me with many tools that I needed to choose the best direction and further my research.

I want to thank the committee members, Duvan Henao, Cristobal Bertoglio, and Diego Celentano, for their valuable suggestions. They have highly improved the final version of this thesis.

I would also like to thank my colleagues from the Computational Medicine Group for their extraordinary collaboration. You have been an excellent team to work with and have given me perfect moments to develop my university work.

In addition, I would like to thank my family, especially my mother and my wife, for their wise counsel and support. You have always been there for me and have given me much strength. Finally, I could not have completed this work without the encouragement of all my friends in Chile; too many to list here. You have provided me a tremendous stimulating company outside my research.

TABLE OF CONTENTS

ACKNOWLEDGEMENTS iv

LIST OF FIGURES viii

LIST OF TABLES x

ABSTRACT xi

RESUMEN xii

1. INTRODUCTION 1

2. ANATOMY AND PHYSIOLOGY OF THE HEART 7

2.1. Conduction system 7

2.2. Architecture of the ventricular myocardium 9

2.3. Action potential 10

3. MODELING CARDIAC ELECTROPHYSIOLOGY 13

3.1. Cellular electrical behavior 13

3.1.1. The cell membrane 14

3.1.2. The Nernst equilibrium potential 15

3.1.3. Current-voltage relation for the ion flux 16

3.1.4. Ion channel gating 16

3.1.5. The Hodgkin-Huxley model 18

3.1.6. Models for cardiac cells 19

3.1.7. The Fenton-Karma model 21

3.1.8. The ten Tusscher-Panfilov 2006 biophysical model 23

3.2. Mathematical models of cardiac tissue electrophysiology 24

3.2.1. The bidomain model 24

3.2.2. The monodomain model 29

3.3. Numerical solution of electrophysiology models 30

3.3.1. Operator Splitting method 31
3.3.2. Operator Splitting for the monodomain model 32
3.3.3. Spatial discretization: the finite element method 34
3.4. Subject-specific modeling of the heart 36
3.4.1. Image based anatomy 36

4. CARDIAC ARRHYTHMIA AND HEART FAILURE 39
4.1. Cardiac arrhythmia 39
4.1.1. Types of reentrant cardiac arrhythmia 39
4.1.2. Mechanisms of cardiac arrhythmias 39
4.1.3. Vortex filaments computation during fibrillation 40
4.2. Heart failure 42
4.2.1. Definition and incidence 42
4.2.2. Post myocardial-infarction heart remodeling in heart failure 43
4.2.3. Current therapies to Heart Failure 45
4.3. Biomaterial injection therapy 48

5. IN-SILICO STUDY OF ARRHYTHMOGENIC POTENTIAL OF BIOMATERIAL INJECTION THERAPY IN SWINE HEARTS UNDER HEART FAILURE 51
5.1. Methods 53
5.1.1. Geometrical and morphological representation of swine hearts 53
5.2. Numerical modeling of cardiac electrical activity 55
5.2.1. Simulation protocols and analysis 59
5.3. Results 61
5.4. Discussion 66

6. ON THE EFFECT OF IONIC MODELING IN THE DISPERSION OF REPOLARIZATION AND SUSTAINABILITY OF VENTRICULAR FIBRILLATION: A COMPARISON STUDY 72
6.1. Methods 75

6.1.1. The Fenton-Karma model 75
6.1.2. The TenTusscher-Panfilov 2006 model 76
6.1.3. Stimulation protocols and post-processing 77
6.2. Results 78
6.2.1. Dispersion of APD restitution 78
6.2.2. VF sustainability 79
6.3. Discussion 84

7. CONCLUSIONS 87

REFERENCES 89

APPENDIX 111
A. Appendix A 112
A.1. tenTusscher-Panfilov (2006) EP model equations 112

LIST OF FIGURES

2.1 Representation of the human heart 8

2.2 Representation of heart fibers 9

2.3 Action potential representation 10

2.4 APD_{90}, DI and CL definitions 11

2.5 Action potential heterogeneity 12

3.1 Cell membrane representation 14

3.2 Restitution curve 21

3.3 DT-MRI visualization 38

4.1 Filaments counting 41

4.2 Myocardial infarction stages 44

4.3 Cardiac resynchronization therapy 46

4.4 Surgical reshaping process 47

4.5 Myofiber stress 49

4.6 Biomaterial delivery process 50

5.1 Heart geometry and fiber directions 55

5.2 Heart with HF and biomaterial injections 55

5.3 Transmural heterogeneity in hearts 57

5.4 Control nodes in mesh for PDF approximation 58

5.5 Spatial distribution of APD, AT and RT 62

5.6 Restitution curve of control heart and HF hearts 63

5.7 Empirical PDF functions of regional APD 64

5.8 Temporal evolution of VF 65

5.9 Evolution of the number of filaments in VF 65

5.10 Number of filaments for heart with HF and biomaterial injections 66

6.1 S1S2 locations 78

6.2 Restitution quantification 81

6.3 Normalized PDF at CL=400 82

6.4 Ventricular Fibrillation evolution 83

6.5 FK and TP06 models: number of filaments 83

6.6 FK and TP06 models: pseudo-ECG computation 84

LIST OF TABLES

5.1 Parameter values used in VF simulations with the TP06 model 56

5.2 Initial conditions used in the TP06 model 57

6.1 FK parameters 76

6.2 Parameter values TP06 model for VF 76

6.3 Initial conditions used for the TP06 model 77

6.4 Normalization values for the APD 80

6.5 Number of filaments mean, maximum and minimum- VF 84

ABSTRACT

Computational cardiac electrophysiology is increasingly being used as a powerful tool for studying the electrical behavior of the heart, especially in pathological conditions such as heart failure. Recent advances in the acquisition of patient-specific geometrical and structural data have created the opportunity of applying numerical tools to investigate electrical abnormalities caused by ischemic heart disease. In conjunction with experimental and clinical trials, cardiac electrical activity simulations have provided a better understanding of the electrical attributes of cardiac disorders, making meaningful contributions to the enhancement of heart failure treatments. This progress is stimulated by the many achievements in the formulation of highly specialized electrophysiological models that have been able to describe the complex multi-scalar nature of the myocardium accurately. Despite this, the use of computational electrophysiology for the study of alternative therapies such as biomaterial injections and their influence in cardiac arrhythmia is still limited. Moreover, there are uncertainties about selecting an appropriate electrophysiological model in conjunction with complex subject-specific representations of the heart where computational demands and accuracy play an essential role in arrhythmia simulation. In this work, we study the influence of biomaterial injection therapy on the electrical behavior of infarcted hearts, using a highly optimized finite element code together with high-resolution MRI and DT-MRI data from swine. We concluded that although biomaterials may not affect the local restitutive properties of the myocardium, they may influence ventricular fibrillation sustainability. Finally, we compared two different electrophysiological models using the same subject-specific geometries, deducing that ventricular fibrillation dynamics can be reproduced using simplified ionic models with less demanding computational efforts.

Keywords: Computational electrophysiolgy, Biomaterial injection therapy, Ventricular Fibrillation, Myocardial Infarction

RESUMEN

La electrofisiología cardíaca computacional está siendo usada cada vez más como una herramienta eficaz para estudiar el comportamiento eléctrico del corazón, especialmente en condiciones patológicas como la falla cardíaca. Los avances recientes en la adquisición de datos geométricos y estructurales de corazones de pacientes especícificos ha creado la oportunidad de aplicar herramientas numéricas para investigar las anormalidades eléctricas causadas por enfermedad cardíaca isquémica. Junto con pruebas experimentales y clínicas, la simulación de la actividad eléctrica en el miocardio ha establecido un nuevo paradigma para entender las características eléctricas de las enfermedades cardíacas, haciendo contribuciones significativas al mejoramiento de sus tratamientos. Todo este progreso ha sido estimulado por la basta cantidad de logros en la formulación de modelos eletrofisiológicos altamente especializados que han ayudado a describir de forma precisa el complejo comportamiento eléctrico del miocardio. Sin embargo, el uso de la electrofisiología computacional para el estudio de terapias alternativas, como lo son las inyecciones de biomateriales en casos de arritmia cardiaca, es aún limitado. Además de esto, existen incertidumbres sobre los modelos numéricos apropiados para la simulación de la propagación eléctrica en corazones de sujetos específicos, donde las demandas computacionales y la precisión juegan un rol muy importante. En esta tesis se estudia la influencia de la terapia de inyección de biomateriales en el comportamiento eléctrico de corazones con infarto, usando un código de elementos finitos altamente optimizado en combinación con datos de alta resolución de corazones porcinos tomados de resonancia magnética. De este trabajo se concluye que aunque las inyecciones de biomateriales parecen no afectar las propiedades restitutivas locales del miocardio, sí pueden influir en la sostenibilidad de la fibrilación ventricular. Finalmente, en esta tesis se comparan dos modelos electrofisiológicos diferentes usando los mismos datos de sujetos específicos y se concluye que la dinámica de la fibrilación ventricular puede reproducirse usando modelos iónicos simplificados, disminuyendo la demanda computacional.

1. INTRODUCTION

During many millenia the heart, its function, and its diseases have played a critical role in the history of science. According to (Katz, 2008), descriptions of heart diseases can be already encountered in ancient Greek and Roman texts. Katz affirmed that it was during the third century BCE when it was recognized, by Herophilus and Erasistratus, that the heart contracts and the function of the semilunar valves were understood. After that, as reported by (Lüderitz, 2009) , throughout the late 19th and 20th centuries, many advances in the understanding of the heart function and its pathophysiology were accomplished. To some extent, this could be achieved as a result of the discovery of the cardiac conduction system . However, according to Lüderitz, it was not after the 1960s when the mechanics of heart muscle contraction, relaxation, and excitation-contraction were elucidated. In the last decades, the uncovering of heart function mechanisms continues as a predominant topic of study in the scientific community, principally motivated by its clinical relevance. However, there are still many open questions regarding heart function, particularly in pathological conditions such as heart failure (HF).

As reported by the American Heart Association (AHA) in 2019, cardiovascular diseases are the most frequent cause of death worldwide, and they are expected to increase in the next decades (Benjamin et al., 2019). The same report informs that in 2008, 30% of all global deaths were due to heart diseases, stroke, and other cardiovascular diseases. Solely in the United States (US), cardiovascular diseases have substantial personal and financial impacts. For instance, HF cost in the US is projected to be 69.7 billion dollars by 2030, representing approximately 244 dollars for every US adult. Benjamin *et al* also informed that even though survival after diagnosis of heart disease has improved over time with better treatments and dedicated devices, 50% of people die within five years after diagnosis. Moreover, for some patients with severe, progressive HF, transplant is the only viable option. The development of new techniques for the diagnosis and treatment of heart diseases is necessary to manage the severe threat represented by this illness. Therefore, a better

understanding of heart function at both normal and pathological conditions is required.

The heart acts as a pump, delivering oxygenated blood to the organs by using a highly synchronous cycle of contraction-relaxation process of about 10^{10} muscle cells. A complex propagation of electrical waves controls this process. Abnormal electrical activity of the heart can lead to severe medical conditions, and most of the heart problems either results from or cause disturbances of the electrical activity (Weiss, Garfinkel, Karagueuzian, Chen, & Qu, 2010; Zhou, Bueno-orovio, & Rodriguez, 2018; Roberts, Yang, Behrens, Moreno, & Clancy, 2012). These disturbances are called cardiac arrhythmias. Among the most dangerous cardiac arrhythmias are the reentrant ventricular arrhythmias, namely ventricular tachycardia (VT) and ventricular fibrillation (VF). In the former, cardiac contraction rate increases considerably and, in the latter, contraction becomes completely disorganized, developing a chaotic electrical activation (Jalife, 2000). The link between cardiac contraction and electrical propagation led to the development of techniques to measure the electrical activity of the heart as a way to diagnose heart problems. For instance, the electrocardiogram, or ECG, is the oldest non-invasive tool for diagnosing heart conditions. This technique is a surface recording of the electrical potential differences that results from the electrical activity of the heart (Oresko et al., 2010). When the electrical activity is disturbed, the potential differences change in characteristic patterns, allowing the recognition of abnormalities (Sundnes et al., 2007).

During the last decades, vast knowledge about the electrical activity of the heart has been accumulated (N. A. Trayanova & Chang, 2016a). We have now many insights of how the heart works at a multiscale level: a small scale where bioelectrochemical phenomena regulate the processes occurring at cellular and sub-cellular level, and a large scale where processes of electrical activation are seen at tissue and organ level (Sahli Costabal, Yao, & Kuhl, 2018). Even so, many mechanisms are not entirely understood. The knowledge about how the interaction of the billions of small-scale processes occurring in the cell

membrane affects the electrical activity at tissue and organ level is minimal. Research on computational and mathematical modeling of cardiac electrophysiology has been increasingly intensified since it has shown to bee a promising technique to expand our knowledge and predictability in the field (Sahli Costabal et al., 2019; Ferrero, Trenor, & Romero, 2014; Pathmanathan & Gray, 2018). With this tool, the electrical activity of the heart can be investigated by using detailed and precise cellular models that describe phenomena at microscopic levels in combination with homogenized macroscopic tissue and organ models. These models can be validated later by comparing simulated results with experimental *in vitro* and *in vivo* data to improve multiscale models or to redesign experiments. Moreover, electrophysiological models are being integrated into mechanical models of myocardial tissue deformation, hemodynamics models and in general with models of the cardiovascular system (Franzone, Pavarino, & Scacchi, 2014; Quarteroni, Lassila, Rossi, & Ruiz-Baier, 2017).

Simplified cardiac setups, such as tissue samples with regular geometry, are often simpler and less expensive to model and simulate than real heart models (Sundnes et al., 2007). Although several achievements have been accomplished during the last years in the field of computational electrophysiology, there is still a large need for further model development and validations before they can be extensively used in clinical applications (Niederer, Lumens, & Trayanova, 2019). It is crucial to overcome several computational and mathematical issues that are still present in the numerical modeling of cardiac electrical activity. Many of these issues are related to computational efficiency: current large scale simulations of whole-heart beats require highly specialized numerical tools in order to reduce their intense computational cost. Moreover, parameters from clinical data are still limited given the complex and multiscale nature of electrical propagation within the myocardium, particularly when dealing with cardiomyopathies such as cardiac ischemia (Gray & Pathmanathan, 2018; Barone, Fenton, & Veneziani, 2017). Closely related to this is the need for better mathematical descriptions of the biophysical nature of electrical

propagation within the myocardium (Clayton et al., 2011).

The vast literature about computational models in cardiac electrophysiology and the advances in image acquisition techniques, such as magnetic resonance imaging (MRI), has made it possible to simulate complex mechanisms leading to cardiac arrhythmogenesis using highly-detailed anatomical models of the heart (N. A. Trayanova & Chang, 2016a; Witzenburg & Holmes, 2017). Through MRI-based animal and human ventricular geometries, several computational studies have uncovered the mechanisms of electrical excitation wakebreaks and the onset of cardiac arrhythmias, such as VT and VF, especially in hearts with serious diseases such as myocardial infarction (Zhou et al., 2018; H. J. Arevalo et al., 2016; N. A. Trayanova & Chang, 2016b; Roberts et al., 2012; Karma, 2011; Benson, Ries, & Holden, 2007). This *in-silico* approach has been used to develop quantitative measures for vulnerability to VT, which have been validated in clinical applications using optical mapping techniques (Christoph et al., 2018; Walton et al., 2014). The capabilities of computational models to predict the electrical behavior of hearts with infarction has been demonstrated, particularly in the development of alternative treatments such as cell-based myocardial repair (Yu et al., 2019). Nevertheless, the are several prospective treatments that have no been addressed yet with computational tools. This is the case of biomaterial-injection treatments (Choy et al., 2018; Ruvinov & Cohen, 2016; Lee et al., 2015), a topic that is widely investigated in this thesis.

Non-linear reaction-diffusion models are usually adopted to study the propagation of bioelectrical waves within the myocardium (D. Hurtado & Henao, 2014; Göktepe & Kuhl, 2009). Many numerical approaches have been implemented to solve this set of equations, predominantly finite difference schemes , finite volume schemes, and finite element schemes (Dupraz, Filippi, Gizzi, Quarteroni, & Ruiz-Baier, 2015; Abbasi & Clayton, 2013; Göktepe & Kuhl, 2009; Pathmanathan, Mirams, Southern, & Whitheley, 2011).

The implementation of these methods usually requires homogenization techniques to address the spatial multiscale nature of the problem (Peñaranda, Cantalapiedra, Bragard, & Echebarria, 2012). From the literature, it is known that meshes with small representative sizes are required due to accuracy constrains. Moreover, several time-integration techniques to address the different time scales are used, especially in biophysical-based mathematical models where several state variables are represented at the cell level (Franzone, Deuflhard, Erdmann, Lang, & Pavarino, 2006). Explicit Euler methods and variants of these time-integration techniques have shown to be suitable for whole-organ simulations, where the system of equations is extensive. However, these sorts of techniques are highly restricted by the time step bounds that arise due to the mesh size constraints. Phenomenological models have been developed to tackle this problem (F. Fenton & Karma, 1998; Bueno-Orovio, Cherry, & Fenton, 2008; Tusscher, Hren, & Panfilov, 2007; FitzHugh, 1961). These models have the property of simulating the electrical properties accurately at cell and tissue levels with fewer state variables compared with biophysical-based models. This is an advantage when running large scale simulations. However, they can not be used to model the behavior of particular ionic currents that may be relevant in several applications, such as drug induced electrophysiological imbalances (ten Tusscher & Panfilov, 2006).

In this thesis, we first investigate the electrical behavior and arrhythmic vulnerability of hearts treated with alginate-based biomaterial injections employing a computational modeling approach. To this end, we used data from high-resolution MRI and diffusion tensor magnetic resonance imaging (DT-MRI) of hearts treated with biomaterials to create a computational model that represents the normal and deceased biventricular cardiac anatomy as well as the myocardial fiber orientations. In addition, using the same subject-specific heart data, we compare phenomenological and biophysical electrophysiology models in the prediction of VF under different scenarios, and evaluate the advantages of employing phenomenological models to asses complex electrical behavior.

This thesis is structured as follows: first, we briefly describe the anatomy and physiology of the heart, making emphasis in its electrical conduction system. Secondly, we introduce the modeling aspects of cardiac electrophysiology, going from the characterization of cellular activity to the description of electrical propagation within the myocardial tissue. Following this, we introduce the mathematical and numerical modeling of cardiac electrophysiology using the finite element method (FEM). In addition, we give an outlook of subject-specific modeling of the heart, making emphasis on MRI and DT-MRI data acquisition prospects. After this, we discuss about cardiac arrhythmia and heart failure, making emphasis in types of cardiac arrhythmia and their mechanisms of action, as well as incidence and current therapies for HF and its relation with cardiac arrhythmia. Later, the application of computational electrophysiology for the study of the electrical vulnerability of biomaterial-treated hearts is addressed in sect. 5. Finally, in sect. 6, we introduce the comparative study on the effect of phenomenological and byphisical electrophysiological models on the dispersion of repolarization and VF behavior. We close this work in sect. 7 by highlighting the main conclusions of this study, as well as discussing future perspectives.

2. ANATOMY AND PHYSIOLOGY OF THE HEART

2.1. Conduction system

The mammalian heart is a muscular organ composed of four chambers: the left and right atria and the left and right ventricles. Its function is to supply the body with oxygen and nutrients through the blood flow by periodic contractions and relaxations. The right atrium and ventricle act as a pump for the pulmonary circulation system, whereas the left atrium and ventricle act as a pump for the systemic circulation. Atria and ventricles are separated by the atrioventricular septum, which contains the tricuspid valve on the right side and the mitral valve on the left side. The right ventricle is connected to the pulmonary artery via the pulmonary valve, and the left ventricle is connected to the aorta via the aortic valve (Figure 2.1). The walls of the different parts of the heart have different thicknesses. The atria walls are thin ($<$2 mm), because they have to produce a pressure difference of only 20 mmHg. The ventricles walls are thicker (right: ca. 10 mm, left: ca. 20 mm), since they generate about 30 mmHg of pressure difference in the right ventricle and approximately 50 mmHg in the left ventricle.

For an effective pumping in this four-chambered organ, a number of processes take place. First of all, there is a synchronous contraction of the left and right atria to deliver blood to the ventricles. An electrical signal, called action potential, regulates this contraction. The action potential is propagated by the cardiac muscle cells (cardiomyocytes) due to a complex intracellular and extracellular ionic kinetic interaction. Neighboring cells are electrically coupled via the so-called gap junctions, allowing the flux of ions between cells. The electrical connection between cells leads to virtually synchronous contraction of the cardyomiocytes. Under normal conditions, the excitation wave starts at the sino-atrial (SA) node, located on the right atrium. The SA node is composed of pacemaker cells, that are electrically active and produce spontaneous action potentials without the need of external stimuli. Heart rate is regulated via frequency changes of the SA node and the transmission rate of the atrio-ventricular (AV) node (Alonso, Bar, & Echebarria, 2016).

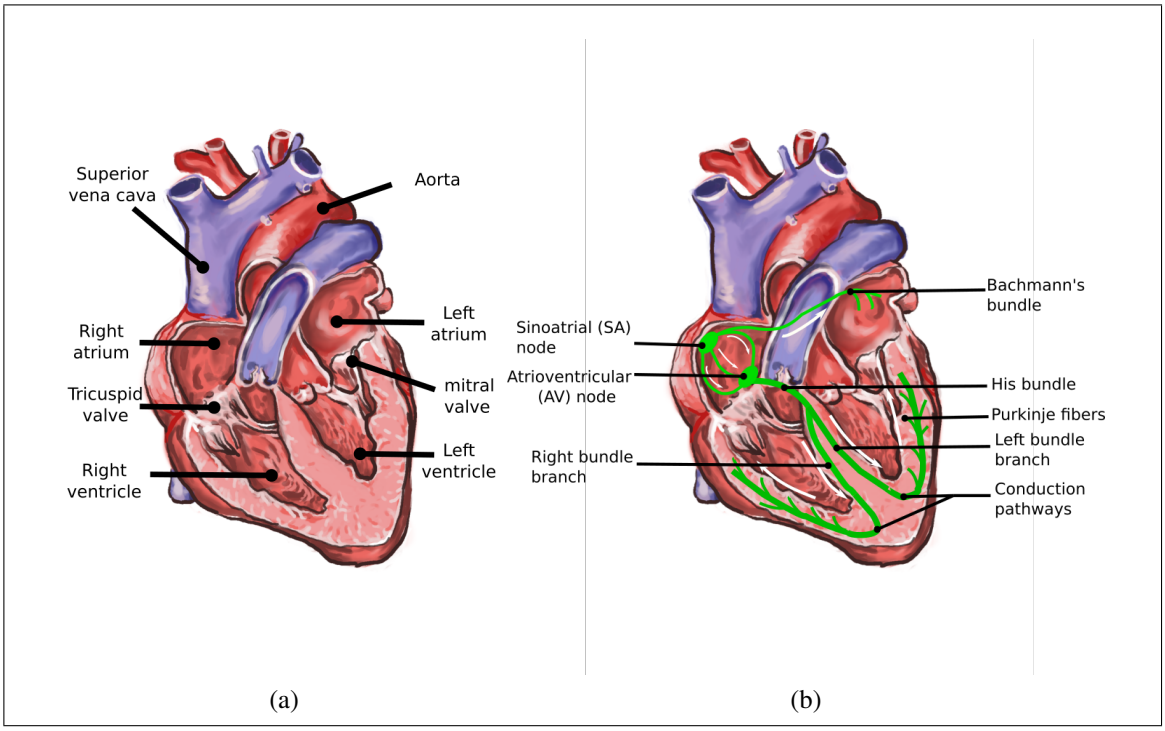

Figure 2.1. Representation of the human heart.(a) Heart anatomycal subdivision and (b) representation of the electrical conduction system. The action potential travels from the the SA node to the AV node and ends at the ventricles through the His bundle. This highly synchronized excitation path allows an optimal contraction of atria and ventricles.

Atrial contraction is achieved once the electrical wave travels outward the SA node, exciting all atrial cells. The atria and ventricles are separated by a non-conductive layer except at the AV node, allowing a delay between atrial contraction and ventricular contraction. This delay is necessary given that the ventricles must contract after being filled with blood supplied from the atria. The AV node reduces the propagation velocity to achieve the required delay. From the AV node, the action potential is propagated to the common bundle, or His bundle, the left and right bundle branches, and the Purkinje fibers, which end on the endocardial surface of the left and right ventricular wall and septum. The action potential propagates through the ventricles, initiating ventricular contraction and an efficient pumping of blood through the bloodstream. Cardiac output is adapted to the oxygen demands of the organism through the autonomous nervous system. Contraction force is

regulated by adapting intracellular calcium handling and restitution properties of the tissue (Seemann, 2005).

2.2. Architecture of the ventricular myocardium

The heart ventricles exhibit a complex three dimensional spatial organization of their reinforcing fibers (see Figure 2.2). As it was described above, the cardyomiocites are mostly connected end-to-end via gap junctions forming cardiac fibers with varying orientation. These fibers orientation changes smoothly between the endocardium and the epicardium. Moreover, cardiac fibers also have an aditional spatial organization that consists in laminar muscle sheets, typicaly 4-6 myocytes thick, changing radially from the epicardium to the endocardium. These sheets are separated with connective tissue and gaps called cleavage planes. At any given point of the myocardium $\mathbf{x}$ it is possible to

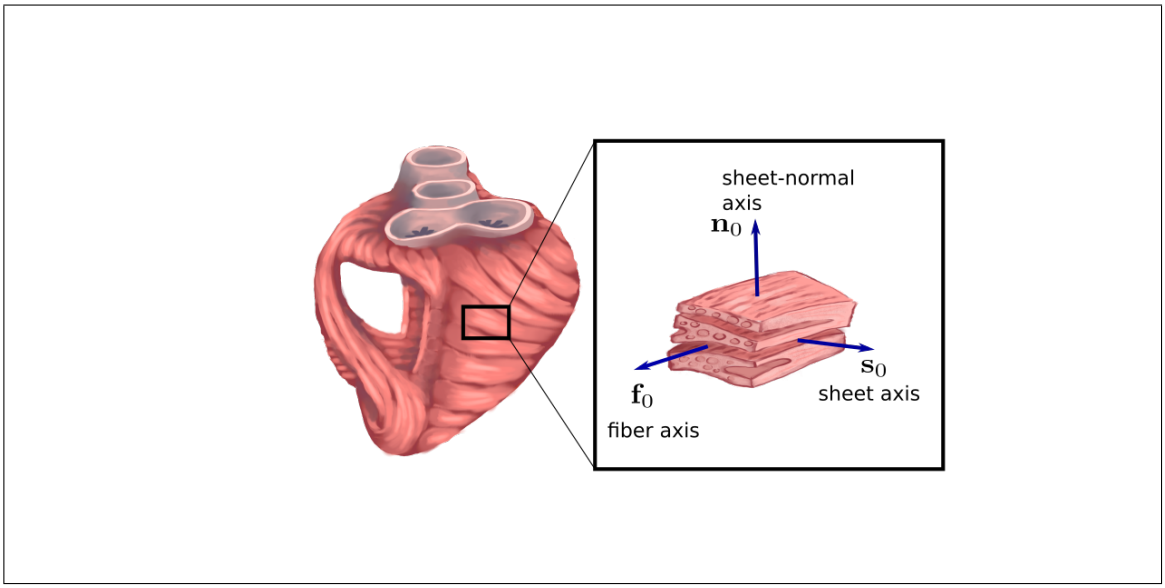

Figure 2.2. Representation of the ventricular fiber spatial distribution and the orthogonal principal axes related with the fibers direction. Adapted from (Holzapfel & Ogden, 2009)

identify a triplet of orthogonal principal axes $\mathbf{f}_0(\mathbf{x})$, $\mathbf{s}_0(\mathbf{x})$ and $\mathbf{n}_0(\mathbf{x})$, where $\mathbf{f}_0(\mathbf{x})$ corresponds to the direction parallel to the fiber direction, while $\mathbf{s}_0(\mathbf{x})$ and $\mathbf{n}_0(\mathbf{x})$ correspond to

the tangent and orthogonal to the radial laminae, respectively, and both being transverse to the fiber axis. See 2.2 for an schematic representation of the fibers architecture and the orthogonal principal axes.

2.3. Action potential

The contraction process of the heart is regulated by an electrical signal called action potential. The excitation of cardiac cells causes a rapid variation of the potential difference across the cell membrane, the so-called transmembrane potential. If the stimulus is strong enough, the transmembrane potential rapidly goes from a negative resting value to a value above zero (*depolarization*), remains around this value for a given period of time (plateau) and then returns to the resting value (*repolarization*). The elapsed time between depolarization and repolarization is the so-called action potential duration (APD). A representation of an action potential is showed in Figure 2.3.

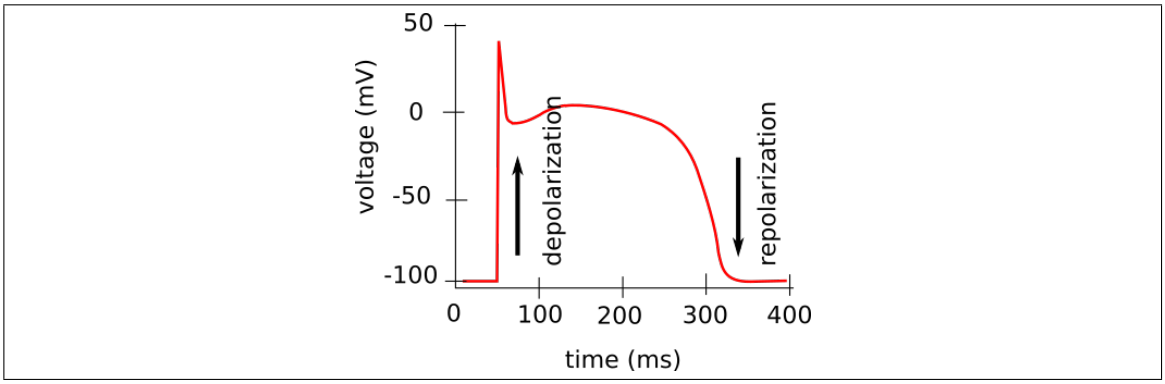

Figure 2.3. Action potential representation using the Winslow model for the canine heart (Winslow et al., 1999)

Maps of the activation and recovery sequences provide important information about normal heart activity and cardiac arrhythmias that are often associated with abnormal APDs and recovery times (Hill et al., 2016). Methods for determining the activation and recovery times within the myocardium are essential tools in clinical and experimental applications. Widely used in the study of cardiac electrophysiology are the concepts of late

activation time (AT_{90}) and the late recovery time (RT_{90}) which are markers defined as the instant in which the transmembrane potential reaches 90% of its resting value during an activation or recovery state. Related with these is the action potential duration (APD_{90}) which is defined as $APD_{90} = RT_{90} - AT_{90}$. Given a set of consecutive action potential waves, the time period between two stimuli consist of two segments, the ADP and the diastolic interval (DI). Therefore, the late cycle length (CL_{90}) is expressed as $CL_{90} = APD_{90} + DI_{90}$ (see Figure 2.4). For numerical applications in which a high number of degrees of freedom are needed (i.e., whole heart simulations), the estimation of these markers may represent a considerable part of the computational time.

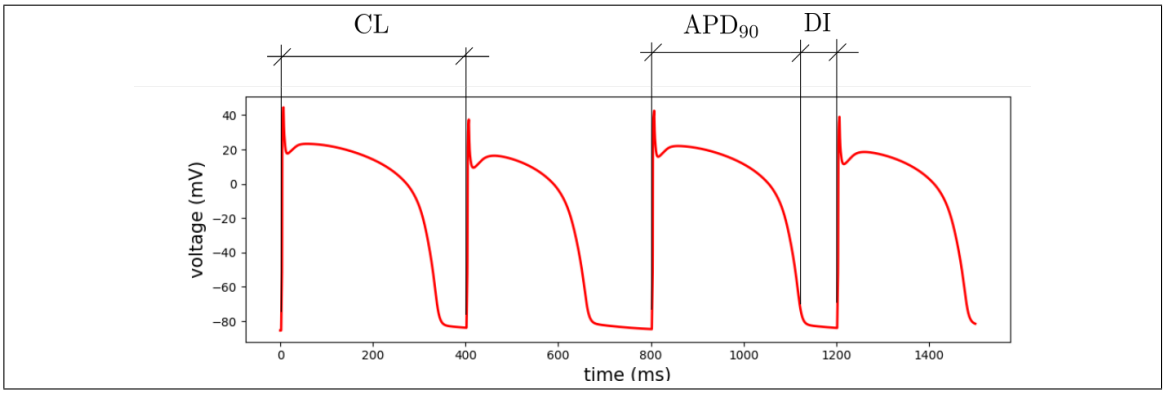

Figure 2.4. APD_{90}, DI and CL from a single cell simulation of action potential using the ten Tusscher-Panfilov electrophysiological model (ten Tusscher & Panfilov, 2006), with a stimulation frequency of 400 ms.

Cardiac action potentials differ significantly in different regions of the heart (see Figure 2.5), as action potentials in the atria, the ventricles and in specialized conduction myocites exhibit different shapes and duration. Furthermore, myocytes with different AP morphologies are encountered within the endocardium, epicardium and midmyocardium (M-cells) regions (transmural heterogeneity) and along the apex-to-base direction (apex-to-base heterogeneity). These heterogeneities affect the propagation of the electrical stimulus within the heart, specially the sequence of repolarization, leading to the concept of APD dispersion. Transmural dispersion of the APD has been found in several animal species, with

shorter APD in subepicardial and subendocardial cells and with the longest APD in mid-myocardial cells. Transmural heterogeneity is related with the expression of some ionic channels, in particular the sodium channel (I_{Na}), the slow and rapid delayer potassium channels (I_{Kr}, I_{Ks}) , the transient net outward current channel (I_{to}), and the Na^{+}/Ca^{2+} exchanger. In addition to spatial dispersion of APD, temporal dispersion may also occur during beat-to-beat changes.

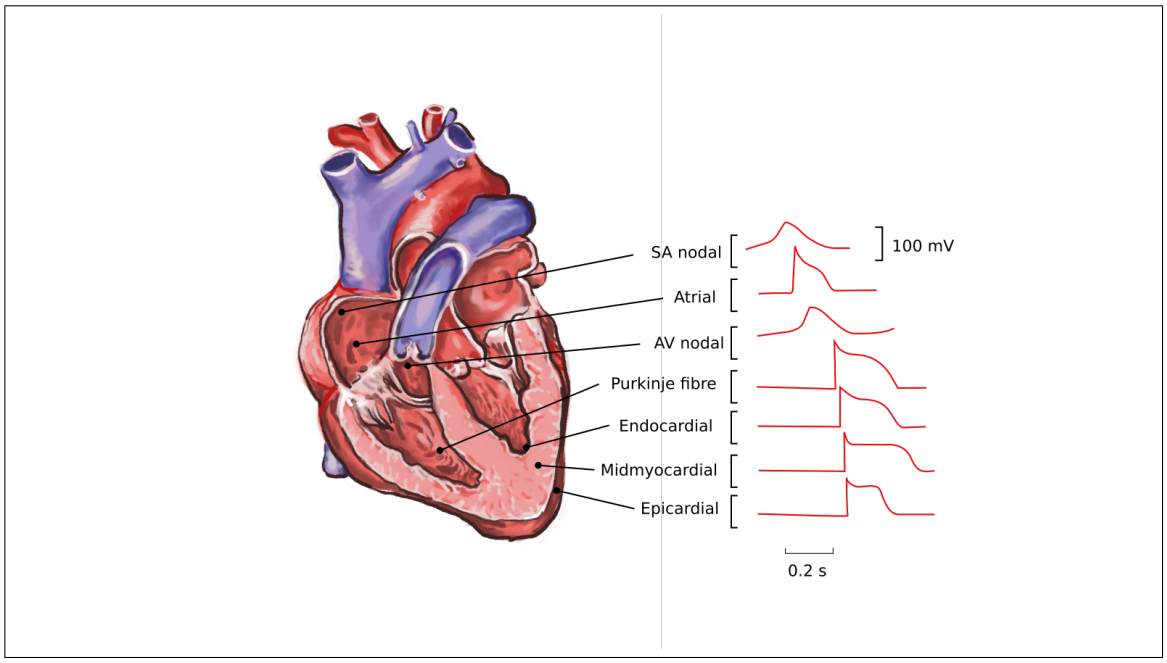

Figure 2.5. Action potential morphology for different regions of the heart. Referenced from (Franzone et al., 2014)

3. MODELING CARDIAC ELECTROPHYSIOLOGY

3.1. Cellular electrical behavior

There are a number of models for the study of cardiac activation and repolarization. They are usually grouped into three categories:

- Phenomenological models, which are simple models that reproduce the macroscopic properties of cell behavior. This models are usually polynomial functions that approximate the ionic current and state variables that drives the evolution of the system.
- First-generation biophysical models: these models attempt to approximate the observed cellular behavior and the underlying physiology. They describe the most important ionic currents using a simplified formulations of the underlying physiological details.
- Second-generation biophysical models: they offer a very detailed description of the physiology of the cells. Based on advanced experimental techniques they enable a high detailed small-scale representation of cell physiology.

Pure phenomenological models offer significant advantages from a computational point of view, as they typically consider a few variables (typically less than 4) and evolution equations. The small dimensionality of these models make them very efficient in the numerical simulations of the heart. In contrast, biophysical models employ a larger number of variables and evolution equations (in the order of tens) that are stated based on ionic and subcellular mechanisms. This larger dimensionality implies a considerably higher computational cost in the solution of biophysical models.

For a single cell all the charge transported by the ionic current accumulates at the membrane producing and varying the transmembrane potential v. This is described by the balance equation

$$C_m \frac{dv}{dt} = -I_{ion} + I_{app}, \tag{3.1}$$

where I_{ion} is the sum of ionic currents and I_{app} is an applied stimulus current, which is used to trigger the action potential of the cell.

3.1.1. The cell membrane

The cell membrane is a lipid bilayer that provides a boundary separating the internal workings of the cell from its external environment. It is selective permeable, allowing the free transfer of some materials and restricting the transfer of others. The cell membrane also contains protein-lines pores, called ion channels, that allows specific ions to travel through them by a passive process, controlled by their concentration gradient. This concentration gradient produce a potential difference, the *transmembrane potential*, that in conjunction with the channel structure drives the ionic currents. This is a fundamental topic in molecular biophysics and the regulation of such ionic currents is one the most extensively studied problems. Moreover, the modulation of the transmembrane potential is one of the most important ways in which cells control their behavior or communicate with other cells. The primary ions that flows through the ion channels for cardiac cells are Na^{+}, K^{+}, Cl^{-}, and Ca^{2+}

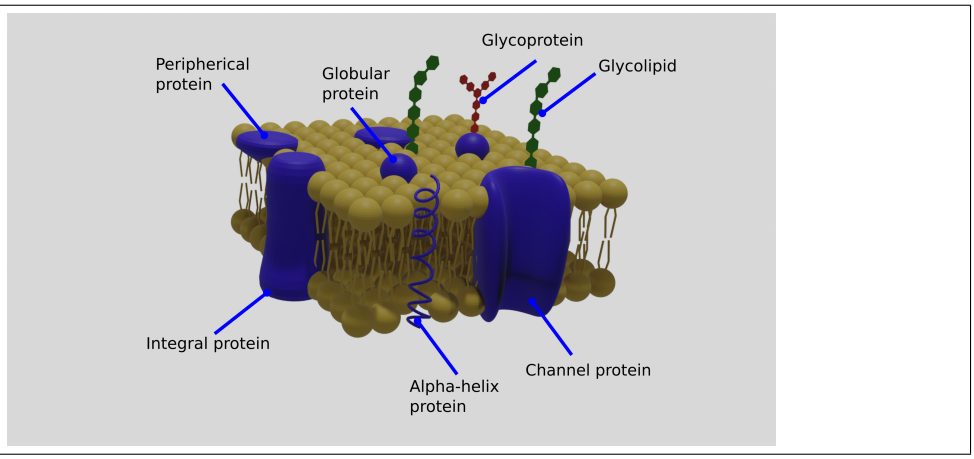

Figure 3.1. The cell membrane is a lipid bilayer composed by channel proteins that are selective permeable, allowing the ions transport through the membrane (modified from (Keener & Sneyd, 2009)).

3.1.2. The Nernst equilibrium potential

In general, the flux across the membrane of a generic ion K with valence z is the sum of the diffusion flux $\mathbf{J}_D$ and the electric flux $\mathbf{J}_E$. The constitutive law that describes this total flux is known as the Nernst-Planck equation, defined as

$$\mathbf{J} = \mathbf{J}_D + \mathbf{J}_E = -D\left(\nabla c + \frac{zF}{RT}c\nabla u\right). \tag{3.2}$$

Here, D is the diffusion coefficient, c is the ion concentration, F is the Faraday's constant, R is the ideal gas constant, T is the temperature, and u is a scalar potential. For the cell membrane it is natural to assume that the variations in potential concentration occur only in one direction across the membrane. Then, the flow of ions can be view as the one dimensional relation

$$J = -D\left(\frac{dc}{dx} + \frac{zF}{RT}c\frac{du}{dx}\right). \tag{3.3}$$

When the total flux **J** is zero then $J_D = -J_E$ and

$$\frac{1}{c}\frac{dc}{dx} + \frac{zF}{RT}\frac{du}{dx} = 0, \tag{3.4}$$

Supossing that the cell membrane extends from $x = 0$ (inside) to $x = L$ (outside) and using subscripts i and e to denote internal and external quantities respectively. Then, integrating equation (3.4) from $x = 0$ to $x = L$ results in

$$ln(c)|_{c_i}^{c_e} = \frac{zF}{RT}(\phi_i - \phi_e), \tag{3.5}$$

and thus the potential difference across the membrane $v = \phi_i - \phi_e$ that gives zero flux is given by the so-called Nerst equilibrium (or reversal) potential

$$v_{eq} = \frac{RT}{zF}ln\left(\frac{c_e}{c_i}\right). \tag{3.6}$$

This derivation is based on the constitutive Nernst-Plack equation. However this equilibrium potential can be also derived from thermodynamical assumptions, showing the universal character of the Nernst potential.

3.1.3. Current-voltage relation for the ion flux

Although we are able to derive the Nernst equilibrium potential from the Nernst-Planck equation and even from thermodynamic considerations, there is no universal expression for the ionic current (Keener & Sneyd, 2009). For instance, an expression for the Na^+ current cannot be derived from thermodynamic principles and depends on the particular model selected to describe the Na^+ channels. However, any expression for the passive ionic flux should at least satisfy the equilibrium equation (3.6) given zero flux. In a simple model, the Na^+ current across the cell membrane can be assumed to be a linear function of the transmembrane potential. Thus

$$J_{Na} = G_{Na}(v - v_{Na}) \tag{3.7}$$

where v_{Na} is the equilibrium potential of Na^+ and G_{Na} is the permeability of the membrane for Na^+. G_{Na} may be constant or a function of time, membrane potential and, in some cases, ionic concentrations.

3.1.4. Ion channel gating

As described before, ion channels that open and close in response to an electrical stimulus are essential in the behaviour of excitable cells. The mechanisms by which these channels open and close are very complex. Here, we focus on models that describe the channels to be composed of several sub-units. Each sub-unit may be either open or closed. We denote the concentration of channels in the open state and closed state as $[O]$ and $[C]$, respectively. Moreover, if we assume that the total concentration of channels $[O] + [C]$ is constant, then the change between the open and closed state may be expressed as

$$C \underset{\beta}{\overset{\alpha}{\rightleftarrows}} O,$$

where α is the rate of opening and β is the rate of closing. Generally, this rates depend on the transmembrane potential v. In a reaction of this kind, by the law of mass action, the rate of change from one state to another is proportional to the concentration of channels in

one state. Then, we get

$$\frac{d[O]}{dt} = \alpha(v)[C] - \beta(v)[O]. \tag{3.8}$$

Usually, this equation is divide by the total concentration $[O] + [C]$ to give

$$\frac{dg}{dt} = \alpha(v)(1 - g) - \beta(v)g, \tag{3.9}$$

where $g = [O]/([O]+[C])$ is the proportion of open channels. g may be also viewed as the probability that the channel is open. As most channels consist of several subunits, which may all be either open or closed, then this equation may be also viewed as the probability for each subunit being open.

Assuming complete independency of each subunit, the probability that a channel is open is equal to the product of the probability for each subunit of being open (Keener & Sneyd, 2009). Then, for a channel that consist on n equal subunits, the probability O that the channel is open is given by

$$O = g^n. \tag{3.10}$$

From the definition we have that $O, g \in [0, 1]$. Moreover, a channel may consist in several different subunits. In that case the behavior of each subunit is modeled using equation 3.9. For instance, if a channel consist on two subunits with probabilities g for one subunit and h for the other, each probability have different α and β functions. Then, the probability that the channel is open is given by

$$O = g^m h^n. \tag{3.11}$$

Once the channels dynamics is established we can compute the current through the membrane as the product of maximum current, i.e., the current we would have if all the channels were open, and the proportion of open channels. For instance, the linear model defined before for the Na^+ current may expressed as

$$I_{Na} = G_{max_{Na}} O(v - v_{eq}) \tag{3.12}$$

where O is defined as products of the form (3.10) or (3.10), v_{eq} is the equilibrium potential for the specific ion, and G_{max} is the maximum conductance (i.e., conductance with all channels opened). Apart from the channel-gating models described here, there are other types of models which are not based on the same assumptions, i.e., subunit state independence.

3.1.5. The Hodgkin-Huxley model

As already stated, the primary ions that flows through the ion channels in cardiac cells are Na^+, K^+, Cl^-, and Ca^{2+}. A model for the total ionic current across the membrane can be constructed by using an expression for each current of the form (3.12). A model of this kind was first proposed in 1952 by Hodgkin and Huxley (HH). They provided a the description of the action potential for the squid giant axon. Although this model is not directly related with the myocardium, it served as the base for the construction of cardiac cell models. The HH model considers the total ionic current as the sum of three contributions; a Na^+ current (I_{Na}), a K^+ current (I_K) and an unespecified current called a leakage current (I_L). These currents are described as

$$I_{Na} = \bar{g}_{Na} m^3 h(\nu - \nu_{Na}) \tag{3.13}$$

$$I_K = \bar{g}_K n^4 (\nu - \nu_K) \tag{3.14}$$

$$I_L = \bar{g}_L (\nu - \nu_L). \tag{3.15}$$

Here, v is the deviation from the resting potential, defined as $\nu = v - v_{eq}$. Equivalently, $\nu_{Na} = v_{Na} - v_{eq}$, $\nu_K = v_K - v_{eq}$ and $\nu_L = v_L - v_{eq}$ are shifted equilibrium potentials. Besides, m, h and n are gate variables represented by equations of the form 3.9, and $\bar{g}_{Na}$, $\bar{g}_K$, and $\bar{g}_L$ are the maximum conductances for each current. The total ionic current is then represented as

$$I_{ion} = I_{Na} + I_K + I_L. \tag{3.16}$$

Inserting this last expression into the single cell equation 3.1, we get that the rate of change of the membrane potential becomes

$$C_m \frac{dv}{dt} = -\bar{g}_{Na} m^3 h(v - v_{Na}) + \bar{g}_K n^4 (v - v_K) + \bar{g}_L (v - v_L), \tag{3.17}$$

with the gate variables given by equations of the form

$$\frac{dg}{dt} = \alpha_g(v)(1 - g) - \beta(v)g, \tag{3.18}$$

for $g = m, h, n$. The rate functions α_g and β_g, specified in Appendix A, enforce a functional dependence on the membrane potential necessary for experiment reproduction.

3.1.6. Models for cardiac cells

Although the HH model can reproduce depolarization and repolarization of the cell and tissue, it does not provide a good approximation to the electrical behavior of cardiac cells. The first model that describes the action potential in cardiac cells was proposed in 1962 by Noble. This model is based on the HH equations, but the parameters have been set to approximate action potential of the Purkinje cells (Noble, 1962). The first model to describe ventricular cells was that of Beeler and Reuter in 1977 (Beeler & Reuter, 1977). In this model, the role of calcium plays a fundamental role since it is essential for the contractile mechanism of the muscle cells. It is based on experimental data from the guinea pig, and it is still widely used, given its simplicity compared with more recent models. Another broadly used ventricular cell model is the Luo-Rudy model (Luo & Rudy, 1991), which is a extension of the Beeler-Reuter model, and include six ionic currents, controlled by seven gate variables. In 1994, Luo and Rudy published a substantial upgrade of their previous model, known as the Luo-Rudy phase two model, with a more detailed description of the specific ionic currents across the membrane (Luo & Rudy, 1994). Moreover, this model included important internal fluxes, such as the calcium flux of the *sarcoplasmic reticulum* (SR), as well as the buffering of calcium. Although this model presented a very

detailed description of the ventricular cell, several models have been proposed since then, in which different processes are managed in a different way.

An important characteristic of the electrical behaviour of cardiac cells is the electrical restitution. In basic terms, this characteristic is a functional relationship between the action potential duration (APD) and the length of the diastolic interval (DI) preceding it. In many cases, this relationship is characterized by small changes in the APD for a broad range of long DIs and shortening of the APD at shorter DIs. Therefore, restitution may be seen as a form of adaptation to changes in rate (see Figure 3.2 (a)). If this adaptation does not take place and the APD is constant regardless of the heart rate, this would result in a blockade of the heart beat so contractions are skipped when the heart is beating extremely rapid (i.e., intensive physical activity). The heart ability to adapt to different heart rates allows an adequate contraction and pumping of blood under a wide range of physiological conditions. The mechanism behind this adaptation is related to the fact that at fast rates not all ions channels are able to fully recover from inactivation before the next action potential occurs, resulting in a reduction in current (Keener & Sneyd, 2009; Yehia, Jeandupeux, Alonso, & Guevara, 1999).

An APD restitution curve can be constructed by measuring the APD for a wide range of DIs (see Figure 3.2 (b)). This curve reflects the underlining dynamics of the system during steady-state conditions. It has been studied that alternants (i.e. , different values of APD for a given DI) and spiral breackups may appear at APD restitution slopes bigger or equal to one (Karma, 1994; Gizzi et al., 2013; Koller et al., 2005). Moreover, it has been shown that some drugs have a flattening effect in the APD restitution slope, preventing the formation of fibrillation. Therefore, the APD restitution curve is highly relevant in the study of cardiac electrophysiology, since it allows a better understanding of the electrical behaviour of the myocardial tissue both under physiological and pathological conditions.

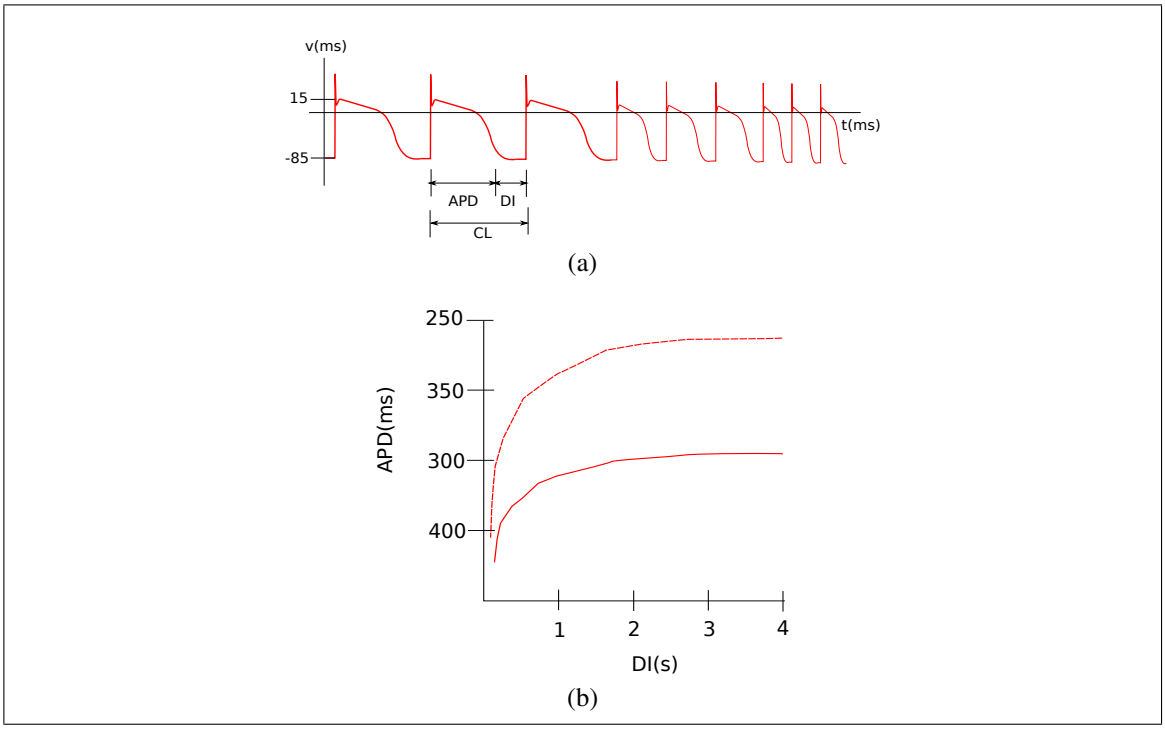

Figure 3.2. Schematic representation of the nonlinear relation between the stimulus frequency (CL) and the APD. (a) APD changes when the stimulus frequencies increases and (b) APD restitution curves for the Ten Tusscher-Panfilov model (ten Tusscher & Panfilov, 2006)

3.1.7. The Fenton-Karma model

The Fenton-Karma model is a phenomenological model developed to study arrhythmogenesis in cardiac tissue. It allows dealing with the computational difficulties of modeling spiral and scroll waves with more complex ionic models in continuous myocardium. The mechanisms of VF, such as the influence of fiber rotation on filaments instability, have been successfully studied using this model. Moreover, it incorporates the restitution properties of more complex ionic models or experimentally measured restitution curves, and reproduces accurate spiral wave behavior (F. Fenton & Karma, 1998). To capture these properties, this model retains a minimal ionic complexity. To this end, the current I_{ion} is written as

$$I_{ion} = I_{fi}(V, v) + I_{so}(V) + I_{si}(V, w), \tag{3.19}$$

where I_{fi} is a fast inward current responsible for depolarization of the membrane, this current depends only on an inactivation-reactivation gate v. This gate plays a similar role of the gates in the sodium current of the Beeler-Reuter and Luo-Rudy models. I_{so} is a slow outward current, comparable to the time-dependent potassium current, responsible for the repolarization of the membrane. I_{si} is a slow-inward current, comparable to the calcium current; it balances the slow outward current during the plateau phase of the action potential. The activation, inactivation, and reactivation dynamics described by these currents reproduce the recovery process of the membrane.

Usually, this model is rewritten based on a dimensionless membrane potential $u = (v - V_0)/(V_{fi} - V_0)$, where V_0 is the resting potential, and V_{fi} is the Nernst potential of the fast inward current. Currents are also scaled as $J_\chi = I_\chi/(C_m(V_{fi} - V_0))$ with units of inverse time. The equations are

$$\dot{u} = \nabla \cdot (D\nabla u) - J_{fi}(V, v) - J_{so}(V) - J_{si}(V, w), \tag{3.20a}$$

$$\dot{v} = H(u_c - u)(1 - v)/\tau_v^- - H(u - u_c)v/\tau_v^+, \tag{3.20b}$$

$$\dot{w} = H(u_c - u)(1 - w)/\tau_w^- - H(u - u_c)w/\tau_v^+ \,. \tag{3.20c}$$

where the currents are described by

$$J_{fi}(u, v) = -v\, H(u - u_c)(1 - u)(u - u_c)/\tau_d, \tag{3.21a}$$

$$J_{so}(u) = u\, H(u_c - u) + \frac{1}{\tau_r} H(u - u_c)/\tau_0, \tag{3.21b}$$

$$J_{si}(u, w) = -w(1 + \tanh[k(u - u_c^{si})])/(2\tau_{si}), \tag{3.21c}$$

where $H(x)$ is the Heaviside step function defined as $H(x) = 1$ for $x \geq 0$ and $H(x) = 0$ for $x < 0$.

The model parameters were selected originally to fit two different biophysically based models: the Beeler-Reuter and the Luo-Rudy-I models. As was exposed before, the former was essentially the first detailed model of ventricular action potential after the Noble's model based on the HH equations, and the LR-I model was an improvement of

the BR with more realistic sodium kinetics. Parameters for diverse models, such as the Courtemanche-Ramirez-Nattel (CRN), have been identified in different works, showing the high adaptability of the FK model to reproduce different dynamics (Courtemanche, Ramirez, & Nattel, 1998; Oliver & Krassowska, 2005).

3.1.8. The ten Tusscher-Panfilov 2006 biophysical model

The tenTusscher-Panfilov (TP06) biophysical model was developed based on experimental data on most of the major ionic currents of human myocardial cells and human APD restitution (ten Tusscher & Panfilov, 2006). It includes an extensive description of the calcium dynamics and adequately reproduces human epicardial, endocardial, and M cell action potentials. The relation between the recovery dynamics of the fast sodium current and the onset of instabilities was shown using this model. Moreover, although it includes a high level of electrophysiological detail, it is computationally cost-effective enough to be used in large scale simulations, particularly on the study of VT and VF dynamics (Ten Tusscher, Hren, & Panfilov, 2005; ten Tusscher & Panfilov, 2006). This model is described by the following equations

$$\dot{V} = \frac{1}{\chi C_m} \left(\nabla \cdot (\mathbf{D} \nabla V) - \chi (I_{ion} + I_{stim}) \right) \tag{3.22}$$

where χ is the surface-to-volume ratio and I_{ion} is the sum of all transmembrane ionic currents given by the equation

$$I_{ion} = I_{Na} + I_{K1} + I_{to} + I_{Kr} + I_{Ks} + I_{CaL} + I_{NaCa} + I_{NaK} + I_{pCa} + I_{pK} + I_{bCa} + I_{bNa}, \tag{3.23}$$

where I_{NaCa} is Na^+/Ca^{2+} exchanger current, I_{NaK} is Na^+/K^+ pump current, I_{pCa} and I_{pK} are plateau Ca^{2+} and K^+ currents, and I_{bCa} and I_{nNa} are background Ca^{2+} and Na^+ currents. The equations that describe each current and gating variables are reported in Appendix A.

3.2. Mathematical models of cardiac tissue electrophysiology

3.2.1. The bidomain model

The mathematical model for the propagation of action potential within the heart tissue is based on a volume-averaged approach (Franzone et al., 2014). To include the effects of the potential differences across the membrane, the tissue is divided into two separate domains: the intracellular domain and the extracellular domain. Based on the notion of *interpenetrating domains* both domains are assumed to be continuous an anisotropic, and they both fill the complete volume Ω_H of the myocardium. In each of these domains an electrical potential is defined, which at each point is taken as an average quantity over a small volume. Every point in the heart is assumed to be both in the extracellular and intracellular space, and therefore is assigned both an intracellular and extracellular potential. The cell membrane is also assumed to fill the complete volume of the heart. This membrane acts as an electrical insulator between the two domains. Although the resistance of the cell membrane is very high, it allows the transit of ions through specific channels. An electrical current travels through the membrane which magnitude depends on the potential difference across the membrane and its permeability to the ions. This potential difference is called *transmembrane potential* and is defined at every point as the difference between the extracellular potential and the intracellular potential. From Maxwell's equations we have that for a volume conductor, the relation between the electric and magnetic field is described as

$$\nabla \times \mathbf{E} + \frac{\partial B}{\partial t} = 0, \tag{3.24}$$

where $\mathbf{E}$ and B are the strengths of the electric and magnetic fields, respectively. In a quasi-static condition, equation 3.24 becomes

$$\nabla \times \mathbf{E} = 0, \tag{3.25}$$

which implies that the electric field may be written as the gradient of a scalar value potential. Denoting this potential by u, we have

$$\mathbf{E} = -\nabla u, \tag{3.26}$$

where the negative sign is a convention. The current $\mathbf{J}$ in a conductor is given by the general relation

$$\mathbf{J} = \mathbf{M}\mathbf{E}, \tag{3.27}$$

where $\mathbf{M}$ is the conductivity of the medium. From equation 3.26 we have

$$\mathbf{J} = -\mathbf{M}\nabla u \tag{3.28}$$

For the extracellular and intracellular domains within the myocardium this quasi-static condition also applies, thus we can express the current in the two domains as

$$\mathbf{J}_i = -\mathbf{M}_i \nabla u_i, \tag{3.29}$$

$$\mathbf{J}_e = -\mathbf{M}_e \nabla u_e, \tag{3.30}$$

where $\mathbf{J}_i(\mathbf{x}, t)$ is the intracellular current and $\mathbf{J}_e(\mathbf{x}, t)$ the extracellular current at any given point $\mathbf{x} \in \Omega_H$. $\mathbf{M}_i(\mathbf{x})$ and $\mathbf{M}_e(\mathbf{x})$ are the conductivity tensors in the two domains, which are inhomogeneous functions of space that reflect the local variations of conductances because of the presence of structural intra and extracellular inhomegeneities of resistance. u_i and u_e are the respetive intra and extracellular potentials. Given the small thickness of the cell membrane, the acumulation of charges in any point $\mathbf{x} \in \Omega_H$ is zero, this can be expressed as

$$\frac{\partial(q_i + q_e)}{\partial t} = 0 \tag{3.31}$$

where q_i is the intracellular charge and q_e is the extracellular charge. The net current for each domain is expressed as the sum of the rate of charge accumulation and the ionic

current exiting the the domain, then

$$-\nabla \cdot \mathbf{J}_i = \frac{\partial q_i}{\partial t} + \chi I_{ion}, \tag{3.32}$$

$$-\nabla \cdot \mathbf{J}_e = \frac{\partial q_e}{\partial t} + \chi I_{ion}, \tag{3.33}$$

where I_{ion} is the ionic current through the cell membrane. This ionic current is usually measured per unit area of cell membrane, whereas densities of charge and current are measured per unit volume. The constant χ represents the area of cell membrane per unit volume. Therefore χI_{ion} is ionic current per unit tissue volume. Combining equations 3.31, 3.32 and 3.33 we have

$$\nabla \cdot \mathbf{J}_i + \nabla \cdot \mathbf{J}_e = 0. \tag{3.34}$$

Relation 3.34 states that the total current is conserved. Moreover, including equations 3.29 and 3.30 into this equation gives

$$\nabla \cdot (\mathbf{M}_i \nabla u_i) + \nabla \cdot (\mathbf{M}_e \nabla u_e) = 0 \tag{3.35}$$

The difference between the extracellular and intracellular potential is in relation with the amount of charge and the capacitance, this relation is described by

$$v = \frac{q}{\chi C_m} \tag{3.36}$$

where $v = u_i - u_e$, $q = 1/2(q_i - q_e)$ and C_m is the capacitance of the cell membrane. The time derivative of equation 3.36 gives

$$\chi C_m \frac{\partial v}{\partial t} = \frac{1}{2} \frac{\partial (q_i - q_e)}{\partial t}, \tag{3.37}$$

and from equation 3.31 we get

$$\frac{\partial q_i}{\partial t} = -\frac{\partial q_e}{\partial t} = \chi C_m \frac{\partial v}{\partial t}, \tag{3.38}$$

Inserting this equation into equation 3.32 gives

$$-\nabla \cdot \mathbf{J}_i = \chi C_m \frac{\partial v}{\partial t} + \chi I_{ion}, \tag{3.39}$$

using equation 3.29 we have

$$\nabla \cdot (\mathbf{M}_i \nabla u_i) = \chi C_m \frac{\partial v}{\partial t} + \chi I_{ion}, \tag{3.40}$$

We can eliminate the intracellular potential from equations 3.35 and 3.40 using the fact that $u_i = u_e + v$

$$\nabla \cdot (\mathbf{M}_i \nabla (u_e + v)) = \chi C_m \frac{\partial v}{\partial t} + \chi I_{ion}, \tag{3.41}$$

$$\nabla \cdot (\mathbf{M}_i \nabla (u_e + v)) + \nabla \cdot (\mathbf{M}_e \nabla u_e) = 0 \tag{3.42}$$

If we rearrange the terms is these equations gives

$$\nabla \cdot (\mathbf{M}_i \nabla v) + \nabla \cdot (\mathbf{M}_i \nabla u_i) = \chi C_m \frac{\partial v}{\partial t} + \chi I_{ion}, \tag{3.43}$$

$$\nabla \cdot (\mathbf{M}_i \nabla v) + \nabla \cdot ((\mathbf{M}_i + \mathbf{M}_e) \nabla u_e) = 0 \tag{3.44}$$

This is known as the standard formulation of the bidomain model. This formulation was introduce by (Tung, 1978) in the late 70s. The anisotropy of the intra and extracellular media, related to the macroscopic arrangement of the cardiac myocites in the fiber structure, is described by the anisotropic conductivity tensors $M_i(\mathbf{x})$ and $M_e(\mathbf{x})$, defined as

$$\mathbf{M}_{i,e} = \sigma_l^{i,e} \mathbf{a}_l(\mathbf{x}) \mathbf{a}_l^T(\mathbf{x}) + \sigma_n^{i,e} \mathbf{a}_n(\mathbf{x}) \mathbf{a}_n^T(\mathbf{x}) + \sigma_t^{i,e} \mathbf{a}_t(\mathbf{x}) \mathbf{a}_t^T(\mathbf{x}). \tag{3.45}$$

Here $\mathbf{a_l}(\mathbf{x}), \mathbf{a_t}(\mathbf{x}), \mathbf{a_n}(\mathbf{x})$ is a triplet of orthonormal principal axes with $\mathbf{a}_l(\mathbf{x})$ parallel to the local fiber direction, $\mathbf{a}_t(\mathbf{x})$ and $\mathbf{a}_n(\mathbf{x})$ tangent and orthogonal to the radial laminae, respectively, and both being transversal to the fiber axis. $\sigma_l^{i,e}$, $\sigma_t^{i,e}$ and $\sigma_n^{i,e}$ are the conductivity coefficients in the intra and extracellular media measured along the corresponding directions.

To be able to solve the equations 3.43 and 3.44 we need to specify not only the local basis vectors $\mathbf{a_l}(\mathbf{x}), \mathbf{a_t}(\mathbf{x}), \mathbf{a_n}(\mathbf{x})$ and the local conductivity parameters but also the boundary conditions for u_e and v. If we assume that the heart is surrounded by a non-conductive medium, we require the normal component of both domains currents to be zero on the

boundary. Then

$$\mathbf{n} \cdot J_i = 0, \tag{3.46}$$

$$\mathbf{n} \cdot J_e = 0, \tag{3.47}$$

where $\mathbf{n}$ is the normal to the volume surrounding $\mathbf{x}$. Using the expression for the two currents we get

$$\mathbf{n}\cdot(\mathbf{M}_i \nabla v + \mathbf{M}_i \nabla u_e) = 0, \tag{3.48}$$

$$\mathbf{n}\cdot(\mathbf{M}_e \nabla u_e) = 0. \tag{3.49}$$

With these boundary conditions we obtain the parabolic-elliptic (PE) formulation of the bidomain equation (Franzone et al., 2014).

Bidomain formulation. Given the the initial conditions $v_0 : \Omega_H \to \mathbb{R}$, $\mathbf{w}_0 : \Omega_H \to \mathbb{R}^k$, $\mathbf{z}_0 : \Omega_H \to (0, +\infty)^m$, find the intra- and extracellular potentials $u_{i,e} : \Omega_H \times (0,T) \to \mathbb{R}$, the transmembrane potential $v = u_i - u_e : \Omega_H \times (0,T) \to \mathbb{R}$, the gating variables $\mathbf{w} : \Omega_H \times (0,T) \to \mathbb{R}^k$ and the ionic concentrations variables $\mathbf{z} : \Omega_H \times (0,T) \to \mathbb{R}^m$ such that

$$\begin{cases} \nabla \cdot (\mathbf{M}_i \nabla v) + \nabla \cdot (\mathbf{M}_i \nabla u_i) = \chi C_m \frac{\partial v}{\partial t} + \chi I_{ion} & \text{in } \Omega_H \times (0,T) \\ \nabla \cdot (\mathbf{M}_i \nabla v) + \nabla \cdot ((\mathbf{M}_i + \mathbf{M}_e) \nabla u_e) = 0 & \text{in } \Omega_H \times (0,T) \\ \frac{\partial \mathbf{w}}{\partial t} = \mathbf{F}(v, \mathbf{w}) & \text{in } \Omega_H \times (0,T) \\ \frac{\partial \mathbf{z}}{\partial t} = \mathbf{G}(v, \mathbf{w}, \mathbf{z}) & \text{in } \Omega_H \times (0,T) \\ \mathbf{n} \cdot (\mathbf{M}_i \nabla v + \mathbf{M}_i u_e) = 0 & \text{in } \partial\Omega_H \times (0,T) \\ \mathbf{n} \cdot (\mathbf{M}_e \nabla u_e) = 0 & \text{in } \partial\Omega_H \times (0,T) \\ v(\mathbf{x}, 0) = v_0(\mathbf{x}), \mathbf{w}(\mathbf{x}, \mathbf{0}) = \mathbf{v_0}(\mathbf{x}), \mathbf{z}(\mathbf{x}, \mathbf{0}) = \mathbf{z_0}(\mathbf{x}) & \text{in } \Omega_H. \end{cases} \tag{3.50}$$

3.2.2. The monodomain model

By making the assumption of equal anistropy rates $\mathbf{M}_e = \lambda \mathbf{M}_i$, where λ is a constant scalar, then $\mathbf{M}_e$ can be eliminated from the bidomain formulation, resulting in

$$\nabla \cdot (\mathbf{M}_i \nabla v) + \nabla \cdot (\mathbf{M}_i \nabla u_i) = \chi C_m \frac{\partial v}{\partial t} + \chi I_{ion}, \tag{3.51}$$

$$\nabla \cdot (\mathbf{M}_i \nabla v) + (1+\lambda) \nabla \cdot (\mathbf{M}_i \nabla u_e) = 0 \tag{3.52}$$

We get, from equation 3.52

$$\nabla \cdot (\mathbf{M}_i \nabla u_e) = -\frac{1}{1+\lambda} \nabla \cdot (\mathbf{M}_i \nabla v) \tag{3.53}$$

Inserting this into equation 3.51 we get

$$\nabla \cdot (\mathbf{M}_i \nabla v) - \frac{1}{1+\lambda} \nabla \cdot (\mathbf{M}_i \nabla v) = \chi C_m \frac{\partial v}{\partial t} + \chi I_{ion}. \tag{3.54}$$

Rearranging the terms in this last equation we get

$$\frac{\lambda}{1+\lambda} \nabla \cdot (\mathbf{M}_i \nabla v) = \chi C_m \frac{\partial v}{\partial t} + \chi I_{ion}. \tag{3.55}$$

Similarly, the boundary condition is set as

$$\mathbf{n} \cdot (\mathbf{M}_i \nabla v) = 0 \tag{3.56}$$

Monodomain formulation. Given the initial conditions $v_0 : \Omega_H \to \mathbb{R}$, $\mathbf{w}_0 : \Omega_H \to \mathbb{R}^k$, $\mathbf{z}_0 : \Omega_H \to (0, +\infty)^m$, find the the transmembrane potential $v = u_i - u_e : \Omega_H \times (0,T) \to \mathbb{R}$, the gating variables $\mathbf{w} : \Omega_H \times (0,T) \to \mathbb{R}^k$ and the ionic concentrations variables $\mathbf{z} : \Omega_H \times (0,T) \to \mathbb{R}^m$ such that

$$\begin{cases} \frac{\lambda}{1+\lambda} \nabla \cdot (\mathbf{M}_i \nabla v) = \chi C_m \frac{\partial v}{\partial t} + \chi I_{ion}. & \text{in } \Omega_H \times (0,T) \\ \frac{\partial \mathbf{w}}{\partial t} = \mathbf{F}(v, \mathbf{w}) & \text{in } \Omega_H \times (0,T) \\ \frac{\partial \mathbf{z}}{\partial t} = \mathbf{G}(v, \mathbf{w}, \mathbf{z}) & \text{in } \Omega_H \times (0,T) \\ \mathbf{n} \cdot (\mathbf{M}_i \nabla v) = 0 & \text{in } \partial\Omega_H \times (0,T) \\ v(\mathbf{x}, 0) = v_0(\mathbf{x}), \mathbf{w}(\mathbf{x}, \mathbf{0}) = \mathbf{v_0}(\mathbf{x}), \mathbf{z}(\mathbf{x}, \mathbf{0}) = \mathbf{z_0}(\mathbf{x}) & \text{in } \Omega_H. \end{cases} \tag{3.57}$$

There are many advantages in using the monodomain model, both from a mathematical point of view as well as from a computational point of view. However, the monodomain model has important limitations. The first one is related to the assumption of equal anisotropy ratios in the conduction of electrical impulses. It has been shown experimentally that this is not the case, and it is difficult to specify the parameter λ to obtain the closest approximation of the physiological conductivities. Moreover, some important electrophysiological phenomena vanish when equal anisotropy rates are assumed, such as the ability to simulate the low gap junctional coupling that arises during pathological conditions (Costa & Dos Santos, 2010), and phenomena of arrhythmia termination (defibrillation) (N. Trayanova, Plank, & Rodríguez, 2006). Therefore, whereas the monodomain model is still a useful tool for analysis and simplified computational studies, realistic simulations of many important phenomena must be tackle using a complete bidomain model. In contraposition with this, there are several studies that proved the capabilities of using the monodomain equation in clinical applications (Pathmanathan & Gray, 2018; Nash et al., 2006; H. J. Arevalo et al., 2016).

The assumption of a non-conductive volume surrounding the heart domain limits the monodomain and bidomain formulations to solely describe the evolution of the transmembrane potential through the myocardial tissue. Additional equations and boundary conditions must be added to these formulations to represent the potential distribution surrounding the heart. Human torso coupling is of great importance for the study of body surface maps and electrocardiograms. However, these types of problems are not approached in this thesis.

3.3. Numerical solution of electrophysiology models

To solve the set of partial differential equations that define the bidomain and monodomain models of cardiac electrophysiology we employ numerical discretizations, both in space and in time, that lead to linear systems of equations that can be implemented

and solved in a computer. In the following, we summarize the main spatial and temporal numerical methods for this goal.

3.3.1. Operator Splitting method

The operator splitting method is a technique for solving coupled systems os PDE's. It is based on the notion of split a system of complex equations into smaller parts that may be easier to solve. The class of operator splitting technique introduced here is the so-called fractional step method (LeVeque & Leveque, 1992). To introduce this technique, consider an initial value problem of the form

$$\frac{du}{dt} = (L_1 + L_2)u, \quad u(0) = u_0, \tag{3.58}$$

where L_1 and L_2 are operators on u, and u_0 is a given initial condition. Choosing an small time-step Δt, an approximate solution at $t = \Delta t$ may be computed by first solving the problem

$$\frac{dv}{dt} = L_1(v), \quad v(0) = u_0 \tag{3.59}$$

for $t \in [0, \Delta t]$. After this, we can solve the problem

$$\frac{dw}{dt} = L_2(w), \quad w(0) = v(\Delta t), \tag{3.60}$$

for $t \in [0, \Delta t]$. Using this technique we have that the solution $w(\Delta t)$ is a consistent approximation of $u(\Delta t)$. In fact, the splitting error at $t = \Delta t$ is given by (Sundnes et al., 2007)

$$w(\Delta t) - u(\Delta t) = \frac{\Delta t^2}{2}(L_1 L_2 - L_2 L_1)u_0 + O(\Delta t^3) \tag{3.61}$$

Then, the error after one time step is proportinal to Δt^2. When solving the equation in a given time interval, e. g. $t \in [0, b]$, the error at $t = b$ is proportinal to Δt. This splitting method is called Godunov splitting and is a first-order method. However, we can slightly modify this method is order to get a second-order accurate algorithm. For this, we first

solve the problem

$$\frac{dv}{dt} = L_1(v), \quad v(0) = u_0, \tag{3.62}$$

for $t \in [0, \Delta t/2]$. Then, solve the problem

$$\frac{dw}{dt} = L_2(w), \quad w(0) = v(\Delta t/2), \tag{3.63}$$

for $t \in [0, \Delta t]$. Finally, we solve the problem

$$\frac{dv}{dt} = L_1(v), \quad v(\Delta t/2) = w(\Delta t), \tag{3.64}$$

for $t \in [\Delta t/2, \Delta t]$. This splitting algorithm is usually called Strang splitting, and is a second-order accurate algorithm.

3.3.2. Operator Splitting for the monodomain model

Starting from the monodomain equations introduced in 3.57, the Strang splitting can be applied by defining the operators

$$L_1 v = -I_{ion}(v, \mathbf{w}), \tag{3.65}$$

$$L_2 v = \frac{\lambda}{1+\lambda} \nabla \cdot (\mathbf{M_i} \nabla v). \tag{3.66}$$

With these operators the splitting method become

$$\frac{\partial v}{\partial t} = -I_{ion}(v, \mathbf{w}), \tag{3.67}$$

$$\frac{\partial v}{\partial t} = \frac{\lambda}{1+\lambda} \nabla \cdot (\mathbf{M_i} \nabla v). \tag{3.68}$$

Now we have reduced the nonlinear PDE to a linear PDE and a nonlinear ODE. As we need to solve an ODE system for the gating variables $\mathbf{w}$ in the monodomain equations, this system can be solved simultaneously with the system described by 3.67 in the splitting. Now, assuming that $v^n = v(t_n)$ and $s_n = s(t_n)$ are known, the operations of the Strang splitting consist on the following operations:

(i) Solve the system

$$\frac{\partial v}{\partial t} = -I_{ion}(v, \mathbf{w}), \quad v(t_n) = v^n, \tag{3.69}$$

$$\frac{\partial \mathbf{w}}{\partial t} = R(v, \mathbf{w}), \quad \mathbf{w}(t_n) = \mathbf{w}^n, \tag{3.70}$$

for $t_n < t \leq t_n + \theta\Delta t$. The solutions at $t_n + \theta\Delta t$ are denoted v_θ^n and $\mathbf{w}_\theta^n$.

(ii) Solve the linear PDE given by

$$\frac{\partial v}{\partial t} = \frac{\lambda}{1+\lambda}\nabla \cdot (\mathbf{M_i}\nabla v), v(t_n) = v_\theta^n \tag{3.71}$$

for $t_n < t \leq t_n + \Delta t$. The solution at $t_n + \Delta t$ is denoted v_θ^{n+1}.

(iii) Solve the system

$$\frac{\partial v}{\partial t} = -I_{ion}(v, \mathbf{w}), \quad v(t_n + \theta\Delta t) = v_\theta^{n+1}, \tag{3.72}$$

$$\frac{\partial \mathbf{w}}{\partial t} = R(v, \mathbf{w}), \quad \mathbf{w}(t_n + \theta\Delta t) = \mathbf{w}_\theta^n, \tag{3.73}$$

for $t_n + \theta\Delta t < t \leq t_n + \Delta t$. Obtaining the approximate solutions v^{n+1} and $\mathbf{w}^{n+1}$ at $t = t_n + \Delta t$.

For values of $\theta = 1/2$ we obtain the second-order Strang splitting, and for $\theta = 1$ we obtain the first-order Godunov splitting.

The solution of the subproblems that appear in the different splitting algorithms have not been discussed yet. It is not usually easy to find an analytical solution of realistic choices of cell models and geometry for the monodomain equations. Then, it is necessary to use some numerical method to approximate a solution of the ODE system in step (i) and the PDE in step (ii). In general, for the Strang algorithm it is necessary to use at least a second-order accuracy method for the subproblems.

There is a large variety of methods for solving ODE systems. For the PDE system we are going to introduce a time discretization based on a θ-rule, which is a commonly used technique for solving PDEs. Assuming that the current value $v^n = v(t_n)$ is known, we want to find the unknown field v^{n+1} at the next time step. The idea behind the time

discretization θ-rule is to approximates v^{n+1} from

$$\frac{v^{n+1}-v^n}{\Delta t} = \theta\left(\frac{\lambda}{1+\lambda}\nabla\cdot(\mathbf{M}_i\nabla v^{n+1})\right) + \left((1-\theta)\frac{\lambda}{1+\lambda}\nabla\cdot(\mathbf{M}_i\nabla v^{n})\right), \quad (3.74)$$

which is a weighted average of the values from the current and the next time step, and the time derivative is a simple finite difference approximation. For a choice of $\theta = 1$ we have the implicit backward Euler method. For $\theta = 0$ the scheme is easily recognized as the forward Euler scheme. Setting $\theta = 1/2$ gives the Cranck-Nicolson scheme, which is second order accurate with respect to time. If we select $\theta = 1/2$ for the splitting method as well as for the time approximation scheme, we can see that the accuracy matches well.

3.3.3. Spatial discretization: the finite element method

The spatial discretization of the bidomain and monodomain equations has been approached with several methods, such as finite element methods, finite volume methods, and spectral methods (Dupraz et al., 2015; Abbasi & Clayton, 2013; Göktepe & Kuhl, 2009). Numerical methods and simulations of different eikonal approaches have also been explored (Pashaei, Romero, Sebastian, Camara, & Frangi, 2010). In this thesis we use the classical Galerkin procedure as the starting point for the formulation of a finite element discretization.

Variational formulation. Let V be the Sobolev space $H^1(\Omega_H)$ and defined by

$$(\varphi,\psi) = \int_{\Omega_H}\varphi\psi dx, \psi \in L^2(\Omega_H) \quad (3.75)$$

$$a(\varphi,\psi) = \int_{\Omega_H}(\nabla\varphi)^T\mathbf{M}_i(\mathbf{x})\nabla\psi dx,\ \forall\varphi,\psi \in H^1(\Omega_H) \quad (3.76)$$

the usual L^2-inner product and elliptic bilinear forms. The variational formulation of the monodomain model is defined as follows. Given $v_0, w_0 \in L^2(\Omega_H)$, $I_{app} \in L^2(\Omega_H \times$

$(0,T)$), find $v \in W^{1,1}(0,T;V)$ and $w \in W^{1,1}(0,T;L^2(\Omega_H)^M)$ such that $\forall t \in (0,T)$

$$\begin{cases} \chi C_m \frac{\partial}{\partial t}(v(t),\varphi) + a(v(t),\varphi) + \chi(I_{ion}(v,w),\varphi) = (I_{app},\varphi) & \forall \varphi \in V \\ \frac{\partial}{\partial t}(w(t),\psi) = (R(v(t),w(t)),\psi), & \forall \psi \in L^2(\Omega_H)^M \end{cases} \tag{3.77}$$

with appropiate given initial conditions on v and w.

Finite element discretization. Let $\mathcal{T}^h$ be a uniform hexahedral triangulation of Ω_H and V^h the associated finite element space. Given a finite element basis function $\{\phi_i\}$ for V^h and an appropriate quadrature rule, the symmetric mass matrix and stiffness matrix are given by

$$\mathbf{M} = \left\{ m_{rs} = \int_{\Omega_H} \phi_r \phi_s dx \right\}, \tag{3.78}$$

$$\mathbf{A} = \left\{ a_{rs} = \int_{\Omega_H} (\nabla \phi_r)^T \nabla \phi_s dx \right\}. \tag{3.79}$$

If we define I^h_{ion} and I^h_{app} the finite element interpolants of I_{ion} and I_{app} respectively, the finite element approximation $\mathbf{v}_h$ of the transmembrane potential is given by solving

$$\chi C_m \mathbf{M} \frac{\partial \mathbf{v}_h}{\partial t} + \frac{\lambda}{1+\lambda} \mathbf{A} \mathbf{v}_h + \chi \mathbf{M} I^h_{ion}(\mathbf{v}_h, \mathbf{w}_h) = \mathbf{M} I^h_{app}. \tag{3.80}$$

This equation is coupled with the semidiscrete approximations of the gating and concentration system

$$\frac{\partial \mathbf{w}_h}{\partial t} = R(\mathbf{v}_h, \mathbf{w}_h). \tag{3.81}$$

Based on the same finite element spatial discretization, the θ-rule time discretization of the PDE system in the second step of the Strang splitting algorithm, described by equation 3.74, can then be expressed as

$$\left(\mathbf{M} - \Delta t \theta \frac{\lambda}{1+\lambda} \mathbf{A} \right) \mathbf{v}_h^{n+1} = \Delta t (1-\theta) \frac{\lambda}{1+\lambda} \mathbf{A} \mathbf{v}_h^n + \mathbf{M} \mathbf{v}_h^n \tag{3.82}$$

3.4. Subject-specific modeling of the heart

During the last three decades the scientific community has worked on the construction of computational models of the heart that incorporate realistic geometry and physiological behavior. This is a challenging problem given the complex geometry of the heart and the circulatory system. One of the advantages of using the finite element method is that it is well suited for complex geometric domains and allows the representation of the local structure of the heart, such as myofibers. It also allows the representation of spatial heterogenities such as transmural heterogeneity as well as spaces of patological tissue such as ischemic tissue or infarcted scar tissue. These representations are usually extracted from image-based anatomy data from real patient-specific animal or human subjects.

3.4.1. Image based anatomy

The computational modeling of the electrical behavior of the heart relays in an accurate description of the heart anatomy. However, complex representations of heart anatomy are restricted by their computational demands. This has motivated the use of simplified left ventricular geometries as the primary tool for the study of cardiac electrophysiology and electromechanics. However, in the last decade, the use of patient-specific realistic geometries has become prevalent in computational models (K. L. Sack, Davies, Guccione, & Franz, 2016). Following the initial work of (Okajima, Fujino, Kobayashi, & Yamada, 1968),a finite element method was used to approximate the geometry and fiber direction of a canine heart (Nielsen, Le Grice, Smaill, & Hunter, 1991). After this, (Stevens, Remme, LeGrice, & Hunter, 2003) were able to extend the model to account for the four valves. Since then, the use of realistic heart geometries has become popular. Using computer tomography and MRI images, the Living Heart Project has created a full four-chambered heart with the connecting large vessels (Baillargeon, Rebelo, Fox, Taylor, & Kuhl, 2014). Subject-specific cardiac geometries of several animal species have been used in proof-of-concept studies of pathological and non-pathological cases (H. Arevalo, Plank, Helm, Halperin, & Trayanova, 2013; N. A. Trayanova & Chang, 2016a). Statistically averaged

heart geometries are another alternative for generating meaningful results within a representative patient population (Young & Frangi, 2009; Backhaus et al., 2010).

Several imaging techniques are used to perform cardiac examinations. Ultrasound (US), single-photon emission computed tomography (SPECT), computed tomography (CT), and magnetic resonance imaging (MRI) are the most well-known and used techniques (A. Chang, Cadaret, & Liu, 2020; Hendrikx, Vöö, Bauwens, Post, & Mottaghy, 2016; Deng, Jiao, Ye, & Xia, 2012). Moreover, their applicability has been powerfully extended by the recent developments in hardware, contrast agents, and algorithms for postprocessing (Attili, Schuster, Nagel, Reiber, & Van Der Geest, 2010; Kim et al., 2000). Faster image protocols and hardware improvements in MRI, CT, and US have resulted in near real-time dynamic three-dimensional imaging of the heart (S. Zhang et al., 2014; Saito, Saito, Komatu, & Ohtomo, 2003).

Cardiac MRI supplies a large source of detailed quantitative data of heart structure. The non-invasive nature, safe procedures, ability to modulate contrast in response to different mechanisms, and the ability to provide high-quality functional information in any direction are some of the advantages of cardiac MRI. This technique has provided detailed information on tridimensional ventricular shape and geometry, regional systolic and diastolic strain, material microstructure, and blood flow (Fonseca et al., 2004). MRI is increasingly being applied in cardiac research trials and clinical practice. Moreover, diffusion tensor MRI (DT-MRI) has been progressively used to measure myocardial fiber orientation in formaldehyde-fixed hearts (Holmes, Scollan, & Winslow, 2000). The diffusion pattern in DT-MRI is represented by a symmetric second-rank tensor in which its three orthogonal eigenvectors are related to cardiac structure (see Figure 3.3). The assumption on this technique is that the direction of greatest proton diffusion (i.e., the eigenvector with the largest eigenvalue) will be along the fiber parallel axis, the intermediate diffusion (secondary eigenvector) will lie orthogonal to the fiber axis, and the minor direction of diffusion will lie orthogonal to the primary and secondary eigenvectors (Helm, Beg, Miller,

& Winslow, 2005). These results have been validated using three-dimensional histological reconstructions of the fiber and sheet.

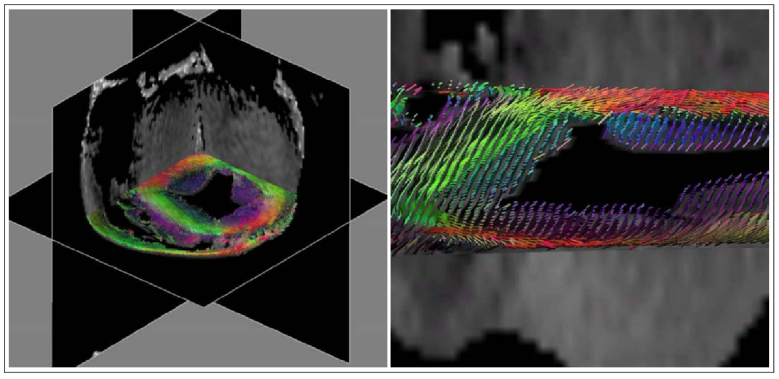

Figure 3.3. visualization of DT-MRI reconstruction of a heart (left) and zoomed view (right) showing the components of the fibers direction in colors. Taken from (Zhukov & Barr, 2003)

4. CARDIAC ARRHYTHMIA AND HEART FAILURE

4.1. Cardiac arrhythmia

4.1.1. Types of reentrant cardiac arrhythmia

Cardiac arrhythmia, also known as heart rhythm disorders, are conditions in which a failure in the timing and / or coordination of cardiac contraction occurs. Their cause is mainly related to abnormal formation of the excitation wave (abnormal automaticity or triggered activity), abnormal propagation of the excitation wave, or both. There are different types of cardiac arrhythmias. A frequently occurring and dangerous category are the so-called reentrant arrhythmias, which are caused by abnormal reentrant propagation of excitation waves. Reentrant arrhythmias in the ventricles can be classified in monomorphic and polymorphic VT and VF. Monomorphic and polymorphic VT (among which is the Torsade de Pointes) lead to increased ventricular excitation and contraction rates along with a decrease of cardiac output. Both cases may destabilize into VF, which leads to a further increase in excitation rate and a loss of coherence of ventricular contraction, resulting into a complete loss of cardiac output. This will cause death to occur within minutes unless normal sinus rhythm is restored. VT and VF belong to the most dangerous cardiac arrhythmias.

4.1.2. Mechanisms of cardiac arrhythmias

The term reentry refers to a wave front that reenters and hence re-excites the same tissue repeatedly as opposed to the normal ”planar” wave front emitted by the SA node that excites all the tissue only once. If a high-frequency re-excitation occurs, surpassing the sinus rhythm, the sinus rhythm gets suppressed and heart rhythm is controlled by the reentry, resulting in an increased heart rate. In one dimension, reentry can be seen as a single pulse traveling around a circular cable of tissue. This phenomenon has been demonstrated both in experiments and models of excitable media (Winfree, 1989). In two

and three dimensions, reentry can be caused by a spiral or scroll wave front rotation around an in-excitable obstacle. This has been demonstrated using abstract models of excitable media (Ten Tusscher et al., 2005). This so called anatomical reentry is commonly seen in the atria, where a large vessel, tissue ridge or scar may act as anatomical obstacle for the formation of an spiral or scroll wave.

Within the ventricles VT is also thought to be caused by an spiral or scroll wave front. It has been shown that scroll waves do not necessarily rotates around an in-excitable obstacle, but can also rotate around a core that is formed by the refractory properties of the excitable medium (Panfilov & Pertsov, 2001a). This type of reentry is usually called functional reentry. Since the ventricles are more homogeneous than the atria and posses less ridges and holes caused by large vessels relative to their tissue mass, ventricular reentry is usually functional reentry. However, when a scar is formed due to a particular cardiac disease, anatomical reentry may occur around the scar tissue. An experimental proof of the possible presence of functionally reentrant spiral and scroll waves in cardiac tissue was first given by (Allessie, Bonke, & Schopman, 1976) in rabbit atrium, and later on by (Davidenko, Pertsov, Salomonsz, Baxter, & Jalife, 1992). Nowadays, it is a commonly accepted fact that most VT are caused by a spiral or scroll wave front.

4.1.3. Vortex filaments computation during fibrillation

During re-entry an action potential continuously propagates around a point (in two dimensions) or a filament (in three dimensions), forming a vortex-like wave, known as scroll wave in three dimensions. The shape, sustainability, and overall behavior of these phase singularities may be influenced by the anisotropy of the ventricular wall, tissue restitution, and intrinsic three-dimensional instabilities. These singularities were challenging to observe experimentally until recently were singularities could be observed within the contracting heart using high-resolution four-dimensional ultrasound-based strain imaging, showing that mechanical and electrical singularities coexist during cardiac fibrillation (Christoph et al., 2018). VF can then be characterized by studying filament dynamics

since decomposing the intricate activation pattern to show filaments provides insightful information about how many sources organize the excitation propagation (see Figure 4.1). Tracking them will explain the changes in excitation patterns over time. In order to apply this approach, we need an algorithm to identify filaments in three-dimensional wave propagation (Clayton, Zhuchkova, & Panfilov, 2006).

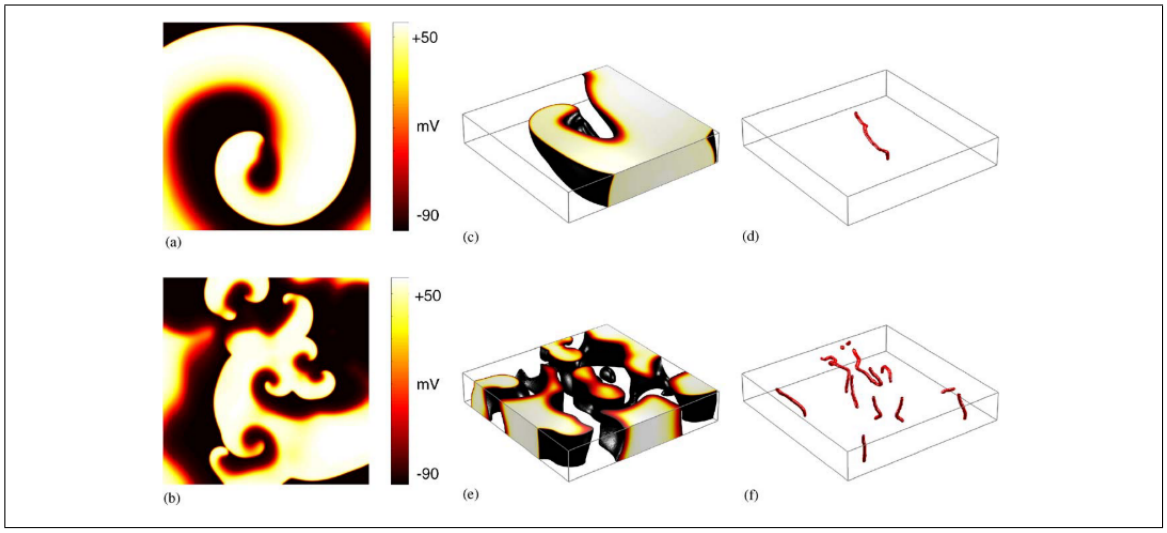

Figure 4.1. Example of a spiral wave formation (a) and multiple spiral wave formation (b) in two-dimensions. 3D scroll wave formation are also showed (c,e) with their corresponding filaments (d,f) (from (Clayton et al., 2006))

Scroll wave filaments were distinguished using the algorithm proposed by Fenton and Karma (F. Fenton & Karma, 1998). In particular, a singular point is found by computing the intersection of an isopotential line (-70 mV) with the condition $dV_m/dt = 0$. In the computational model here implemented, each singular point is related to a single finite element. Afterwards, scroll wave singular line, e.g. filament, was identified and labeled by using a density-based spatial clustering algorithm (DBSCAN)(Ester, Kriegel, Sander, & Xu, 1996). This method allows grouping elements that are closely packed together forming a specific filament. Each group (filament) formed is classified, updated and counted every $10\,ms$ of physical time directly during simulations.

4.2. Heart failure

4.2.1. Definition and incidence

Heart failure is a chronic and progressive condition in which the heart can not supply the required amount of blood and oxygen to meet the body needs. Heart function impairment leads to fatigue and shortness of breath, and everyday activities such as walking or climbing stairs can become very difficult (Mant et al., 2010). It is a serious condition and usually there is no cure. Nowadays 5.1 million people in the United States live with it, and it is estimated that 8 million people living in the United States will have heart failure by the year of 2030. Moreover, mortality is high since patients who die within the first 5 years after a heart failure diagnosis may reach 50%. Moreover, 40% of patients die within the first year after hospitalization for HF (Benjamin et al., 2019). Despite the advance in treatments and devices in the last years, mortality rates are still at high levels. Heart failure is divided into two categories: heart failure with reduced ejection fraction (HFrEF) accounting for 50% to 70% of the cases, and heart failure with preserved ejection fraction (HFpEF) (Savarese & Lund, 2017; Galli & Lombardi, 2016).

The American Heart Association (AHA) and the American College of Cardiology (ACC) have classified chronic heart failure into fourth stages, with disease severity increasing from the first to the fourth stage. In stage A there is presence of risk factors for heart failure without structural heart disease, stage B is the presence of a structural heart disease without symptoms, stage C is symptomatic heart failure, and stage D is symptomatic heart failure with the need of medical therapy (Dolgin, of the New York Heart Association, Committee, Fox, & Levin, 1994). Structural heart disease is related with ventricular hypertrophy in hypertensive patients, valvular diseases and scars due to a previous myocardial infarction. The incidence of heart failure after myocardial infarction is 8% in men and 18% in women between 45 and 64 years old (Chandrasekhar, Gill, & Mehran, 2018; Crespo-Leiro et al., 2018). It has been studied in animal models of myocardial infarction and cardiac imaging in patients with ischemic cardiomyopathy that heart

failure if preceded by an increase in ventricular volumes. This process is called ventricular remodeling, and it implies the enlargement of the left ventricular chamber, changing from an elliptical to a more spherical shape (Konstam, Kramer, Patel, Maron, & Udelson, 2011). This change is described by the sphericity index, which is the ratio between the left ventricular volume and the volume of a sphere whose diameter is equal to the mayor axis of the left ventricle. Post-infarct remodeling developed in around 30% of patients with a history of myocardial infarction (Galli & Lombardi, 2016).

4.2.2. Post myocardial-infarction heart remodeling in heart failure

Cardiac remodeling is a physiological (adaptative) or pathological state in which cellular and interstitial changes occur within the heart. Clinically, remodeling diagnosis is based on the detection of morphological changes such as the cavity diameter, mass (hypertrophy and atrophy), geometry (heart wall thickness and shape), areas of scar after MI, fibrosis, and inflammatory infiltrate (myocarditis) (Azevedo, Polegato, Minicucci, Paiva, & Zornoff, 2016). It is also related to ventricular dysfunction and malignant arrhythmias (Konstam et al., 2011). In the acute and chronic phases of MI, remodeling may be identified due to the dilation of the infarcted area secondary to the expansion process or eccentric hypertrophy of the infarcted area secondary to different stimuli (Azevedo et al., 2016). Therefore, despite its complexity, post-infarction remodeling may be clinically characterized by an increase in the ventricles size.

Ventricular remodeling is a predictor of heart failure, and its occurrence has an essential impact on prognosis. An arbitrary definition of ventricular remodeling, but widely adopted, is an increase of at least 20% of left ventricular end-diastolic ventricular volume (LVEDV) from the first postinfarction imaging (Cokkinos & Belogianneas, 2016). However, as the first imaging study with cardiac magnetic resonance is usually performed a few days after myocardial infarction, early ventricular remodeling, which is the phase of

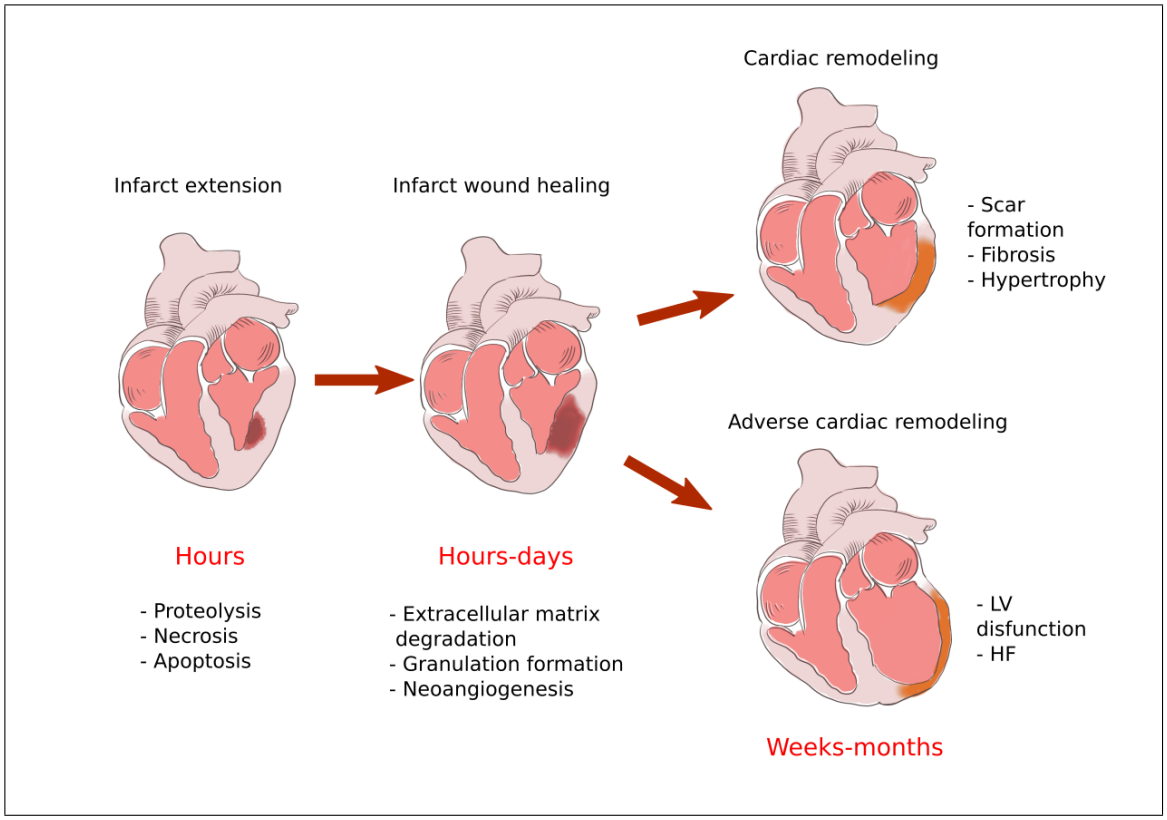

Figure 4.2. Myocardial infarction stages

remodeling that occurs in the first hours after myocardial infarction, could not be recognized, leading to an underestimation of the final ventricular dilatation (Galli & Lombardi, 2016).

The association of malignant ventricular arrhythmias, including VT and VF, with cardiac remodeling has been well established (Dhein et al., 2014; Ten Tusscher, Hren, & Panfilov, 2007). Several mechanisms of cardiac arrhythmias after MI have been identified. The first mechanism is related to changes in the ion channels, such as inactivation of the sodium channels, changes in calcium and potassium channels and alterations in the sodium/calcium relation (Bosch et al., 1999). As a consequence of this, action potential duration (APD) and action potential restitution abnormalities are encountered in remodeled hearts (Gizzi et al., 2013; ten Tusscher & Panfilov, 2006). The second mechanism is the gap junctional intercellular communication changes, responsible for the electrical

coupling between each cell. Finally, cardiac remodeling is associated with an increase in collagen content (fibrosis), which may cause blockage of the electrical conduction and reentry arrhythmia (Shinde & Frangogiannis, 2014), associated with arrhythmias and sudden cardiac death. Clinical strategies to reduce fibrosis have decreased the vulnerability to arrhythmias (Hinderer & Schenke-Layland, 2019).

Due to lost of contractility of the necrotic segments, ventricular contraction is not symmetrical in infarcted hearts. As a result, there is not a counterbalanced distribution of forces, and the infarcted ventricular wall is thus stretched by an increased wall tension that is not homogeneously distributed in the left ventricle. This was verified using MRI data from human hearts (Zhong et al., 2009). This phenomenon might explain why the infarcted wall usually has longer contraction times than the healthy remote myocardium. The infarcted wall has to counteract a greater resultant force, and its prolonged time to peak systolic velocity can be detected as an asynchrony of the left ventricular wall motion (Y. Zhang et al., 2008). This wall motion defect has been recognized as a risk factor for remodeling development, and it can be detected using MRI (S. Chang et al., 2009).

4.2.3. Current therapies to Heart Failure

Clinical evidence has shown that heart remodeling after MI can be prevented or, in some cases, reversed. This process is called reverse remodeling and can be achieved either with pharmacologic therapies or mechanical devices, which are usually combined (Koitabashi & Kass, 2012). Reverse remodeling improves chamber volumes and heart-rate responsiveness. At the cellular level, it improves myocyte size, function, and excitation-contraction coupling, among other important features (Koitabashi & Kass, 2012). While mechanical interventions require surgery and are reserved for patients in stage D of heart failure who meet strict eligibility criteria, drug delivery is the preferred treatment for patients with mild heart failure or for preventing remodeling after a myocardial infarction(Galli & Lombardi,

2016). Stem cells and gene therapy have shown promising results in pilot trials on adjunctive therapy of myocardial infarction and heart failure and might reverse remodeling after myocardial infarction (Windecker, Bax, Myat, Stone, & Marber, 2013).

One of the main treatments for patients with heart failure symptoms is cardiac resynchronization therapy (CRT). This therapy involves the implantation of a half-dollar sized pacemaker in conjunction with three leads that monitor the heart rate and detect abnormalities, emitting tiny electrical pulses to correct them. This procedure has shown to reduce the dyssynchronous left ventricular contraction caused by regional delays in the electrical activity in patients with heart failure due to dilated cardiomyopathy (Bristow et al., 2004). In short-term studies, CRT has shown to improve symptoms, increase exercise tolerance, and partially reduce cardiac remodeling (Bristow et al., 2004; Ruschitzka et al., 2013; Koitabashi & Kass, 2012). In addition to this, this treatment has proved to decrease the risk of death and related heart failure complications. Moreover, implantable cardioverter-defibrillators have shown increased effectiveness when used in combination with CRT (Bristow et al., 2004).

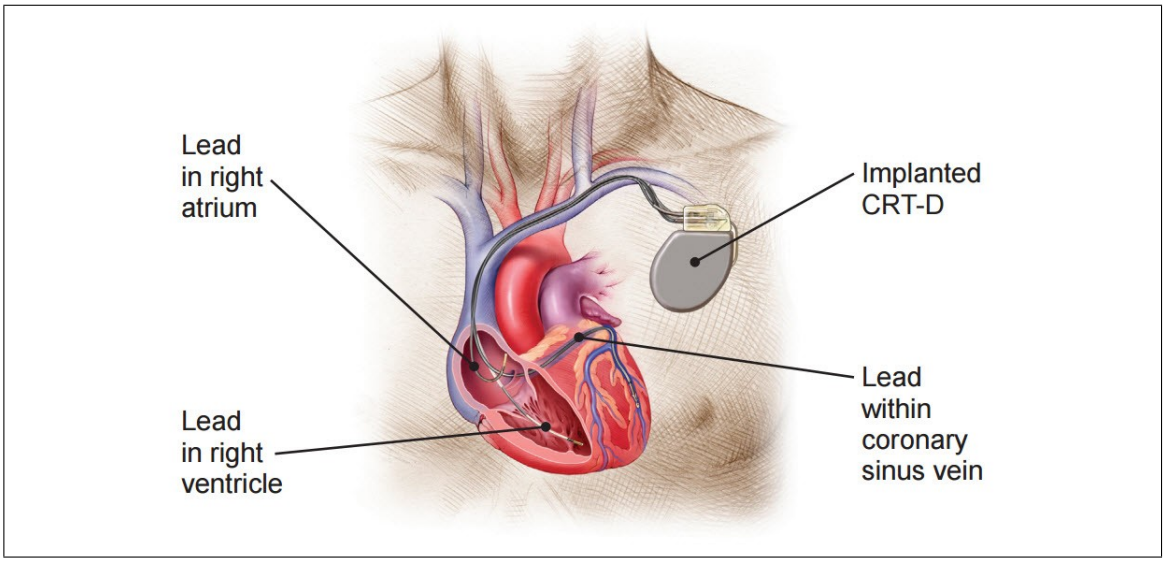

Figure 4.3. Cardiac resynchronization therapy (CRT). A pacemaker device is implanted in conjuction with three leads that monitor the heart rate and detect abnormalities (taken from (*How CRTs Work*, 2017)).

Although several important advances in pharmacological treatments of HF have significantly reduced mortality, the progression from asymptomatic ventricular dysfunction to symptomatic HF is still frequent. It has been recognized that myocardial hypertrophy is related to sustained neurohormonal activation. Although it has been shown that the pharmacological blockade of some neurohormonal pathways may reverse this process, attempting to blockade additional pathways may be detrimental (Mancini & Burkhoff, 2005). Given this, surgical reshaping of the dilated heart has been significantly studied with satisfactory outcomes. The concept behind this treatment is to reduce the size of the dilated heart, increasing the systolic myocardial wall stress (see Figure 4.4). The surgical procedure and its effects differ depending on the properties of the removed muscle. When a healed scar is present, non-contractile material is removed during the surgery, and satisfactory outcomes have been reported (Mickleborough, Carson, & Ivanov, 2001). The limitations of these surgeries are related to the lack of a uniform method to perform the procedure (Buckberg, Athanasuleas, & Conte, 2012). The amount of tissue removed and the size and shape of the reconstructed chamber are at the discretion of the surgeon, with no defined guidelines (Mancini & Burkhoff, 2005; Stefanelli et al., 2020).

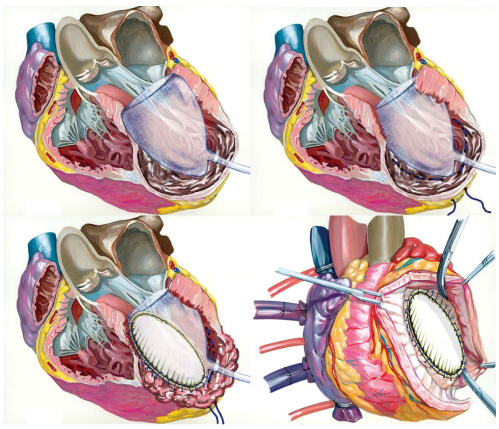

Figure 4.4. Surgical reshaping process. A mannequin is used to reconstruct the remodeled left ventricle in an elliptical shape (taken from (Castelvecchio & Menicanti, 2013)).

4.3. Biomaterial injection therapy

Novel strategies are being implemented to compensate for the insufficient intrinsic ability of the adult heart to regenerate after MI. These strategies are focused on inducing cardiac regeneration, facilitate self-repair, reverse or attenuate adverse remodeling, and ultimately improve the cardiac function. Cardiac tissue substitutes, biomaterial-assisted cell transplantation to improve retention, acellular biomaterials to confer mechanical support and extracellular matrix replacement is being studied to achieve these goals. Biomaterials are widely used in tissue engineering and regeneration due to their biocompatibility, non-thrombogenic nature, and their resemblance to their hydrogel matrix texture and stiffness to that of the extracellular matrix. The injection of biomaterials within the myocardium has shown promise as an alternative biological treatment option after MI to reduce adverse remodeling and preserve cardiac function. They can be delivered alone or as vehicles for carrying drugs or cells, and may provide mechanical support to the injured heart. Pre-clinical studies have shown several improvements on hearts injected with passive biomaterials (Lee et al., 2015; Ruvinov & Cohen, 2016). Augmentation of LV wall thickness with alginate hydrogel has shown to reduce LV end-diastolic and end-systolic volumes, and improve LV sphericity in dog heart (Sabbah et al., 2013). A substantial reduction in myofiber stress with positive effects on ventricular geometry has been shown in studies of swine hearts subjected to biomaterial injections (Choy et al., 2018).

Recently, the mechanical response of infarcted hearts to biomaterial injections was quantified using predictive computational modeling (K. L. Sack et al., 2016). Three-dimensional finite element analyses informed by echocardiography data from sheep hearts were carried out to compare different material properties of infarcted and healthy regions, showing that the presence of tissue filler significantly reduces myofiber stresses (Wenk et al., 2011). Idealized ellipsoidal LV models have also been used to measure the mechanical effects of different biomaterials, identifying the optimal distribution of injectates in terms of mechanical power (Wenk et al., 2009). High-resolution ex-vivo data was used

to show that biopolymer injections act as an LV mid-wall constraint mechanism that prevents adverse remodeling in the heart without secondary effects on the cardiac function (K. L. Sack et al., 2020), see Figure 4.5. While these studies helped to elucidate the promising outcomes of biomaterial injections from a mechanical point of view, their role in cardiac electrical behavior remains poorly investigated. Few recent animal studies have done so. In one study, conductive biomaterials aimed at restoring impulse propagation in rat hearts reduced the QRS interval, suggesting improved electric conduction after MI (Mihic et al., 2015). Hydrogel injections, with a high degree of intra-myocardial spread, did not cause significant electrical abnormalities in rat hearts (Suarez et al., 2015). The knowledge acquired from experimental approaches is still limited because of the complex nature of these treatments and the strong constraints in measuring electrical propagation *in vivo*. In this thesis, we focused on the study of the Algisyl-LVR^{TM}, a Calcium-Alginate hy-

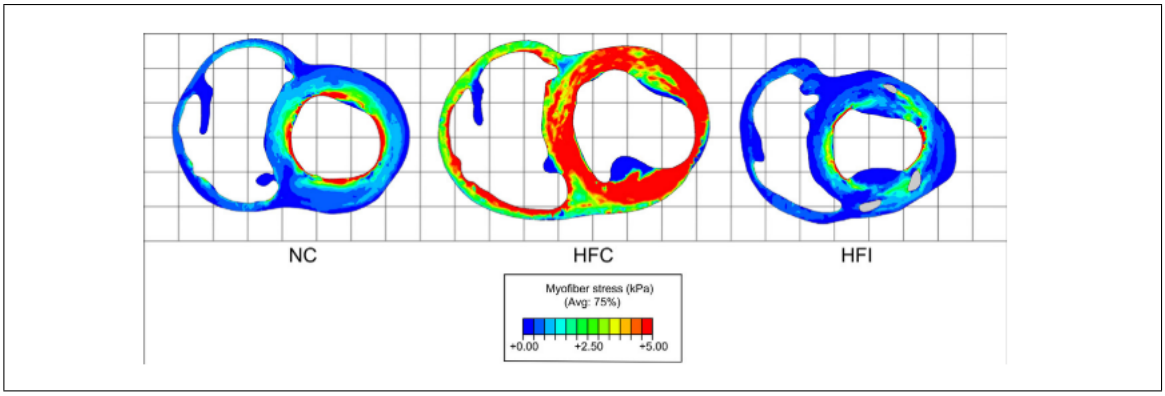

Figure 4.5. End-diastolic myofiber stress distribution comparing a control heart (NC) and heart with HF (HFC) and a heart with HF and biomaterial injections (taken from (K. L. Sack et al., 2020)).

drogel that consists of two components: a Na^{+}-Alginate component supplied as a sterile solution and a Ca^{2+}-Alginate component. These two components are mixed immediately before use and delivered as an intramyocardial injection with a syringe. In approximately 3-4 minutes, the biomaterial reaches its final material stiffness, which resembles that of the passive myocardium (see Figure 4.6). Alginate is a naturally-occurring polysaccharide found in certain species of brown algae. The process of isolating alginate from algal

biomass is simple. This biomaterial is directly injected in a circumferential pattern into the LV wall during an open chest procedure. A total of 12 to 14 injections are delivered in two rows: one above and one below the mid-ventricular plane between the base and the apex.

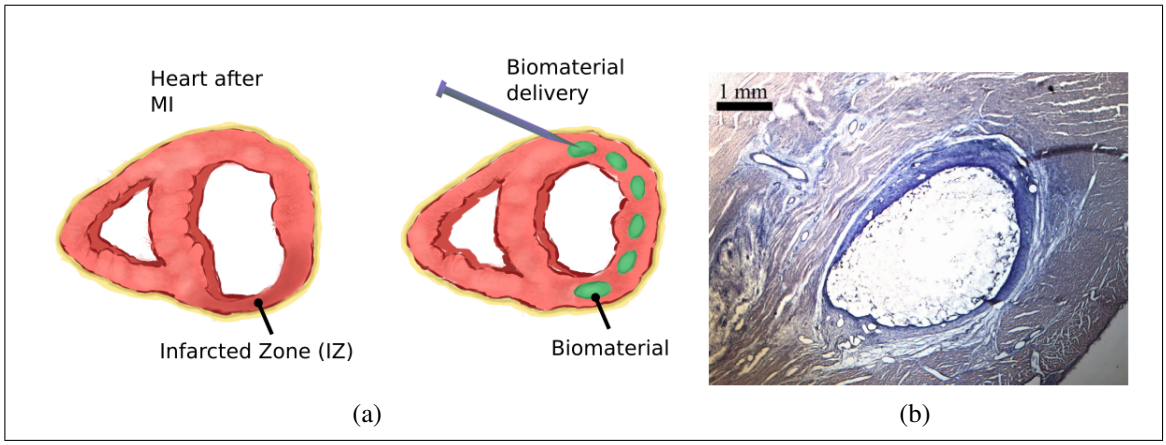

Figure 4.6. (a) Biomaterial delivery process after MI and (b) histology of a representative heart injected with Algisyl-LVR™ (from (K. L. Sack et al., 2020))

5. IN-SILICO STUDY OF ARRHYTHMOGENIC POTENTIAL OF BIOMATERIAL INJECTION THERAPY IN SWINE HEARTS UNDER HEART FAILURE

This chapter is an adapted transcription of the article "In-silico study of the cardiac arrhythmogenic potential of biomaterial injection therapy" *published in Scientific Reports 10(1):12990, June 2020.*

The vast literature about computational models in cardiac electrophysiology has made it possible to simulate most of the complex mechanisms leading to cardiac arrhythmogenesis, particularly when using highly-detailed anatomical models of the heart (N. A. Trayanova & Chang, 2016a; Witzenburg & Holmes, 2017). For instance, through MRI-based canine ventricular geometries, the arrangement and size of the peri-infarct (border) zone (BZ) were shown to be related to electrical excitation wavebreaks and onset of subsequent arrhythmias (H. Arevalo et al., 2013). Detailed electrophysiological models of human ventricles were used to study the morphology of VF, confirming that VF dynamics mainly depend on APD restitution properties (Tusscher et al., 2007). In-silico studies of histologically-based rabbit heart models with infarction were used to develop indices for measuring vulnerability to VT, which were previously validated in clinical applications and optical mapping(Hill et al., 2016). Prediction of electrophysiological behavior of cell-based heart repair was addressed using 3D whole-heart modeling to explore the sustainability of VF of these treatments, demonstrating the promising outcomes of computational modeling for evaluating alternative therapies for HF (Deng, Prakosa, Shade, Nikolov, & Trayanova, 2019). More specifically, patient-specific in-silico studies have allowed the quantification of scroll-wave filaments arising during VF (Panfilov & Pertsov, 2001b; Hu, Gurev, Constantino, Bayer, & Trayanova, 2013; Dierckx, Fenton, Filippi, Pumir, & Sridhar, 2019; Larson, Dragnev, & Trayanova, 2003), and their association to the effectiveness of defibrillation therapies (F. Fenton et al., 2009; Luther et al., 2011; N. Trayanova et al., 2006). This knowledge takes high relevance in the clinical management of failing hearts, as current clinical guidelines recommend implantable defibrillators as therapy for primary prevention of sudden cardiac death after MI (Völler et al., 2010;

Maqsood & Rubab, 2019). The capabilities of using computational models to study the electrical behavior of infarcted hearts have been demonstrated, but have not been used to assess the potential role of biomaterial-injection treatments in the arrhythmic behavior of treated subjects.

In this thesis, we investigated the electrical behavior and arrhythmic potential of swine hearts treated with biomaterial injections by means of computational modeling. To this end, we used high-resolution DT-MRI images of swine hearts treated with Algisyl-LVR^{TM} to create a computational model that represent the biventricular cardiac anatomy as well as the myocardial fiber orientations. We modeled and parameterized the transition zone from infarcted tissue towards the healthy tissue and modeled local tissue heterogeneities from MRI, accounting for injectate volumes. To account for transmural dispersion of repolarization, we divided the heart walls into three layers with endocardial, mid-myocardial, and epicardial cells, and modeled their distinctive behavior using a biophysical cellular model with specific properties for each layer. By performing an extensive computational campaign, we quantitatively characterized the electrical restitution properties of treated and untreated heart models and their performance during VF conditions. To do this, we developed a numerical method to compute important parameters such as activation time (AT) distributions, diastolic interval (DI) distributions and filament counting during simulations. Moreover, to assess the regional dispersion we constructed probability density functions of the APD restitution curve in different regions of the heart. Finally, we examined how the passive electrical properties of the injections influenced the long-term dynamics of VF for the treated heart models. By using computational modeling, this research assesses for the first time the potential of biomaterial injections to become a substrate for arrhythmia and their influence in the dynamics of VF.

5.1. Methods

5.1.1. Geometrical and morphological representation of swine hearts

This study considered one normal control heart (NC), one heart control with ischemic heart failure without biomaterial treatment (HFC), and one heart with ischemic HF and biomaterial injections (HFI). These subjects were selected as representative of larger cohorts considered in a previous morphological study of the effects of fiber remodeling under biogel treatment(K. L. Sack, Aliotta, Choy, et al., 2018). The three selected subjects included natural geometrical differences due to biological variance and remodeling to ischemia. This has been quantified in previous studies which showed local wall thinning and fiber reorientation due to ischemia, but that the global structure and morphology of the hearts were not significantly different (K. L. Sack, Aliotta, Choy, et al., 2018). The injection protocol for the hydrogel delivers a total of 12-14 intra-myocardial injections (0.3mL each) in a circumferential pattern into the LV free wall during an open chest procedure. These are administered in roughly 1.5 cm apart and in two rows: one above and one below the mid-ventricular plane between the base and the apex. The hydrogel, which accounts for roughly 3% of the total LV wall volume, does not disrupt fiber orientation, but rather conforms to the native structure it is injected into, forming ellipsoidal shapes orientated with the local fiber structure (K. L. Sack, Aliotta, Choy, et al., 2018). The solidified injections mitigate the effects of adverse remodeling by anchoring and supporting the surrounding tissue in the nearby vicinity of the circumferential pattern. A deeper analysis of therapy efficacy and the mechanism of action in mechanical terms was recently provided in a recent study (K. Sack et al., in press.).

Subject-specific accurate geometric representations of heart bi-ventricular structure, infarcted tissue, and biomaterial injections are used as the computational domain for the numerical simulations (Figures 5.1 and 5.2). Imaging data originates from *ex vivo* segmentation of high-resolution MRI and DT-MRI of swine hearts. The experimental protocol,

image acquisition, segmentation process and reconstruction methodology have been described previously(K. L. Sack, Aliotta, Ennis, et al., 2018; Choy et al., 2018). In brief, myocardial infarction was induced by occluding the obtuse marginal branches of the left circumflex artery. Eight weeks after MI, animals underwent Algisyl-LVR^{TM} injection, and hearts were excised eight weeks later. Anatomical MRI and DT-MRI were acquired using a readout-segmented diffusion-weighted spin-echo sequence with $1.0 \times 1.0 \times 1.0\,\mathrm{mm}^3$ spatial resolution.We discretized the heart domains using tetrahedral finite elements, identifying healthy, infarcted and hydrogel regions based on MRI observations (Figure 5.1). Following previous works(K. L. Sack, Aliotta, Ennis, et al., 2018), local properties for the infarcted and healthy tissues are modulated by the volume fraction of healthy tissue. This volume fraction is represented by the space-dependent scalar function $h = h(\mathbf{x}) \in [0, 1]$, where $\mathbf{x}$ represents the Cartesian coordinate vector. In particular, $h(\mathbf{x}) = 0$ defines properties of the infarcted zone (IZ), $h(\mathbf{x}) = 1$ identifies healthy tissue, and $0 < h(\mathbf{x}) < 1$ defines the transition zone or gray zone (GZ), where mixed electrical properties of infarcted and healthy tissue are modeled according to the literature (Mendonca Costa, Plank, Rinaldi, Niederer, & Bishop, 2018; H. Arevalo et al., 2013). A gray zone ratio (GZR) could also be computed from this function to characterize the differences in GZ distribution between each heart under study. Myocardial fiber orientation, based on DT-MRI data from three different swine hearts, was assigned to the mesh nodes and interpolated inside each finite element, delivering a continuous spatial vector field representation of the cardiac fiber orientation $\mathbf{f} = \mathbf{f}(\mathbf{x})$ for each heart analyzed (K. L. Sack, Aliotta, Ennis, et al., 2018). To account for transmural dispersion of repolarization, we used a Laplace's interpolation method(Perotti, Krishnamoorthi, Borgstrom, Ennis, & Klug, 2015) to divide the heart wall into epicardial, mid-myocardial, and endocardial layers using a thickness ratio of $2 : 3 : 3$, respectively. Figure 5.3 shows these transmural layers for the three hearts analyzed. The LVMM surface used in the study of APD distribution was constructed from the Laplace's interpolation by creating a mesh at the mid-surface of the mid-myocardial region.

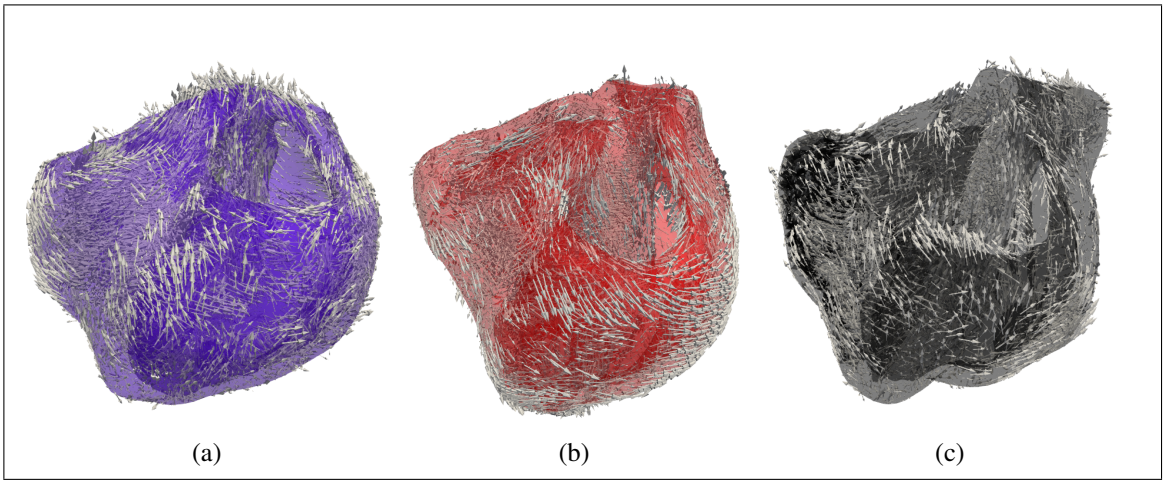

Figure 5.1. Heart geometry and fiber directions: (a) normal control (NC) heart, (b) heart-failure heart (HFC), (c) heart-failure heart treated with biomaterial injections (HFI). The geometry was reconstructed from high-resolution magnetic-resonance images

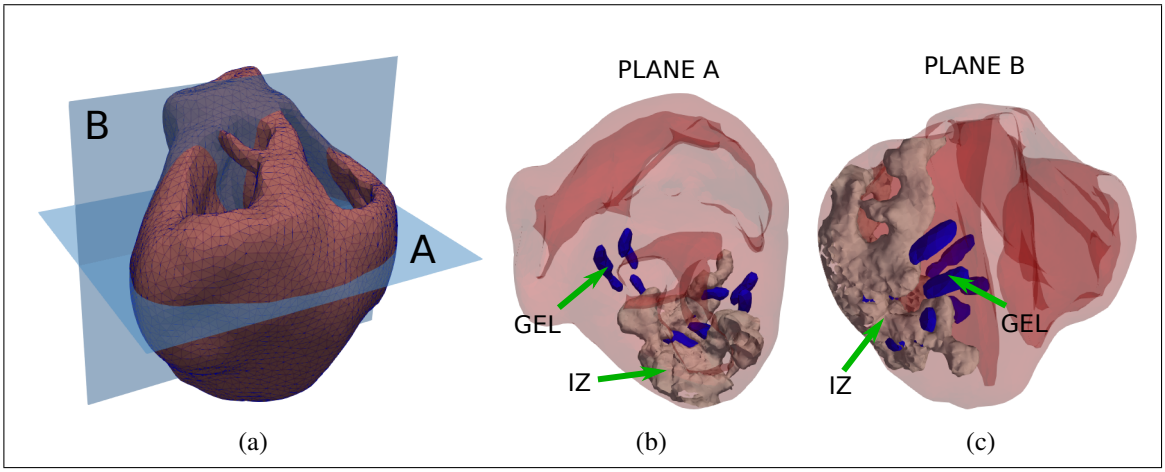

Figure 5.2. Detailed views of the heart-failure treated heart (HFI) in which biomaterial injection distribution is depicted in blue and infarcted regions are depicted in gray. Biomaterial injections are dispersed within the mid-myocardial left ventricle. Some injections are placed within the NZ region, and others are placed within the intersection of IZ and NZ regions.

5.2. Numerical modeling of cardiac electrical activity

The transmembrane ionic current is modeled according to the model proposed by ten Tusscher and Panfilov (TP06) (ten Tusscher & Panfilov, 2006) for ventricular human cells.

This model is fitted to reproduce APD restitution curves measured in humans, and have an extensive description of the intracellular calcium dynamics. It has been broadly used for the study of reentrant arrhythmia and electrical instability at cellular and tissue levels. In this model the ionic current density, defined as the sum of all transmembrane current densities, is given by

$$I_s = I_{Na} + I_{K1} + I_{to} + I_{Kr} + I_{Ks} + I_{CaL} + I_{NaCa} + I_{NaK} + I_{pCa} + I_{pK} + I_{bCa} + I_{bNa}, \quad (5.1)$$

where I_{NaCa} is Na^+/Ca^{2+} exchanger current, I_{NaK} is Na^+/K^+ pump current, I_{pCa} and I_{pK} are plateau Ca^{2+} and K^+ currents, and I_{bCa} and I_{nNa} are background Ca^{2+} and Na^+ currents. One advantage of using this model is that, by changing the parameter values it allows for the representation of transmural heterogeneity observed in myocardial tissue. To this end, the cardiac wall was divided into epicardial, mid-myocardial and endocardial layers using the distribution ratio $2 : 3 : 3$ as adopted in previous works (Corrias et al., 2010), see Figure 5.3. The set of parameters corresponding to each layer, which were used in this work for the simulation of the restitution protocol, have been reported elsewhere (ten Tusscher & Panfilov, 2006). For the simulation of VF, the parameter values reported in (Tusscher et al., 2007) were employed, which are included in Table 6.2. Initial values for the gating and internal variables are included in Table 6.3.

Section	G_{Kr}	G_{Ks}	G_{pCa}	G_{pK}	τ_f Inactivation
Midmyocardium	0.172	0.0515	1.8545	0.00073	$\times 2$
Epicardium	0.172	0.2205	1.8545	0.00073	$\times 2$
Endocardium	0.172	0.2205	1.8545	0.00073	$\times 2$

Table 5.1. Parameter values used in VF simulations with the TP06 model. Parameters not included in this table take the same values reported in (ten Tusscher & Panfilov, 2006). Parameters that where modified were the maximum conductance of the I_{Kr},I_{Ks}, I_{pCa} and I_{pK} currents. The time constant of the f gate was also modified.

V	-85.23	h	0.7444	f_{cass}	0.9953	$CaSR$	3.64
X_{r1}	0.00621	j	0.7045	s	0.999998	Ca_{ss}	0.00036
X_{r2}	0.4712	d	3.373×10^{5}	r	2.42×10^{-8}	Na_i	8.604
X_s	0.0095	f	0.7888	Ca_i	0.000126	K_i	136.89
m	0.00172	f_2	0.9755	R	0.9073		

Table 5.2. Initial conditions used for the TP06 model

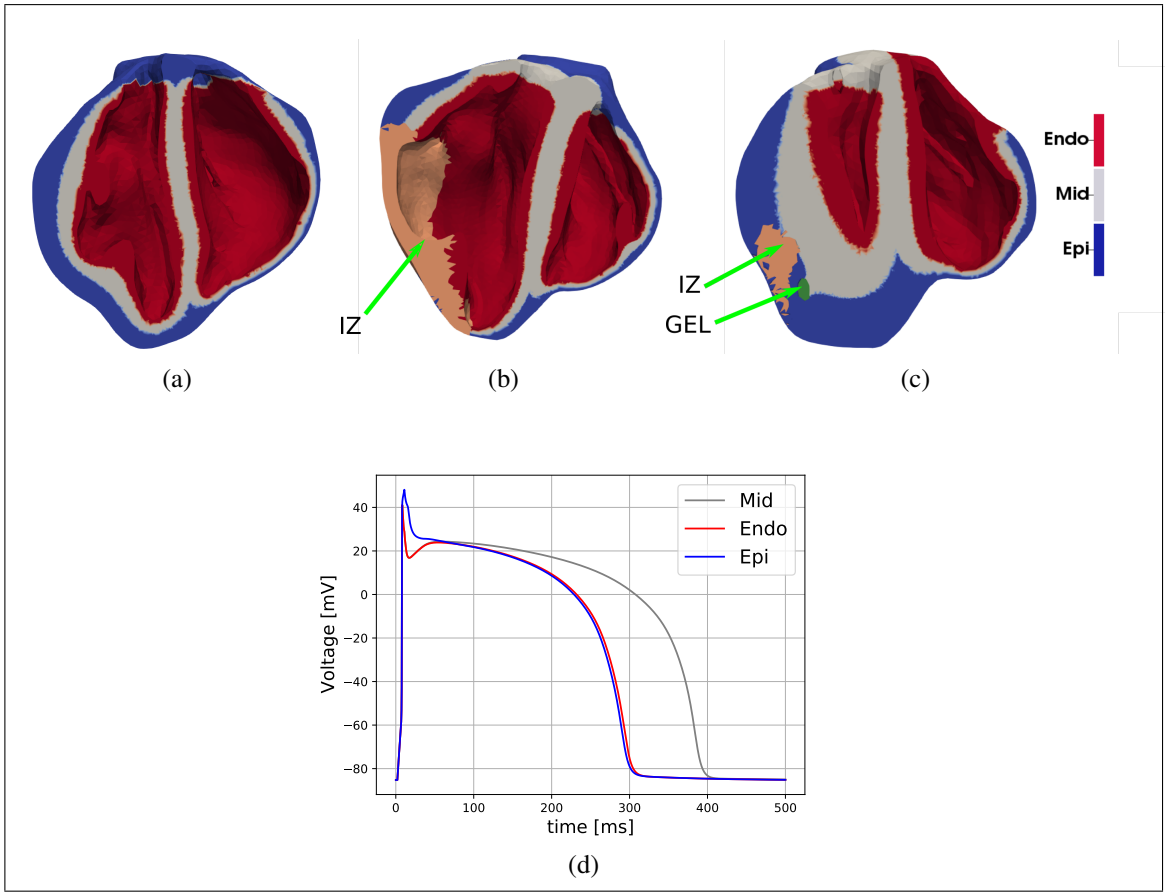

Figure 5.3. Hearts ventricles sections showing the endocardium (Endo), mid-myocardium (Mid), and epicardium (Epi) regions in (a) the NC model, (b) the HFC model, and (c) the HFI model. These domains are defined using a regional segmentation technique based on Laplace interpolations (Perotti et al., 2015). Each domain considers a specific cellular model for ionic transmembrane current. (d) Action potentials for the three type of cells considered in the construction of the heart models

The governing equations described in 3.57 are discretized in space using a standard Galerkin finite-element scheme (D. Hurtado & Henao, 2014), where linear tetrahedral elements are employed to approximate the transmembrane potential field. Time integration was performed using an operator splitting method (Sundnes et al., 2006). All numerical implementations were developed in Python, using the FENICS Project software and the *Cbcbeat* software collection in an in-house parallel computing platform. Given the well-known dependency of the conduction velocity to the mesh size, conduction velocity convergence was carried out for linear tetrahedral elements (Figure 5.4). In particular, we found that a characteristic mesh size of ≈ 0.8 mm provides a good approximation of the sought conduction velocity ($\approx 0.67\,\mathrm{mm/ms}$) at a normal pacing. This implies a set of nonlinear equations with over 7 million degrees of freedom. Time integration of gating evolution equations at quadrature points is performed using the explicit Rush-Larsen method with a time step of $dt = 0.1$ ms. Overall, 1 second of simulation required about 4.8 hours of computation using 62 CPU's within a parallel computing platform AMD Opteron^{TM} Processor 6378. For the APD restitution estimation, this meant a total of 81.6 hours for each heart, whereas VF simulations involved around 48.0 hours of computation for each heart.

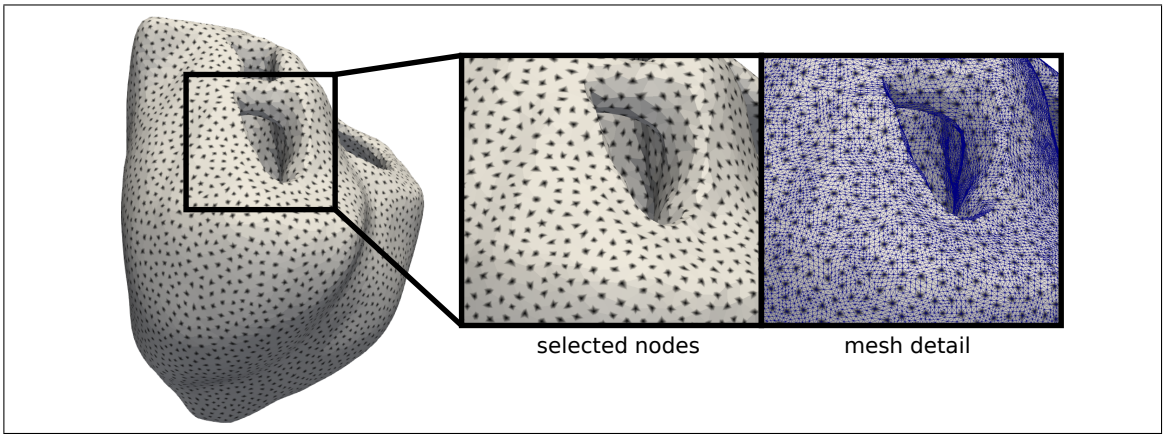

Figure 5.4. Detail of the nodes selected to compute the APD restitution curve (black dots) during simulation time, thereby reducing computational costs during post-processing. Regional distribution of the APD restitution is computed using the information taken from this set of nodes, which are selected based on unrefined meshes.

We developed in-house routines to post-process the simulation results to compute parameters such as activation (AT) and repolarization times (RT), during numerical simulations with a time step $dt^* = 5dt$ over selected nodes in the finite element mesh (Figure 5.4). The nodes were selected using information of unrefined meshes. This setup reduced computational costs, especially for post-processing purposes such as the APD restitution curve. Given the complex geometry of each model, we also performed region labeling for the different heart surfaces by using a Laplace interpolation approach. In particular, we computed APD restitution curves in the LV endocardium (LV), RV endocardium (RV), left ventricle mid-myocardium (LVMM), and epicardium (EPI) on a simple subdivision of the heart geometric features directly during simulations. Accordingly, we produced a probability density function (PDF) using a Gaussian kernel density approach to analyze the distribution of the APD restitution in these regions.

5.2.1. Simulation protocols and analysis

To compute the APD restitution distribution, the three heart models were paced at the apex location (see star in Figure 5.5) 32 times with varying pacing frequency. The total simulation time reached 17 s of physical time for each geometry model, with stimulus value of $40\,mV/ms$ and duration of $2\,ms$. At each pacing cycle length (CL), the APD was computed locally to obtain a regional distribution of the restitution curves. In particular, APD was computed for each selected node (see Figure 5.4) of the finite-element discretization and the PDF was estimated from this data (see Figure 5.6). For comparison purposes, the PDF was examined within the EPI, LV, RV and LVMM surfaces.

An S1-S2 protocol was implemented to induce VF in each heart model. The S1 stimulation site was the septum LV endocardium, while the S2 stimulus was delivered at the posterior zone of the epicardium, near the tail of the S1 wave. The timing between S1 and S2 was fine-tuned to obtain excitation wave-break, formation of a scroll-wave and evolution into VF. A vulnerable window was measured as the elapsed time between the S1 and

S2 pulses for which a sustained VF was achieved ($> 2s$). Given the structural differences (scar distribution) of each heart, different values for the S2 stimulus were needed. The S2 stimulus value was $300\,mV/ms$ (7.5 times the S1 stimulus value) for the NC heart, while for both HFC and HFI hearts the S2 stimulus value was around $220\,mV/ms$ (5.5 times the S1 stimulus value). The vulnerable window was $408ms, 406ms$ and $423ms$ for the NC, HFC and HFI heart, respectively. The complexity of activation patterns developed during VF dynamics was quantified by computing the number of rotors in time. These rotors are 3D scroll waves that rotate around a filament (Winfree, 1994; Panfilov & Pertsov, 2001b). Scroll wave filaments were distinguished using the algorithm proposed by Fenton and Karma (F. Fenton & Karma, 1998). In particular, a singular point is found by computing the intersection of an isopotential line (-70 mV) with the condition $dV_m/dt = 0$. In the computational model here implemented, each singular point is related to a single finite element. Afterwards, scroll wave singular line, e.g. filament, was identified and labeled by using a density-based spatial clustering algorithm (DBSCAN)(Ester et al., 1996). This method allows one to group elements that are closely packed together forming a specific filament. Each group (filament) formed is classified, updated and counted every $10\,ms$ of physical time directly during simulations.

The electrical properties of alginate hydrogel implants have not been reported to date, thus in the previous experiments we have assumed that its conductivity is zero. To assess the effect of gel conductivity on VF sustainability in the treated heart, we performed a sensitivity analysis where the biogel is assumed to behave as a passive conductor. VF simulations were performed assuming an isotropic conductivity in the gel of the form

$$\mathbf{D}_{gel} = cd_{\perp} \quad \text{in} \quad \Omega_{gel}, \tag{5.2}$$

where c is a conductivity ratio that modulates the conductivity of the gel based on the value used for transversely-isotropic propagation in normal cardiac tissue. Accordingly, for values of the conductivity ratio $c < 1$ the biomaterial region is less conductive than the normal tissue and for values of conductivity ratio $c > 1$ the biomaterial region is more

conductive than the normal tissue. We performed simulations for $c = \{0.0, 0.5, 1.0, 1.5\}$, and computed the number of rotors in each case to evaluate the spatiotemporal dynamics during VF. Pseudo-electrocardiograms (EGCs) were computed by estimating the surface potential using the approximation(Plonsey & Barr, 2007)

$$V_e = -\int_{\Omega} \nabla V_m \cdot \nabla \frac{1}{||\rho||} d\Omega, \quad \text{with} \quad \rho = |\mathbf{x}_e - \mathbf{x}|. \tag{5.3}$$

Here, $\rho \in \mathbb{R}^3$ defines the distance from each point of the heart to a point placed at some distance from the ventricles (i.e., electrode location). This position was established at $2\,cm$ away from the left ventricular wall, as is commonly defined to mimic pre-cordial leads to study T waves and QT intervals(Sahli Costabal et al., 2018). ECG signals were analyzed using Fourier Transform, from which power spectra were constructed, and the fundamental frequency was identified.

5.3. Results

A restitution protocol simulation was performed in three different computational heart models: a normal control heart (NC), a heart control with ischemic heart failure without biomaterial treatment (HFC), and a heart with ischemic HF and biomaterial injections (HFI). Figure 5.5 shows isochrone maps of the AT and APD, corresponding to the fifth stimulus delivered for all the three hearts. The spatial distributions of AT in the LV in all three cases look smooth and display a clear gradient along the apicobasal direction. The APD maps in the normal heart display a transmural heterogeneity associated to the three layers with different cell types included in the model, see Figure 5.3. The HFC and HFI cases display a stronger transmural dispersion in APD, with lower APD values towards the epicardium and endocardium than the NC case.

Given the heterogeneous distribution of the APD within the myocardium, the relation between the APD and the cycle length (CL) was computed for the surface of the epicardium (EPI), the left-ventricle endocardium (LV), right-ventricle endocardium (RV) and left-ventricle mid-myocardium (LVMM). Figure 5.6 displays these regions, as well as

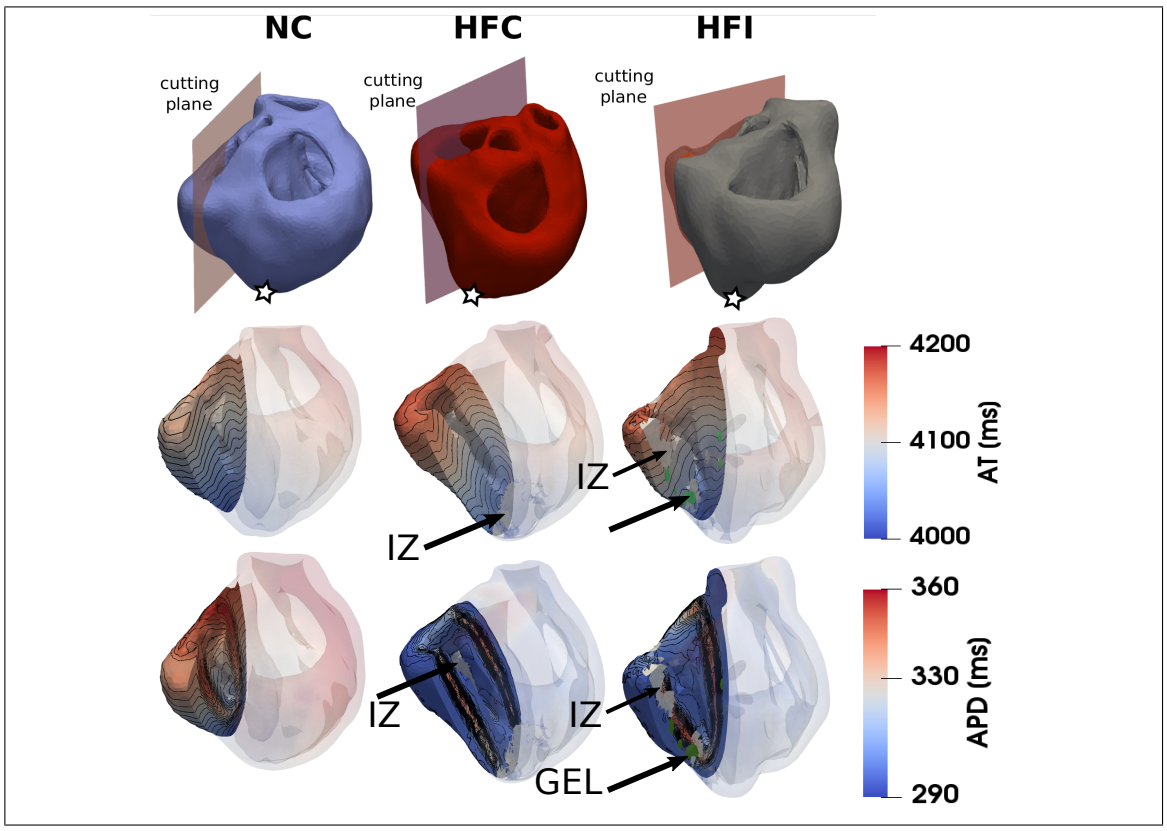

Figure 5.5. Spatial distribution of activation time (AT) and action-potential duration (APD) as measured after the fifth stimulus delivered at the apex. (Top row) computational model showing the biventricular geometry and cutting planes, with stimulation sites indicated with a star. (Middle row) AT maps for the selected cutting planes. (Bottom row) APD maps for the selected cutting planes. Infarcted zones (IZ) and bio-gel injections (GEL) are indicated with arrows.

the empirical probability density functions of the restitution curves on each of these surfaces. Each panel of Figure 5.6 also shows the grey zone ratio (GZR), defined as the area of grey zone over the total area of the surface under consideration. The GZR was large ($> 40\%$) in the LVMM and EPI surfaces of the HFI heart, and in the LVMM surface of HFC heart. The GZR was low ($\leq 10\%$) in all other surfaces, except for the EPI surface of the HFC heart. In all cases, restitution curves monotonically converged to APD = $250\,\mathrm{ms}$ as the CL approached a value of $350\,\mathrm{ms}$. In general, dispersion in APD increased as CL increased, with the largest dispersion found in the LVMM region in all three cases studied

for high CL values. Figure 5.7 shows APD empirical probability density functions for the particular case of CL$=$ $370\,\mathrm{ms}$. Qualitatively, all three heart models resulted in similar distributions of APD for the EPI and LVMM regions, while marked differences in the distribution shape were found for the NC case when compared to the HFC and HFI cases in the LV and RV regions. This trend is confirmed by comparing median values of the distributions, see Supplementary Table 1. A similar analysis on the distribution of APD for higher CL values confirms this trend, see Supplementary Figure 1.

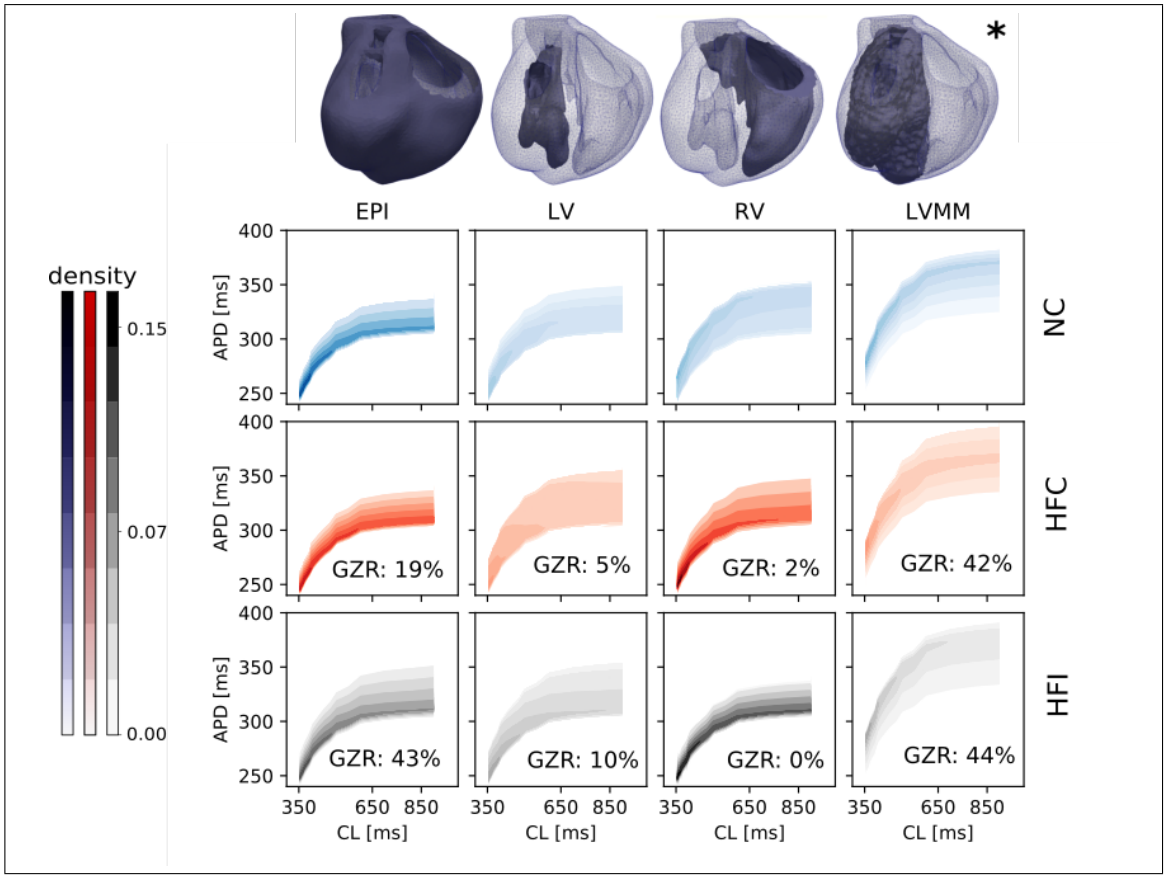

Figure 5.6. Restitution curve of the normal (NC), untreated (HFC) and treated (HFI) heart for the epicardial (EPI), left ventricle (LV), right ventricle (RV) and left ventricle mid-myocardium (LVMM) regions. Gray zone ratio (GZR)is reported for the HFI and HFC hearts. In general, higher dispersion of APD is found in the LVMM region.

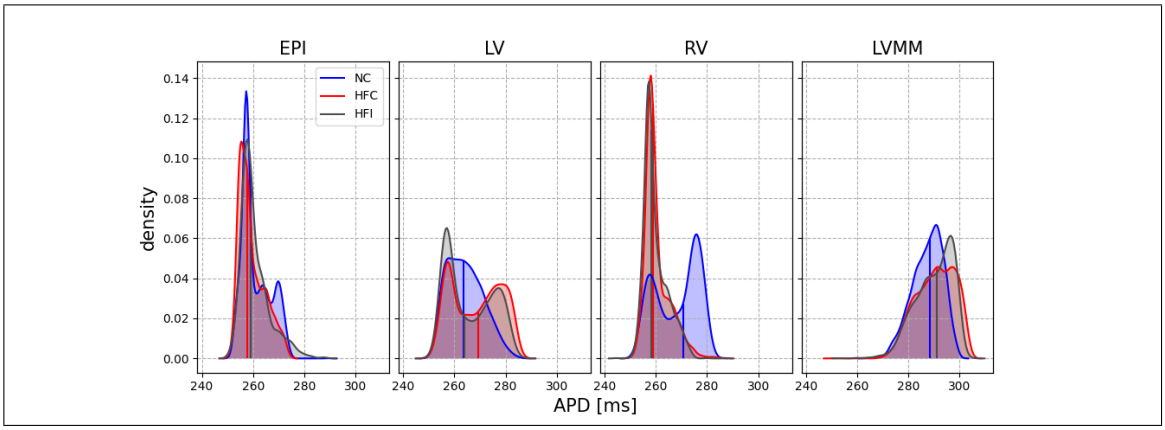

Figure 5.7. Empirical probability density functions of regional APD at CL= 370 ms. Median values are plotted with vertical lines. All three models result in similar distributions for the EPI and LVMM, while the NC case markedly differs from the HFC and HFI cases in the LV and RV regions.

We studied VF sustainability in all hearts via an S1-S2 stimulation protocol for induction of VF. Figure 5.8 shows the depolarized (excited) tissue during the temporal development of arrhythmia in the HFI model, highlighting how the number of scroll waves rapidly increases as the time progresses. To induce VF, increasing levels of injected currents were employed on the different hearts until multiple scroll waves were achieved. In our study, the ratio of the NC, HFC and HFI S1-S2 stimuli amplitude was 15:11:11, and the vulnerable window was $408ms, 406ms$ and $423ms$ for the NC, HFC and HFI subjects, respectively. To provide a quantitative indication of VF dynamics and sustainability, we assessed the time evolution of scroll waves by identifying the total number of 3D filaments at each time instant during a time window of 10 seconds, see Figure 5.9. In all cases, the number of filaments stabilized after roughly 2500 milliseconds. After that time, the NC, HFC and HFI subjects resulted in 27, 34 and 40 filaments, respectively.

To understand the potential impact of the electrical properties of gel injectates in VF sustainability, we performed a sensitivity analysis where the number of filaments during VF was studied for different levels of gel conductivity. We considered four levels of gel conductivity by setting $c = \{0.0, 0.5, 1.0, 1.5\}$, where c is defined as the ratio between the

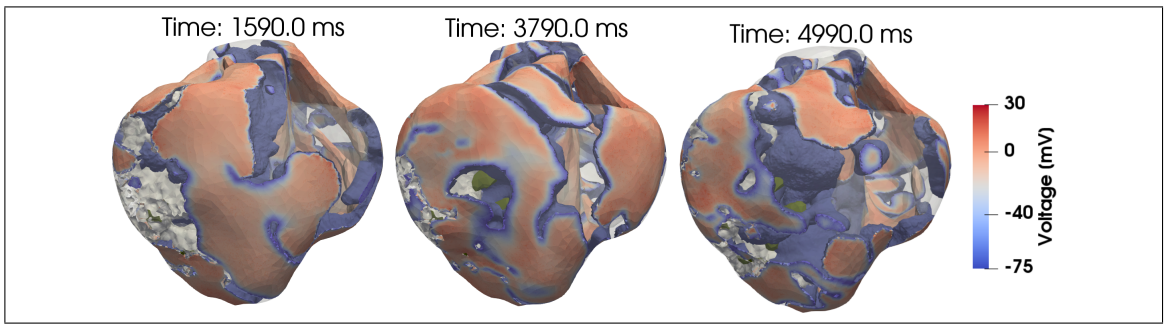

Figure 5.8. Temporal evolution of ventricular fibrillation in the HFI heart. Electrically-active regions ($V_m > -75.0\,mV$) are depicted according to the color scalebar. IZ is depicted in grey, and biomaterial injections are depicted in dark green. The S1 stimulation site is the septum LV endocardium, while the S2 stimulus is delivered at the posterior zone of the epicardium. Rotors rapidly increase in time, and constantly interact with regions where biomaterial injections are located.

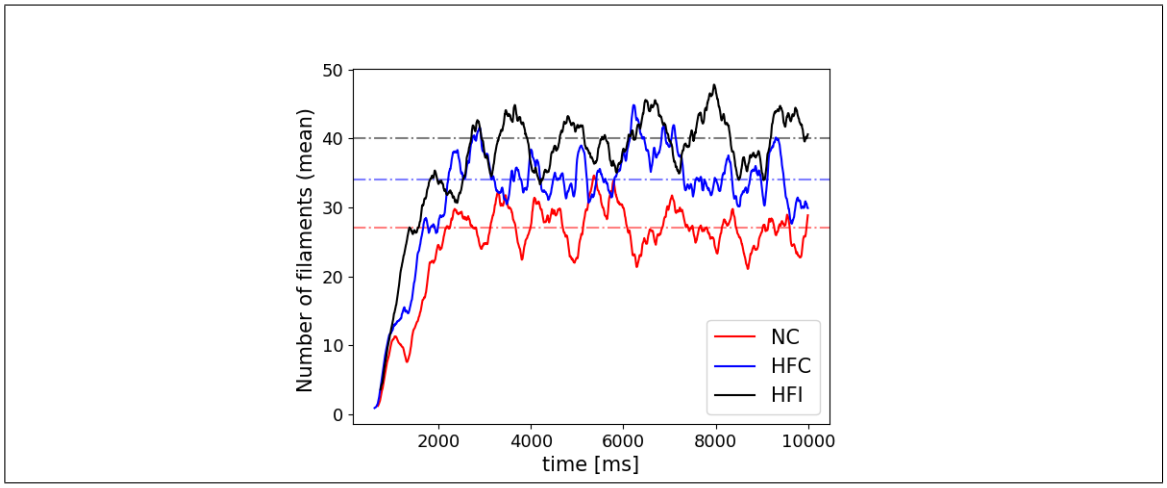

Figure 5.9. Evolution of the number of filaments for all three hearts (solid lines). Dashed lines correspond to the time-averaged number of filaments after the first 2500 miliseconds. The time-averaged number of filaments in the NC, HFC and HFI subjects was 27, 34 and 40, respectively.

gel conductivity and the normal tissue conductivity. Figure 5.10a shows the time evolution of the number of filaments for the HFI model where stabilization is achieved after 2500 milliseconds, resembling the convergent behavior observed in Figure 5.9. The average number of filaments after 2500 milliseconds found in these simulations was 40 for the cases of $c = \{0.0, 0.5\}$ and 38 for the cases of $c = \{1.0, 1.5\}$. Pseudo-ECGs for all cases

are reported in Figure 5.10b, where the fundamental frequency was $4.3\,\mathrm{Hz}$ in all cases, regardless of the biogel conductivity assumed. The volume of the injected biomaterial represented roughly 3% of the heart total conductive volume.

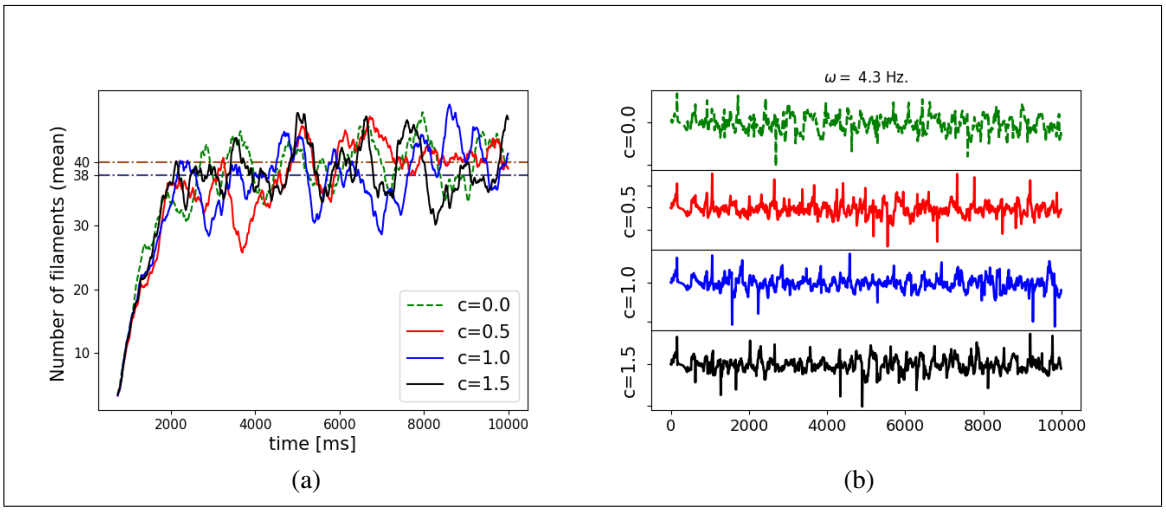

Figure 5.10. (a) Time evolution of the number of filaments during VF simulations of the HFI model for varying levels of electrical conductivity of the gel injections, parameterized by the value of the c ratio. The average value after 2500 miliseconds is depicted with dashed lines. There are not substantial differences between each case: the average number of filaments after 2500 milliseconds found in these simulations was 40, 40, 38 and 38 for the cases of gel conductivity ratios of 0.0, 0.5, 1.0 and 1.5, respectively. (b) Pseudo-ECG computed for each case.

5.4. Discussion

In this work, we develop computational models of the electrical behavior of the heart to study of the influence of biomaterial injection therapy on the arrhythmic behavior of failing hearts. We successfully developed a robust and computationally-efficient method that allows high-resolution subject-specific MRI and DT-MRI data to be used to evaluate the regional distribution of the APD restitution curve and the number of filaments formed during VF of control and treated hearts. We note that our study represents a proof-of-concept study with only one subject per group, and therefore is not sufficiently powered to

make inter-group conclusions. Despite this limitation, it represents a unique effort to understand how the dispersion of repolarization and VF dynamics behavior change in failing hearts treated with alginate hydrogel injections, as no electrophysiological studies for this treatment have been reported to date.

Simulations of standard restitution protocols suggest that there are important differences in the spatial distribution of AT and APD between the normal heart and both hearts with ischemic HF, treated and untreated. Spatial heterogeneity in the APD was observed in all three hearts, with a marked transmural gradient that can be explained by the use of different ionic cellular models for the endocardium, mid-myocardium and epicardium regions in the heart, see Figure 5.5 and Figure 5.3. The regional heterogeneity in APD can be also confirmed from the empirical probability density functions sampled from the restitution curves in selected regions in the heart, see Figure 5.6. In all cases, the largest APD mean values and dispersion were found at the LVMM region, which can be partly explained by the larger APD displayed by mid-myocardial cells, see Figure 5.3. Despite the fact that the LVMM presented the highest ratios of gray zones in HF hearts, the APD probability distributions did not seem to be affected when comparing normal and failing hearts, a trend that is confirmed when analyzing the APD distributions for different values of CL during restitution protocols in this same region, see Figure 1 in the Supplementary Materials. In contrast, the LV and RV regions in the HFC and HFI subjects markedly differed from the NC subject.

In the LV region, failing hearts displayed a bimodal distribution with higher dispersion (standard deviation) and median APD than the normal heart, which displayed a unimodal distribution. An inverse trend was found in the RV region, where the normal heart resulted in a bimodal distribution with higher median and dispersion than both the untreated and treated failing hearts, which displayed unimodal distributions, see Table 1 and Table 2 in the Supplementary Materials.

These findings suggest that, while the development of HF does result in marked changes in the dispersion of repolarization, the use of biogel injection treatment does not seem to affect the spatial dispersion of APD in failing hearts. Further, we attribute the differences in dispersion of repolarization in failing hearts when compared to the normal case to the remodelling that typically takes place after MI. This conclusion is supported by previous work using 2D simulations of cardiac tissue under an S1-S2 protocol, where the dispersion of APD was correlated with the formation of abnormalities in the electrical activity, such as VT. In these simulations, regions with altered restitution properties co-localized with zones with wave break and reentry (Clayton & Taggart, 2005; Weiss et al., 2010). Figure 5.6 shows that the restitution curve distribution at small CL values preserves a similar behavior for all hearts. This is an important observation since an anomalous behavior of the restitution curve at lower CL values is related to the formation of action-potential alternants and consequent wavebreaks (F. H. Fenton & Karma, 1998; F. H. Fenton & Cherry, 2002; Cherry & Fenton, 2004). For instance, experimental studies in human hearts with different stages of cardiomyopathy have shown that altered dynamics of the restitution curve at high pacing frequencies lead to electrical instabilities (Koller et al., 2005).

We have studied the VF dynamics in normal, untreated HF and treated HF subjects. In all three cases, we reached conditions for inducing and sustaining fibrillation by varying the location and duration of the excitation. We note that the injected current needed to induce VF in the NC case was considerably higher than in the HFC and HFI cases, which is consistent with experimental and clinical observations. During the sustained fibrillation regime, the average number of filaments in the HFC and HFI hearts stabilized around 34 and 40, respectively (Figure 5.9). The NC heart reaches a markedly lower value of 27 filaments during sustained VF. These results show that untreated and treated failing hearts resulted in increased VF sustainability when compared to a normal heart. Further, the larger number of filaments in the HFI subject compared to the HFC subject suggests that the biogel treatment can result in higher VF sustainability than that expected for untreated failing hearts. This observation has important implications in the development

of biomaterial-based treatments, especially when considering defibrillation procedures. Computational investigations have shown that a successful defibrillation process requires less energy when fewer filaments are present within the tissue (Plank, Leon, Kimber, & Vigmond, 2005). Since the HFI resulted in a larger number of filaments than the HFC heart, higher defibrillation-energy levels may be required in treated hearts (Luther et al., 2011). Since ischemic HF biomaterial-treated hearts are already at high risk of developing arrhythmias, these results provide crucial knowledge to be considered in the experimental design of defibrillation treatment of hearts with gel injectates.

A mechanistic explanation of the higher sustainability of VF observed in treated and untreated hearts can be supported by the changes in dispersion of repolarization resulting from remodeling. Post-MI HF results in marked alterations in key structural features of the heart such as cardiomyocyte principal orientation as well as changes in the cardiac volume (K. L. Sack, Aliotta, Choy, et al., 2018). These features induce a higher dispersion of repolarization, materialized in our case in critical changes in the distribution of APD in the RV and LV regions. Bimodality of the LV provides a wider substrate for discordant alternans and wavebreaks because of the larger volume of conductive mass available in the LV that can accommodate a large number of spiral waves (Gray et al., 1995). We remark that such an information is not directly inferrable from classical restitution curves, usually quantified only at specific locations, but it is crucial to connect the analysis of APD restitution distributions with an intrinsic spatial feature (electrotonic and memory effects) given by the spiral core filament in our analysis (Cherry & Fenton, 2004; ten Tusscher & Panfilov, 2006; Clayton et al., 2011).

In the first set of simulations, we treated biomaterial injections as non-conductive regions within the myocardium, which may not be the case for a biocompatible material. To assess the validity of this assumption, we developed a sensitivity analysis study where

injections within the myocardium were varied to understand the effect of gel conductivity in our results. We found that gel conductivity does not alter VF dynamics, as shown in Figure 5.10a. This result is further supported by the pseudo-ECG simulation reported in Figure 5.10b, where we found a fundamental frequency that does not depend on the level of gel conductivity. Further investigations concerning the conductivity properties of biomaterial injections are needed in order to fully characterize their significance in different electrophysiological models and multiple clinical conditions. For instance, biohybrid hydrogels composed of collagen, alginate and poly:polystyrene sulfonate have shown to be electroconductive, preventing arrhythmia in cardiac tissue constructs from neonatal rat hearts (Roshanbinfar et al., 2018).

This work has limitations that should be addressed in future extensions. An important limitation is that only one subject per group was considered, which is largely justified by the high computational burden, both in wall-clock time and in required infrastructure, that each simulation demands. While each group necessitates a larger population in order for the results to be statistically meaningful, we remark that the aim of this work is to present a proof-of-concept study that demonstrates the feasibility of performing pre-clinical studies of biomaterial injection in-silico. In particular, our results can be used as preliminary data in the design of future computational studies. In such an effort, the electrophysiological cellular model will require dedicated measurement and fine-tuning of the restitution parameters to set the spatiotemporal dynamics within a patient-specific framework. Further, it is worth noting that the behavior of interfaces between healthy myocardial tissue and gel biomaterials necessarily imply alterations in the local reaction dynamics and conduction properties, which currently remains an open topic from the experimental and theoretical perspectives (Choy et al., 2018). These alterations may resemble the situation of border zones located near the boundary of the IZ, where strong cardiac remodelling is observed. These border zones reportedly play a meaningful role in the propagation of action potentials, since they may promote the formation of abnormalities such as action potential alternans (Gizzi et al., 2013) and arrhythmias (Mendonca Costa et al., 2018). While recent

multiscale models of cardiac tissue have been able to theoretically link the remodelling of gap-junction conductivity with reduced conduction velocity in cardiac tissue (D. E. Hurtado, Jilberto, & Panasenko, 2020), further studies should quantify in biophysical terms the level of remodelling found at the gel-intact tissue interface, in order to incorporate additional nonlinearities in the emerging cardiac behavior (D. Hurtado, Castro, & Gizzi, 2016; Cherubini, Filippi, Gizzi, & Ruiz-Baier, 2017; Lenarda, Gizzi, & Paggi, 2018; Loppini et al., 2019). Another limitation is the absence of electromechanical coupling in our simulations. Because Algisyl-LVR^{TM} injection treatments are specifically developed to deliver passive mechanical support to the ventricle, the electromechanical coupling plays a decisive role to examine the overall performance of treated hearts. Computational models that incorporate electromechanical coupling have become increasingly relevant given the role of deformation in the local electrical behavior and spatial propagation of electrical impulses, particularly in VF dynamics (Land & et al., 2015; D. E. Hurtado, Castro, & Madrid, 2017; Quarteroni et al., 2017; Costabal, Concha, E.Hurtado, & Kuhl, 2017; Christoph et al., 2018). Therefore, future efforts should include electromechanical coupling in order to better characterize the behaviour of biomaterial-treated hearts, at the expense of increasing the computational costs.

Future work may help to elucidate how biomaterial injection treatments can be enhanced such that the overall function of HF hearts could be improved without affecting their electrical performance. For instance, future efforts could focus on understanding how the distribution of injections can affect the electrophysiological behavior of treated hearts. Recent studies show that the volume and location of biomaterial injections correlate with the reduction of pathological conditions within the heart (Wall, Walker, Healy, Ratcliffe, & Guccione, 2006). Another avenue of research is to extend the current simulations to include electrophysiological models that could take into account the multiscale nature of the myocardial tissue, and muscle contraction.

6. ON THE EFFECT OF IONIC MODELING IN THE DISPERSION OF REPOLARIZATION AND SUSTAINABILITY OF VENTRICULAR FIBRILLATION: A COMPARISON STUDY

This chapter is an adapted transcription of the article "On the Role of Ionic Modeling in the Signature of Cardiac Arrhythmias for Healthy and Diseased Hearts" *submitted to the Special Issue "Mathematical Modeling in Biomechanics and Mechanobiology" of Mathematics 2020, 8(12), 2242.*

Recent developments in computational modeling of the heart's bio-electrical activity have established the most highly detailed example of a virtual organ (N. A. Trayanova, 2011; N. A. Trayanova & Chang, 2016a; Dierckx et al., 2019). These advances are due to the significant progress achieved in cardiac cell modeling, corroborated with experimentation and clinical practice. Besides, due to the continuous increment in computational power, whole-heart electrical models have shown promising translational outcomes, improving the general understanding of the heart function, its pathologies, and therapies (Quarteroni et al., 2017; Kaboudian, Cherry, & Fenton, 2019; Kariya et al., 2020; Viola, Meschini, & Verzicco, 2020; Ramirez, Gizzi, Sack, Guccione, & Hurtado, 2020). Still, critical modelling challenges arise when local heterogeneities at different spatio-temporal scales are taken into account (D. Hurtado et al., 2016; Loppini et al., 2018, 2019; Cusimano, Gizzi, Fenton, Filippi, & Gerardo-Giorda, 2020; Propp, Gizzi, Levrero-Florencio, & Ruiz-Baier, 2020; D. E. Hurtado et al., 2020).

Various approaches have been proposed to simulate complex electrical behaviour of the heart, e.g., ventricular arrhythmias. First, detailed cell models, with highly accurate and validated biophysical relationships representing the ground truth, have been incorporated to improve the physiological relevance of in silico cardiac predictions. Nonetheless, these approaches may result computationally demanding, further requiring advanced optimization tools (Barone et al., 2017; Peirlinck et al., 2019; Barone, Gizzi, Fenton, Filippi, & Veneziani, 2020; Niederer et al., 2020). Alternatively, reduced phenomenological models were developed, preserving the main features of physiological approaches, but still allowing for a robust in silico investigation. Depending on the application at hand, one of

the two options is favorable, identifying the specific characters that minimize alterations of the final results (Clayton et al., 2011). This is especially true in the study of abnormal electrical waves, e.g., ventricular tachycardia (VT) and ventricular fibrillation (VF), in healthy and diseased conditions (Ten Tusscher et al., 2009).

The computational cardiology literature is populated by a plethora of biophysical models that describe the electrical behavior of the human myocardium. A detailed description of ion channels, pumps, and exchangers is usually included to explain experimental observations (F. H. Fenton & Cherry, 2008). However, many parameters are highly difficult or nearly impossible to measure in vivo, and different formulations have been shown to replicate similar dynamics. For example, the O'hara Rudy dynamic (Ord) model (41 variables, 16 parameters) and the Ten Tusscher-Panfilov 2006 (TP06) model (19 variables, 48 parameters) produce similar electrical behaviors (O'Hara, Virág, Varró, & Rudy, 2011; ten Tusscher & Panfilov, 2006; Abbasi & Clayton, 2013). In addition, the multiple time scales involved in the formulation, from ms to s, make the resulting system of equations stiff and challenging to solve numerically. Alternatively, phenomenological models derive from the overall description of cumulative inward and outward currents across the cell membrane and rely on a smaller set of variables. For instance, the Fenton-Karma (FK) model (3 variables, 14 parameters) and its later extensions (minimal model–4 variable, 28 parameters) (F. Fenton & Karma, 1998; Bueno-Orovio et al., 2008) are well-known instances of simplified phenomenological descriptions able to reproduce several dynamical properties of the cardiac electrical activity: threshold of excitation, maximum upstroke velocity, action potential (AP) shape and morphology, restitution properties, action potential duration (APD) and alternans dynamics (F. H. Fenton, Cherry, Hastings, & Evans, 2002; F. H. Fenton, Gizzi, Cherubini, Pomella, & Filippi, 2013). Increased numerical efficiency is enforced, lacking detailed ionic descriptions, although well-suited for large-scale whole-heart numerical studies.

Cardiac arrhythmias, such as VT and VF, have been studied in detail using physiologically-based computational approaches. Various cardiac diseases, such as long-QT syndrome or

Brugada Syndrome, have been elucidated using advanced computational techniques (Ten Tusscher et al., 2007; Zhou et al., 2018; Roberts et al., 2012). Besides, computational cardiology modeling has been used to explain the relation between AP shape changes with the likelihood of a reentrant arrhythmia (see e.g. (Clayton et al., 2011) and references therein). Subject-specific whole-heart computational models explored arrhythmia risk stratification in patients with myocardial infarction (MI) (N. A. Trayanova & Chang, 2016b; Ramirez et al., 2020), and complex VF dynamics have also been characterized in terms of scroll wave filaments through detailed ventricular models (Tusscher et al., 2007). Likewise, the study of AP vortex dynamics has been conducted via phenomenological descriptions in whole-heart simulations (Clayton & Holden, 2004; Cherry & Fenton, 2008).

Regardless of such rich literature, in this chapter, we propose a novel extended comparison among phenomenological and biophysically-based approaches considering subject-specific whole-heart geometries in healthy and MI cases. In particular, we develop a robust finite element computational framework investigating similarities and differences between FK and TP06 formulations during physiological and pathological electrical dynamics. High-resolution geometry models, reconstructed from DT-MRI swine hearts dataset, are used to evaluate statistical descriptions of AP restitution properties and VF dynamics. We consider the different local electrical properties of the healthy and infarcted myocardium (epicardium, mid-myocardium, endocardium, and transition zones or grey zones (N. A. Trayanova & Chang, 2016b; Gokhale, Medvescek, & Henriquez, 2017; Zhou et al., 2018)), further including image-based myocardial fiber orientations. We compute classical features of cardiac excitation, e.g. CV and APD restitution curves, also generalizing APD measures over specific anatomical surfaces introducing a novel statistical description. Moreover, we quantify multiple well-recognized VF signatures, such as the number of filaments and pseudo-ECG fundamental frequency during sustained VF. We aim to show that FK ionic model can reproduce VF signatures predicted by TP06 model in both normal and failing hearts using a fraction of the computational effort, despite the apparent differences in repolarization.

6.1. Methods

6.1.1. The Fenton-Karma model

The Fenton-Karma (FK) model is a 3-variable phenomenological model developed to study arrhythmogenesis in cardiac tissue reproducing restitution properties and spiral wave dynamics by using a minimal set of field variables (F. Fenton & Karma, 1998). Model equations are formulated in dimensionless form, defining the nondimensional membrane potential $u = (V - V_0)/(V_{fi} - V_0)$, and scaling the ionic currents as $J_X = I_X/(C_m(V_{fi} - V_0))$, with units of inverse of time. According to the monodomain approach, Eq.s (3.57) becomes

$$\frac{\partial u}{\partial t} = \nabla \cdot (\mathbf{D}\nabla u) - J_{fi}(u, v) - J_{so}(u) - J_{si}(u, w) + J_{stim}, \tag{6.1a}$$

$$\frac{dv}{dt} = H(u_c - u)(1 - v)/\tau_v^- - H(u - u_c)v/\tau_v^+, \tag{6.1b}$$

$$\frac{dw}{dt} = H(u_c - u)(1 - w)/\tau_w^- - H(u - u_c)w/\tau_v^+ , \tag{6.1c}$$

where

$$J_{fi}(u, v) = -v\, H(u - u_c)(1 - u)(u - u_c)/\tau_d, \tag{6.2a}$$

$$J_{so}(u) = u\, H(u_c - u) + \frac{1}{\tau_r} H(u - u_c)/\tau_0, \tag{6.2b}$$

$$J_{si}(u, w) = -w(1 + \tanh[k(u - u_c^{si})])/(2\tau_{si}), \tag{6.2c}$$

$J_{stim} = J_{stim}(t)$ represents the external electrical impulse, and $H(x)$ is the Heaviside step function defined as $H(x) = 1$ for $x \geq 0$ and $H(x) = 0$ for $x < 0$. Different parametrizations of the FK model have been proposed (Courtemanche et al., 1998; Oliver & Krassowska, 2005). In the present contribution we refer to (F. Fenton & Karma, 1998), with model parameters provided in Table 6.1 below.

u_c	u_v	$\bar{g}_{fi}$	τ_{v1}^-	τ_{v2}^-	τ_v^+	τ_0	τ_r	k	τ_{si}	u_{csi}	τ_w^-	τ_w^+	C_m
0.13	0.04	4	1250	19.6	3.33	12.5	33.33	10	29	0.85	41	870	1

Table 6.1. Parameters used in the FK electrophysiologycal model.

6.1.2. The TenTusscher-Panfilov 2006 model

The TenTusscher-Panfilov 2006 (TP06) model is a 19-variable physiological model that includes an extensive description of the intracellular calcium dynamics and well-reproduces cardiac action potentials of human epicardial, endocardial, and mid-myocardial cells (ten Tusscher & Panfilov, 2006). In this case, the sum of ionic currents is defined as

$$I_{ion} = I_{Na} + I_{K1} + I_{to} + I_{Kr} + I_{Ks} + I_{CaL} + I_{NaCa} \tag{6.3}$$

$$+I_{NaK} + I_{pCa} + I_{pK} + I_{bCa} + I_{bNa} + I_{stim}\,, \tag{6.4}$$

where I_{NaCa} is the Na^+/Ca^{2+} exchanger current, I_{NaK} the Na^+/K^+ pump current, I_{pCa} and I_{pK} are the Ca^{2+} and K^+ plateau currents, and I_{bCa} and I_{nNa} are the background Ca^{2+} and Na^+ currents. The description of each current and related gating variables are provided in Table 6.2 together with model parameters and initial conditions in Tables 6.2 and 6.3.

Section	G_{Kr}	G_{Ks}	G_{pCa}	G_{pK}	τ_f Inactivation
Midmyocardium	0.172	0.0515	1.8545	0.00073	$\times 2$
Epicardium	0.172	0.2205	1.8545	0.00073	$\times 2$
Endocardium	0.172	0.2205	1.8545	0.00073	$\times 2$

Table 6.2. Parameter values used during VF simulations for the TP06 model. Parameters not included in this table take the same values reported in (ten Tusscher & Panfilov, 2006). Modified parameters are the maximum conductance of the I_{Kr},I_{Ks}, I_{pCa} and I_{pK} currents. The time constant of the f gate was also modified.

Layer-specific electrophysiological properties are included in this model through the transient outward and slow delayed rectifier currents. In particular, epicardial cells show

V	-85.23	h	0.7444	f_{cass}	0.9953	$CaSR$	3.64
X_{r1}	0.00621	j	0.7045	s	0.999998	Ca_{ss}	0.00036
X_{r2}	0.4712	d	3.373×10^{5}	r	2.42×10^{-8}	Na_i	8.604
X_s	0.0095	f	0.7888	Ca_i	0.000126	K_i	136.89
m	0.00172	f_2	0.9755	R	0.9073		

Table 6.3. Initial conditions used for the TP06 model

higher I_{to} current (via G_{to}) and higher inactivation recovery (via τ_s). Differently, mid-myocardial cells are characterized by a lower $I_{\mathrm{K}s}$ current.

6.1.3. Stimulation protocols and post-processing

We compute APD restitution distribution for both ionic models by applying repetitive electrical stimulations at the apex of the bi-ventricular heart models (see S1 location in Fig.6.1) with varying pacing frequency. The total stimulation time corresponded to 17 s of physical time (32 electrical stimulations) for each case. At every pacing cycle length (CL), the APD was computed locally to obtain a regional distribution of the restitution curves. An empirical probability distribution function (PDF) was estimated then using APD data extracted from selected nodes of the finite-element discretization. Activation and repolarization times were obtained from unrefined mesh data and interpolated over the finite element discretization.

We further implemented an S1-S2 stimulation protocol to induce a sustainable VF within each bi-ventricular heart geometry. For the TP06 model, we identified the S1 stimulation site on the LV endocardium and delivered the S2 stimulus on the posterior epicardium layer. For the FK model, the S1 stimulation site was identified on the apex, while the S2 stimulus was delivered on the anterior epicardial surface (see Figure 6.1). The S2 stimuli were selected on different locations depending on the ionic model, given the differences in conduction velocity. The effects of the initial site on VF formation have been studied previously in dog and human heart geometries, concluding that although the stimulation site may affect VF onset, the number of filaments (e.g. VF signatures) reach

the same steady-state value (Clayton & Holden, 2004; Ten Tusscher et al., 2009). We calculated the vulnerability window for each electrophysiological model by measuring the elapsed time between the S1 and S2 pulses for cases that resulted in sustained ventricular fibrillation (i.e., VF duration $> 2s$). To further characterize VF dynamics, we computed scroll wave filaments evolution during $10\,\mathrm{s}$ of physical time with a time step of 10 ms. After identification of the intersection between an isopotential line ($-70\,\mathrm{mV}$) and the constraint ${}^{dV_m}/_{dt} = 0$, each intersection was related with a finite element and filaments were labeled and counted using a density based clustering algorithm. Finally, to assess the global behavior of cardiac simulations, pseudo-ECG were computed to study VF signatures such as the fundamental frequency for all of the ionic models analyzed

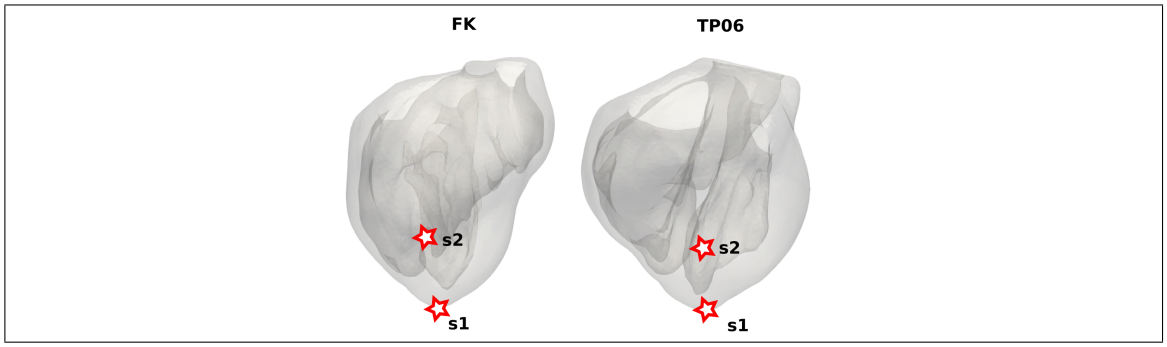

Figure 6.1. Location of the S1 and S2 stimuli for the different electrophysiological models used in this study.

6.2. Results

6.2.1. Dispersion of APD restitution

APD restitution curves were computed for the two electrophysiolgical models over four selected cardiac surfaces (see Fig. 6.2a): epicardium (EPI), left ventricular endocardium (LV), right ventricular endocardium (RV), left ventricular mid-myocardium (LVMM). Accordingly, a numerical probability density function (PDF) of the action potential duration was derived for each anatomical region both for NC and HFC geometry models. The eight distributions of restitution curves computed are shown in Fig.s 6.2b and

6.2c. For comparison purposes, APDs were normalized according to the formula $\mathrm{APD}_n = {}^{(\mathrm{APD}-\mathrm{APD}_{\min})}/_{(\mathrm{APD}_{\max}-\mathrm{APD}_{\min})}$, where, $\mathrm{APD}_{\min}$ and $\mathrm{APD}_{\max}$ are provided in Tab. 6.4-a for each anatomical surface.

In the FK case, APD_n distributions stabilize around 0.78 ± 0.07 for CL ≥ 500, whereas, in the TP06 case, PDF restitutions show different average values and a non-uniform variance. Besides, a steeper and narrower distribution is observed for the FK model for CL < 400 ms while a gradual reduction can be noted for TP06. Interestingly, the FK distribution display peaks at the center of the distributions that remain stable during the whole restitution curve. The four anatomical surfaces show similar trends in both healthy and diseased conditions. Unlike, TP06 presents a strong dependence of the distribution peaks on the selected region. In particular, LV and RV surfaces show severe differences among NC and HFC models. Moreover, the left ventricle shows the highest dispersion of repolarization, i.e. higher variance, in the pathological case. Mean and standard deviations of the distributions are provided in Tab. 6.4-b for CL $= 400$ ms. Using 62 CPU's within a parallel computing platform, the restitution protocol simulation took around 55 hours and 82 hours of wall-clock to compute for the FK and TP06 model, respectively.

6.2.2. VF sustainability

We studied cardiac arrhythmias signature implementing an S1-S2 stimulation protocol to induce sustained VF, i.e., multiple scroll wave formations. Figure 6.4 shows a qualitative visual assessment of the scroll wave evolution for the two ionic models within the HFC geometry. Three selected times of transmembrane activation, $V_m > -75$ mV, are compared where the intramural transparency of the excitation highlights both the complexity of the dynamics and the differences among the two ionic models (Fig. 6.4a for FK and Fig. 6.4b for TP06). It is worth noticing the ratio of the amplitude for the two S1-S2 stimuli. The FK model sufficed an equal $1:1$ ratio with a vulnerable window of 345 ms in both NC and HFC subjects. In contrast with this, the TP06 model required a much higher

(a)

	FK	**TP06**
$\text{APD}_{\min}$	250 ms	250 ms
$\text{APD}_{\max}^{EPI}$	273 ms	335 ms
$\text{APD}_{\max}^{LV}$	273 ms	350 ms
$\text{APD}_{\max}^{RV}$	273 ms	350 ms
$\text{APD}_{\max}^{LVMM}$	273 ms	390 ms

(b)

	FK 400 ms			
	NC		**HFC**	
	Avg	**SD**	**Avg**	**SD**
EPI	0.40	±0.07	0.38	±0.08
LV	0.41	±0.08	0.40	±0.06
RV	0.38	±0.07	0.41	±0.07
LVMM	0.40	±0.05	0.40	±0.06
	TP06 400 ms			
	NC		**HFC**	
	Avg	**SD**	**Avg**	**SD**
EPI	0.30	±0.08	0.28	±0.07
LV	0.30	±0.08	0.34	±0.11
RV	0.34	±0.10	0.25	±0.06
LVMM	0.40	±0.05	0.42	±0.06

Table 6.4. (a) Normalization values for the FK and TP06 models. (b) APD mean (Avg) and standard deviation (SD) for CL $= 400$ ms, see Fig. 6.3.

stimulation amplitude ratio of $11 : 2$ for the NC case and $15 : 2$ for the HFC case, with a higher vulnerable window of 408 ms.

To provide a quantitative indication of VF dynamics and sustainability, we assessed the time evolution of scroll waves by identifying the total number of 3D filaments during 10 seconds of physical time (see Fig. 6.5a). Employing the same computational settings adopted for the restitution protocol, the VF wall-clock time was 34 and 48 hours for FK and TP06 model, respectively.

Similarities are observed among the two ionic models in terms of rolling averages computed with a time window of 500 ms. In all cases, the number of filaments stabilizes after about 2.5 s from arrhythmias induction (see Fig. 6.5b). FK and TP06 models revealed a mean value of filaments equal to $24/34$ and $27/34$ for NC/HFC, respectively. Besides, we provide mean and variance, maximum and minimum values in Tab. 6.5 comparing ionic and geometry models. The L_1 error between the mean number of filaments among FK and TP06 was 12.2% and 9.6% for NC and HFC, respectively. Additionally, the application of

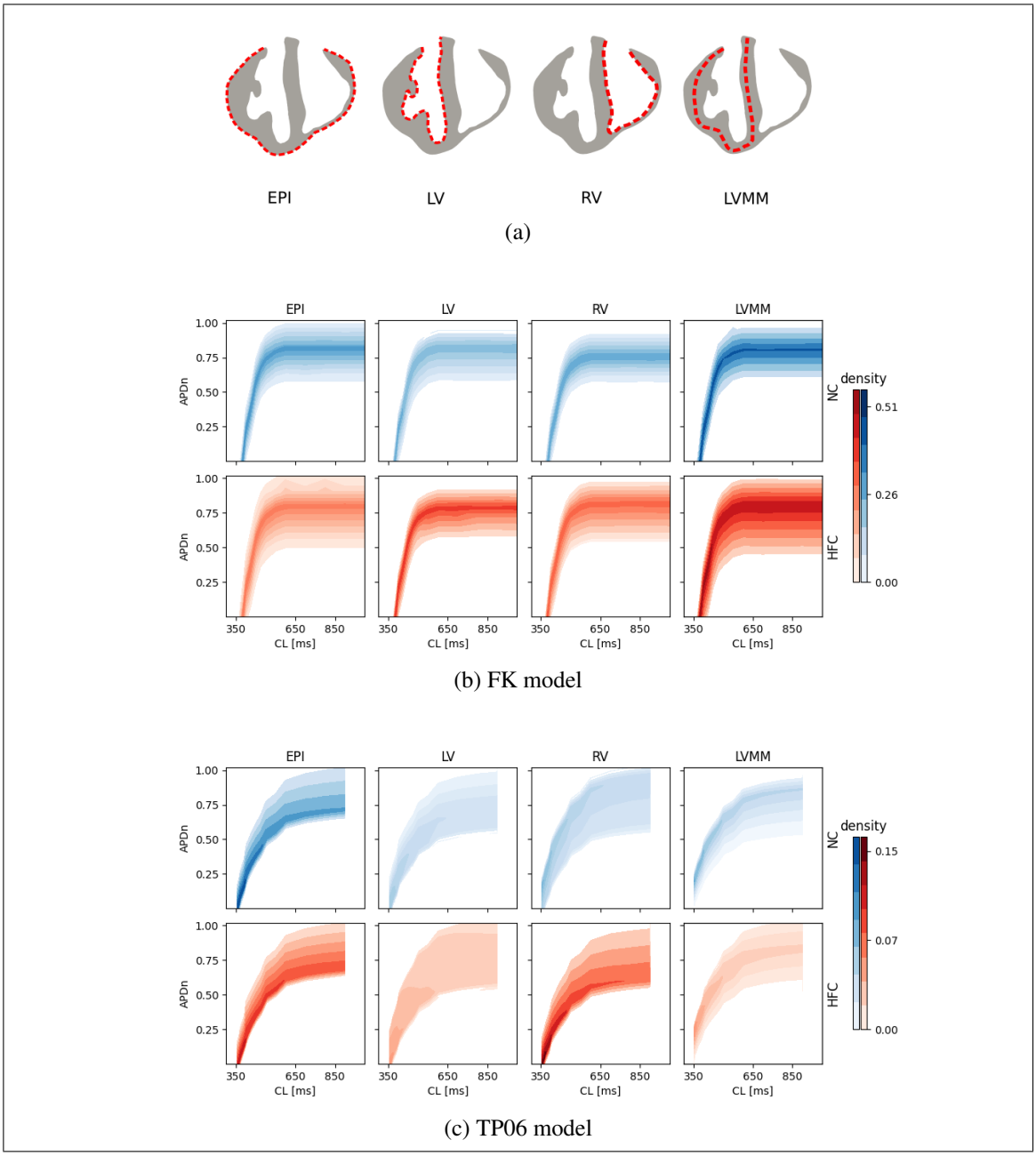

Figure 6.2. (a) Anatomical surfaces for restitution quantification: epicardium (EPI), left ventricular endocardium (LV), right ventricular endocardium (RV), left ventricular mid-myocardium (LVMM). Normalized APD restitution distribution (APD_n) for (b) FK and (c) TP06 model comparing healthy (NC–red) and myocardiacl infarcted (HFC–blue) hearts.

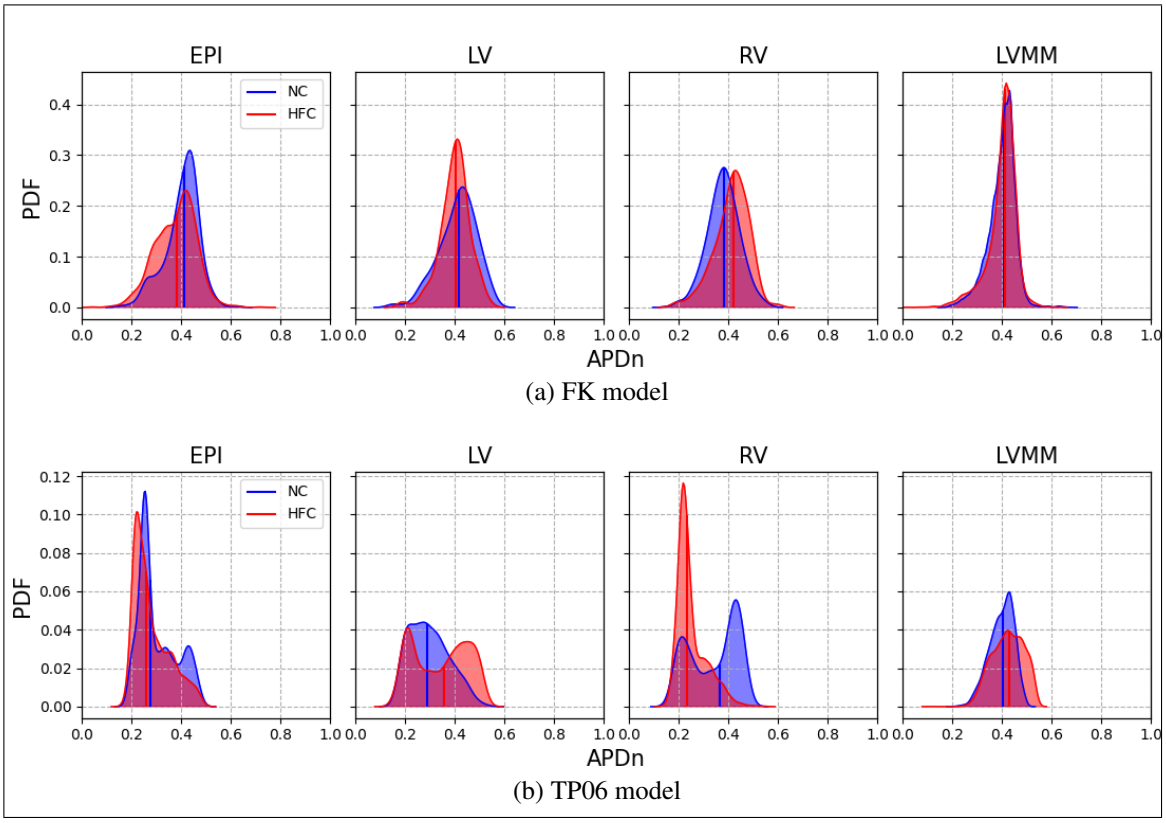

Figure 6.3. Normalized probability distribution function of normalized action potential duration at CL $= 400$ ms for (a) FK and (b) TP06 model, respectively. Blue and red traces refer to healthy (NC) and myocardyal infarction (HFC) cases, respectively. Mean values are depicted with solid vertical lines.

the Mann-Whitney-Wilcoxon test among the corresponding distributions of the number of filaments indicated equal probability for the HFC case ($p = 0.41$). For the NC case, the same result is not obtained.

Finally, the quantification of pseudo-ECG is shown in Fig. 6.6 providing the time course of the computed signal for both models in healthy 6.6a and diseased 6.6b heart geometries. The resulting fundamental frequencies was about 12 Hz for FK and 5 Hz for TP06 independently on the anatomical model considered.

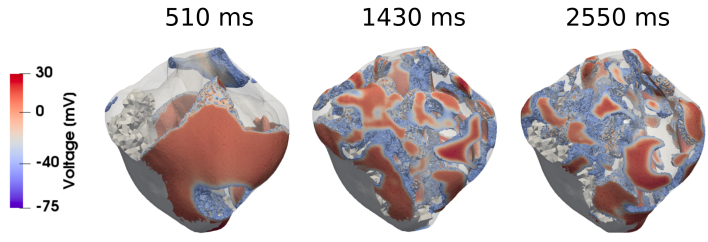

(a) FK model - HFC geometry

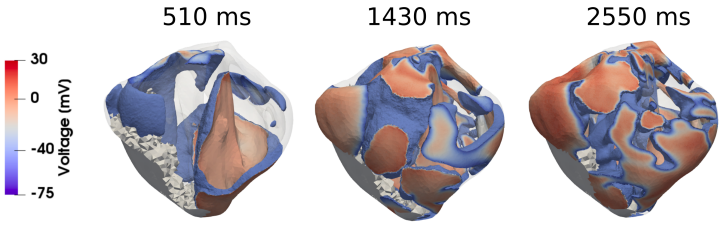

(b) TP06 model - HFC geometry

Figure 6.4. Ventricular fibrillation evolution for (a) FK and (b) TP06 ionic model within the HFC heart induced via an S1-S2 protocol. Active regions ($V_m > -75$ mV) are shown with color bar while IZ is depicted in light gray. Three times are selected showing the increase of scroll waves in accordance with the number of filaments shown in Fig. 6.5.

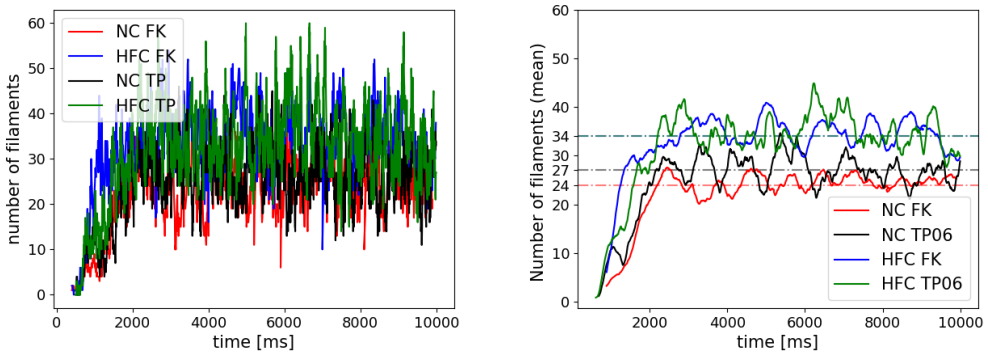

(a) (b)

Figure 6.5. (a) Number of filaments and (b) rolling mean for the FK and TP06 model during 10 s of sustained VF. Mean values are depicted with dashed lines in panel (b) after 2.5 s.

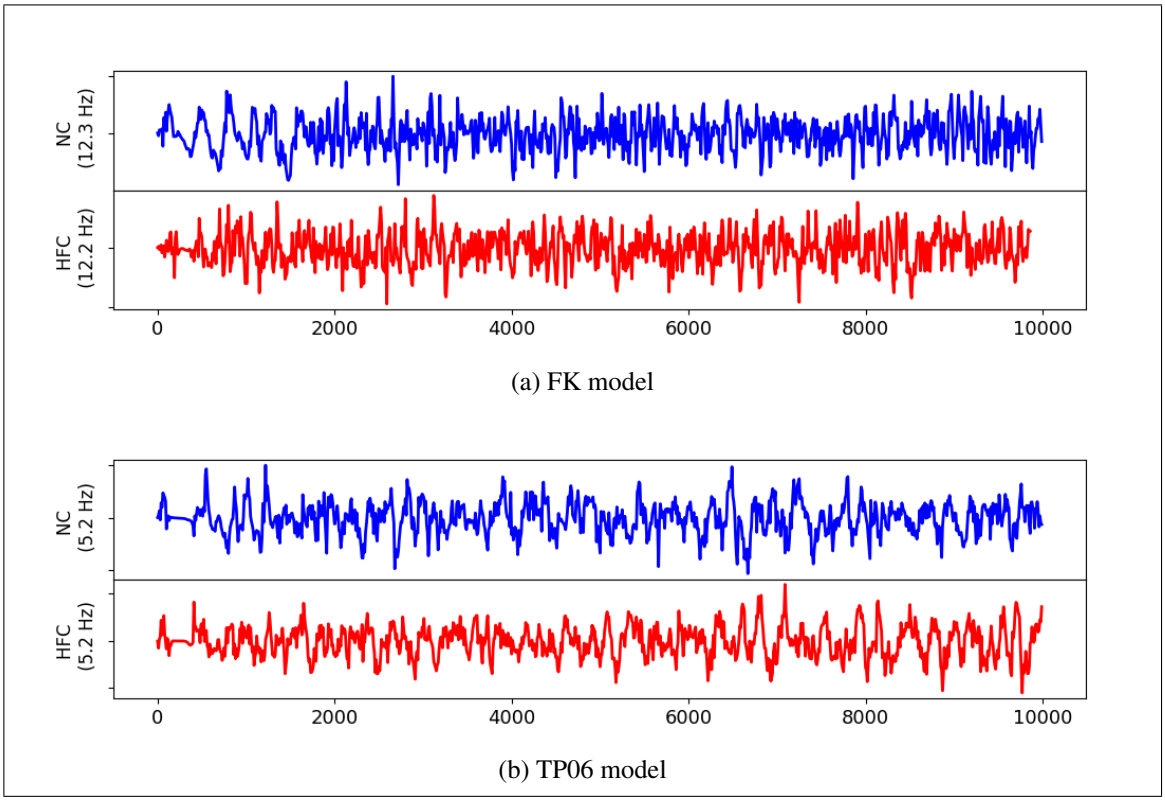

(a) FK model

(b) TP06 model

Figure 6.6. Pseudo-ECG computation for the (a) FK model and (b) the TP06 model. The fundamental frequency is also shown for each case studied.

	NC			**HFC**		
	mean	**max**	**min**	**mean**	**max**	**min**
FK	24 ± 5	40	6	34 ± 7	54	10
TP06	27 ± 6	46	11	34 ± 8	60	14

Table 6.5. Number of filaments: mean, maximum and minimum values after 2.5 s from arrhythmias induction. Comparison among ionic (FK and TP06) and geometry (NC, HFC) models.

6.3. Discussion

In this work, we have studied how the choice of ionic models impact the repolarization properties and VF signatures of computational models of normal and failing hearts.

Numerical analyses allowed us to build up probability distribution functions of APD restitution curves for four selected anatomical surfaces. Accordingly, we identified left and right ventricular endocardium as the anatomical regions characterized by a higher degree of dispersion of repolarization (multimodal PDFs) for the myocardial infarction case. On the other hand, strong electrotonic effects within the mid-myocardial layer homogenize the resulting electrical behavior, thus providing coherent PDFs among the two ionic models for healthy and diseased cases though non-negligible differences appear for epicardium, left and right endocardium.

This result, consistent with the literature and specific kinetics described by the TP06 ionic model, was further confirmed by long-run simulations conducted for ventricular fibrillation. The statistical examination of the evolution and the number of vortex filaments provided an enhanced arrhythmogenicity in the diseased case. Though constitutive differences among the two electrophysiological models appear in terms of restitution dynamics at large cycle lengths and vulnerable windows, negligible discrepancies were found for ventricular fibrillation signature. Specifically, irrespective of the healthy or pathological geometry model, the fundamental frequency of the pseudo-ECG during sustained VF is constant. Moreover, the number of filaments in the HFC case results statistically equal among FK and TP06 models.

Accordingly, our results suggest that VF signatures are mainly controlled by anatomical and structural features rather than regional restitution properties. Therefore, given the large-scale computational models and clinical translation, the choice of a simplified phenomenological description seems favorable. From a computational point of view, phenomenological models allows the implementation of highly efficient and simple integration schemes while biophysical-based model, such as the TP06, requires the employment of specialized and adequate time integration schemes that demand a complex implementation. Several works have tackled the development of time-integration strategies to cope with the stiff nature of these models (Maclachlan, Sundnes, & Spiteri, 2007; Pathmanathan et al., 2011).

The current work can be extended in several directions. First, phenomenological versus biophysical computational analyses should also consider the bidomain theoretical framework to emphasize the role of structural material heterogeneities (Potse, Dube, Richer, Vinet, & Gulrajani, 2006). On the same line, comparing linear, nonlinear, and fractional diffusion formulations will significantly help to identify the best computational approach to apply in subject-specific cardiac studies (Bueno-Orovio, Kay, Grau, Rodriguez, & Burrage, 2014; D. Hurtado et al., 2016; Weinberg, 2017). Moreover, the characterization of the border zone of the scar and gray zones in the infarcted myocardium is related to small-scale components (Ramírez, Gizzi, Sack, Guccione, & Hurtado, 2020). Such features are accurately modeled by detailed biophysical constitutive models reproducing modified ion channel dynamics (electrical remodeling). Though, reduced-order models have been shown to provide a viable alternative also in this context (Ariful Islam et al., 2015). This is key in clinical-related applications such as drug delivery, stem cell delivery, and other innovative applications where the pathology's characterization and treatment depend on the cell membrane's electrochemical dynamics and the associated local heterogeneities.

7. CONCLUSIONS

In this thesis, we developed a robust and computationally-efficient framework that allows the study of high-resolution subject-specific MRI and DT-MRI geometric and structural data. Within this framework, we could adequately estimate the regional distribution of the APD restitution curve and the number of filaments formed during VF for different characteristics of the myocardium. This provided a scheme to compare the electrical behavior of healthy and diseased hearts in different stimulation protocols. Using this scheme, we develop two main studies using data from normal and infarcted hearts. First of all, we could evaluate the influence of biomaterial injection treatments in the restitution properties of the heart and VF sustainability. Secondly, using subject-specific data in normal and pathological electrical propagation contexts, we could establish the limitations and advantages of a phenomenological cell model compared with a biophysically-based model.

The impact of biomaterial injections could be measured in normal, infarcted, and treated hearts during normal and abnormal pacing protocols. As shown in chapter 5, although the influence of biomaterial injections in the restitutive properties of treated hearts is negligible, they may be of importance in the dynamics of abnormal electrical formation, specifically in the sustainability of VF. A meaningful finding of this investigation is that the restitution properties may be primarily influenced by the distribution of the gray zone and infarcted zone. Since the biomaterial volume is not substantial, it does not have a relevant influence on these properties. Although this work is limited by the number of subjects per case, it constitutes the first computational approach to investigate the electrical effects of biomaterial injection therapies. This work opens the possibility of using *in-silico* approaches to asses the electrical attributes of alternative therapies for diseased hearts.

In chapter 6 we showed that a simplified phenomenological ionic model might be reliable in identifying critical characteristics of VF in healthy and myocardial infarction cases. Given the lower computational costs associated with simplified phenomenological

models and the easy scalability of these models to whole-heart simulations, they appear to be the right choice for the study of ventricular fibrillation in hearts in healthy or pathological conditions. However, richer information is obtained through a detailed biophysical model when we want to characterize statistical features of restitution properties and associated dispersion of repolarization behavior. Therefore, future studies in large-scale cardiac models require a careful a priori evaluation of the most convenient modeling choice for the specific problem at hand.

There are several limitations in this work. First, phenomenological versus biophysical computational analyses should also consider the bidomain theoretical framework to emphasize the role of structural material heterogeneities. Moreover, comparing different formulations, such as fractional diffusion formulations, will greatly help to identify the best computational approach to apply in subject-specific cardiac studies. Besides, the characterization of the border zone of the scar and gray zones in the infarcted myocardium is related to small-scale components. Such features may only be accurately modeled by highly detailed biophysical constitutive models reproducing modified ion channel dynamics due to electrical remodeling.

We conclude from these investigations that there is a high capability of *in silico* approaches for the study of subject-specific problems in electrophysiology. Future prospective investigations on biomaterial injection therapies include the impact of the electromechanical feedback and the use of a more complete model, such as the bidomain model, to study the significance of the extracellular potential in this problem. Besides, an exhaustive characterization of the electrical properties of biomaterial injections is necessary to make progress in the numerical modeling of these set of therapies. Finally, a comprehensive description of the border zone electrical features is not yet complete, limiting our knowledge to select an adequate modeling approach. Future investigations may be focused on identifying better the border and gray zone properties to make a suitable choice to simulate ischemic heart disease.

REFERENCES

Abbasi, M., & Clayton, R. (2013). A comparison of two models of human ventricular tissue: Simulated ischaemia and re-entry. *Computing in Cardiology 2013*, 385–388.

Allessie, M. A., Bonke, F. I., & Schopman, F. J. (1976). Circus movement in rabbit atrial muscle as a mechanism of tachycardia. ii. the role of nonuniform recovery of excitability in the occurrence of unidirectional block, as studied with multiple microelectrodes. *Circulation Research*, *39*(2), 168-177. doi: 10.1161/01.RES.39.2.168

Alonso, S., Bar, M., & Echebarria, B. (2016). Nonlinear physics of electrical wave propagation in the heart: A review. *Reports on Progress in Physics*, *79*(9), 96601. doi: 10.1088/0034-4885/79/9/096601

Arevalo, H., Plank, G., Helm, P., Halperin, H., & Trayanova, N. (2013). Tachycardia in post-infarction hearts: Insights from 3d image-based ventricular models. *PLOS ONE*, *8*(7), 1-10. doi: 10.1371/journal.pone.0068872

Arevalo, H. J., Vadakkumpadan, F., Guallar, E., Jebb, A., Malamas, P., Wu, K. C., & Trayanova, N. A. (2016). Arrhythmia risk stratification of patients after myocardial infarction using personalized heart models. *Nature Communications*, *7*(May). doi: 10.1038/ncomms11437

Ariful Islam, M., Murthy, A., Bartocci, E., Cherry, E. M., Fenton, F. H., Glimm, J., ... Grosu, R. (2015). Model-order reduction of ion channel dynamics using approximate bisimulation. *Theoretical Computer Science*, *599*, 34 - 46. (Advances in Computational Methods in Systems Biology) doi: https://doi.org/10.1016/j.tcs.2014.03.018

Attili, A. K., Schuster, A., Nagel, E., Reiber, J. H., & Van Der Geest, R. J. (2010). Quantification in cardiac MRI: Advances in image acquisition and processing. *International Journal of Cardiovascular Imaging*, *26*(SUPPL. 1), 27–40. doi: 10.1007/s10554-009-9571-x

Azevedo, P. S., Polegato, B. F., Minicucci, M. F., Paiva, S. A., & Zornoff, L. A. (2016).

Cardiac remodeling: concepts, clinical impact, pathophysiological mechanisms and pharmacologic treatment. *Arquivos brasileiros de cardiologia*, *106*(1), 62–69.

Backhaus, M., Britten, R., Do Chung, J., Cowan, B. R., Fonseca, C. G., Medrano-Gracia, P., ... Young, A. A. (2010). The cardiac atlas project: Development of a framework integrating cardiac images and models. In O. Camara, M. Pop, K. Rhode, M. Sermesant, N. Smith, & A. Young (Eds.), *Statistical atlases and computational models of the heart* (pp. 54–64). Berlin, Heidelberg: Springer Berlin Heidelberg.

Baillargeon, B., Rebelo, N., Fox, D. D., Taylor, R. L., & Kuhl, E. (2014). The living heart project: A robust and integrative simulator for human heart function. *European journal of mechanics. A, Solids*, *48*, 38-47. doi: 10.1016/j.euromechsol.2014.04.001

Barone, A., Fenton, F. H., & Veneziani, A. (2017). Numerical sensitivity analysis of a variational data assimilation procedure for cardiac conductivities. *Chaos*, *27*, 093930.

Barone, A., Gizzi, A., Fenton, F., Filippi, S., & Veneziani, A. (2020). Experimental validation of a variational data assimilation procedure for estimating space-dependent cardiac conductivities. *Computer Methods in Applied Mechanics and Engineering*, *358*, 112615. doi: https://doi.org/10.1016/j.cma.2019.112615

Beeler, G. W., & Reuter, H. (1977). Reconstruction of the action potential of ventricular myocardial fibres. *The Journal of physiology*, *268*(1), 177-210. doi: 10.1113/jphysiol.1977.sp011853

Benjamin, E. J., Muntner, P., Alonso, A., Bittencourt, M. S., Callaway, C. W., Carson, A. P., ... Virani, S. S. (2019). Heart disease and stroke statistics 2019 update: A report from the american heart association. *Circulation*, *139*(10), e56-e528. doi: 10.1161/CIR.0000000000000659

Benson, A. P., Ries, M. E., & Holden, A. V. (2007). Effects of Geometry and Architecture on Re-entrant Scroll Wave Dynamics in Human Virtual Ventricular Tissues. *Functional Imaging and Modeling of the Heart*, 200–209. doi: 10.1007/978-3-540-72907-5_21

Bosch, R. F., Zeng, X., Grammer, J. B., Popovic, K., Mewis, C., & Kühlkamp, V. (1999).

Ionic mechanisms of electrical remodeling in human atrial fibrillation. *Cardiovascular Research*, *44*(1), 121–131. doi: 10.1016/S0008-6363(99)00178-9

Bristow, M. R., Saxon, L. A., Boehmer, J., Krueger, S., Kass, D. A., De Marco, T., ... Feldman, A. M. (2004). Cardiac-Resynchronization Therapy with or without an Implantable Defibrillator in Advanced Chronic Heart Failure. *New England Journal of Medicine*, *350*(21), 2140–2150+2227. doi: 10.1056/NEJMoa032423

Buckberg, G., Athanasuleas, C., & Conte, J. (2012). Surgical ventricular restoration for the treatment of heart failure. *Nature Reviews Cardiology*, *9*(12), 703–716. doi: 10.1038/nrcardio.2012.143

Bueno-Orovio, A., Cherry, E. M., & Fenton, F. H. (2008). Minimal model for human ventricular action potentials in tissue. *Journal of Theoretical Biology*, *253*(3), 544–560. doi: 10.1016/j.jtbi.2008.03.029

Bueno-Orovio, A., Kay, D., Grau, V., Rodriguez, B., & Burrage, K. (2014). Fractional diffusion models of cardiac electrical propagation: role of structural heterogeneity in dispersion of repolarization. *Journal of the Royal Society Interface*, *11*, 20140352.

Castelvecchio, S., & Menicanti, L. (2013). *Left ventricular reconstruction: update to left ventricular aneurysm and reshaping techniques.* Retrieved from `https://mmcts.org/tutorial/27#additionalInfo`

Chandrasekhar, J., Gill, A., & Mehran, R. (2018). Acute myocardial infarction in young women: current perspectives. *International journal of women's health*, *10*, 267-284. doi: 10.2147/IJWH.S107371

Chang, A., Cadaret, L. M., & Liu, K. (2020, 10). Machine learning in electrocardiography and echocardiography: Technological advances in clinical cardiology. *Current Cardiology Reports*, *22*(12), 161. doi: 10.1007/s11886-020-01416-9

Chang, S., Chang, H., Choi, S., Chun, E., Yoon, Y., Kim, H., ... Lardo, A. (2009). Usefulness of left ventricular dyssynchrony after acute myocardial infarction, assessed by a tagging magnetic resonance image derived metric, as a determinant of ventricular remodeling. *American Journal of Cardiology*, *104*(1), 19–23. doi: 10.1016/j.amjcard.2009.02.042

Cherry, E. M., & Fenton, F. H. (2004). Suppression of alternans and conduction blocks despite steep apd restitution: electrotonic, memory, and conduction velocity restitution effects. *American Journal of Physiology-Heart and Circulatory Physiology*, *286*, H2332-H2341. doi: https://doi.org/10.1152/ajpheart.00747.2003

Cherry, E. M., & Fenton, F. H. (2008). Visualization of spiral and scroll waves in simulated and experimental cardiac tissue. *New Journal of Physics*, *10*, 125016.

Cherubini, C., Filippi, S., Gizzi, A., & Ruiz-Baier, R. (2017). A note on stress-driven anisotropic diffusion and its role in active deformable media. *Journal of Theoretical Biology*, *430*, 221 - 228. doi: https://doi.org/10.1016/j.jtbi.2017.07.013.

Choy, J. S., Leng, S., Acevedo-Bolton, G., Shaul, S., Fu, L., Guo, X., ... Kassab, G. S. (2018). Efficacy of intramyocardial injection of algisyl-lvr for the treatment of ischemic heart failure in swine. *International journal of cardiology*, *255*, 129-135. doi: 10.1016/j.ijcard.2017.09.179

Christoph, J., Chebbok, M., Richter, C., Schröder-Schetelig, J., Bittihn, P., Stein, S., ... Luther, S. (2018). Electromechanical vortex filaments during cardiac fibrillation. *Nature*, *555*.

Clayton, R. H., Bernus, O., Cherry, E. M., Dierckx, H., Fenton, F. H., Mirabella, L., ... Zhang, H. (2011). Models of cardiac tissue electrophysiology: Progress, challenges and open questions. *Progress in Biophysics and Molecular Biology*, *104*(1-3), 22–48. doi: 10.1016/j.pbiomolbio.2010.05.008

Clayton, R. H., & Holden, A. V. (2004). Filament Behavior in a Computational Model of Ventricular Fibrillation in the Canine Heart. *IEEE Transactions on Biomedical Engineering*, *51*(1), 28–34. doi: 10.1109/TBME.2003.820356

Clayton, R. H., & Taggart, P. (2005). Regional differences in apd restitution can initiate wavebreak and re-entry in cardiac tissue: A computational study. *BioMedical Engineering OnLine*, *4*(1), 54. doi: 10.1186/1475-925X-4-54

Clayton, R. H., Zhuchkova, E. A., & Panfilov, A. V. (2006). Phase singularities and filaments: Simplifying complexity in computational models of ventricular fibrillation. *Progress in Biophysics and Molecular Biology*, *90*(1-3), 378–398. doi:

10.1016/j.pbiomolbio.2005.06.011

Cokkinos, D. V., & Belogianneas, C. (2016). Left ventricular remodelling: A problem in search of solutions. *European cardiology*, *11*(1), 29-35.

Corrias, A., Jie, X., Romero, L., Bishop, M., Bernabeu, M., Pueyo, E., & Rodriguez, B. (2010). Arrhythmic risk biomarkers for the assessment of drug cardiotoxicity: From experiments to computer simulations. *Philosophical transactions. Series A, Mathematical, physical, and engineering sciences*, *368*, 3001-25. doi: 10.1098/rsta.2010.0083

Costa, C. M., & Dos Santos, R. W. (2010). Limitations of the homogenized cardiac Monodomain model for the case of low gap junctional coupling. *2010 Annual International Conference of the IEEE Engineering in Medicine and Biology Society, EMBC'10*, 228–231. doi: 10.1109/IEMBS.2010.5627817

Costabal, F. S., Concha, F. A., E.Hurtado, D., & Kuhl, E. (2017). The importance of mechano-electrical feedback and inertia in cardiac electromechanics. *Computer methods in applied mechanics and engineering*, *320*, 352 - 368. doi: https://doi.org/10.1016/j.cma.2017.03.015

Courtemanche, M., Ramirez, R. J., & Nattel, S. (1998). Ionic mechanisms underlying human atrial action potential properties: Insights from a mathematical model. *American Journal of Physiology - Heart and Circulatory Physiology*, *275*(1 44-1). doi: 10.1152/ajpheart.1998.275.1.h301

Crespo-Leiro, M. G., Metra, M., Lund, L. H., Milicic, D., Costanzo, M. R., Filippatos, G., ... Ruschitzka, F. (2018). Advanced heart failure: a position statement of the Heart Failure Association of the European Society of Cardiology. *European Journal of Heart Failure*, *20*(11), 1505–1535. doi: 10.1002/ejhf.1236

Cusimano, N., Gizzi, A., Fenton, F., Filippi, S., & Gerardo-Giorda, L. (2020). Key aspects for effective mathematical modelling of fractional-diffusion in cardiac electrophysiology: A quantitative study. *Communications in Nonlinear Science and Numerical Simulation*, *84*, 105152. doi: https://doi.org/10.1016/j.cnsns.2019.105152

Davidenko, J. M., Pertsov, A. V., Salomonsz, R., Baxter, W., & Jalife, J. (1992). Stationary

and drifting spiral waves of excitation in isolated cardiac muscle. *Nature*, *355*(6358), 349-351. doi: 10.1038/355349a0

Deng, D., Jiao, P., Ye, X., & Xia, L. (2012). An image-based model of the whole human heart with detailed anatomical structure and fiber orientation. *Computational and Mathematical Methods in Medicine*, *2012*. doi: 10.1155/2012/891070

Deng, D., Prakosa, A., Shade, J., Nikolov, P., & Trayanova, N. A. (2019). Sensitivity of ablation targets prediction to electrophysiological parameter variability in image-based computational models of ventricular tachycardia in post-infarction patients. *Frontiers in Physiology*, *10*, 628. doi: 10.3389/fphys.2019.00628

Dhein, S., Seidel, T., Salameh, A., Jozwiak, J., Hagen, A., Kostelka, M., ... Mohr, F. W. (2014). Remodeling of cardiac passive electrical properties and susceptibility to ventricular and atrial arrhythmias. *Frontiers in Physiology*, *5*(OCT), 1–13. doi: 10.3389/fphys.2014.00424

Dierckx, H., Fenton, F. H., Filippi, S., Pumir, A., & Sridhar, S. (2019). Editorial: Simulating normal and arrhythmic dynamics: From sub-cellular to tissue and organ level. *Frontiers in Physics*, *7*, 89. doi: 10.3389/fphy.2019.00089

Dolgin, M., of the New York Heart Association, C. C., Committee, N. Y. H. A. C., Fox, A., & Levin, R. (1994). *Nomenclature and criteria for diagnosis of diseases of the heart and great vessels*. Little, Brown.

Dupraz, M., Filippi, S., Gizzi, A., Quarteroni, A., & Ruiz-Baier, R. (2015). Finite element and finite volume-element simulation of pseudo-ECGs and cardiac alternans. *Mathematical Methods in the Applied Sciences*, *38*(6), 1046–1058. doi: 10.1002/mma.3127

Ester, M., Kriegel, H.-P., Sander, J., & Xu, X. (1996). A density-based algorithm for discovering clusters in large spatial databases with noise. In *Proceedings of the second international conference on knowledge discovery and data mining* (pp. 226–231). AAAI Press.

Fenton, F., & Karma, A. (1998). Vortex dynamics in three-dimensional continuous myocardium with fiber rotation: Filament instability and fibrillation. *Chaos: An Interdisciplinary Journal of Nonlinear Science*, *8*(1), 20-47. doi: 10.1063/1.166311

Fenton, F., Luther, S., Cherry, E., Otani, N., Krinsky, V., Pumir, A., ... Gilmour, R. J. (2009). Termination of atrial fibrillation using pulsed low-energy far-field stimulation. *Circulation*, *120*, 467–76. doi: 10.1161/CIRCULATIONAHA.108.825091

Fenton, F. H., & Cherry, E. M. (2002). Multiple mechanisms of spiral wave breakup in a model of cardiac electrical activity. *Chaos*, *12*, 852–892. doi: https://doi.org/10.1063/1.1504242

Fenton, F. H., & Cherry, E. M. (2008). Models of cardiac cell. *Scholarpedia*, *3*, 1868.

Fenton, F. H., Cherry, E. M., Hastings, H. M., & Evans, S. J. (2002). Multiple mechanisms of spiral wave breakup in a model of cardiac electrical activity. *Chaos*, *12*, 852–892.

Fenton, F. H., Gizzi, A., Cherubini, C., Pomella, N., & Filippi, S. (2013). Role of temperature on nonlinear cardiac dynamics. *Physical Review E*, *87*, 042709.

Fenton, F. H., & Karma, A. (1998). Fiber-rotation-induced vortex turbulence in thick myocardium. *Physical Review Letters*, *81*, 481. doi: https://doi.org/10.1103/PhysRevLett.81.481

Ferrero, J. M., Trenor, B., & Romero, L. (2014). Multiscale computational analysis of the bioelectric consequences of myocardial ischaemia and infarction. *Europace*, *16*(3), 405–415. doi: 10.1093/europace/eut405

FitzHugh, R. (1961). Impulses and physiological states in theoretical models of nerve membrane. *Biophysical Journal*, *1*(6), 445 - 466. doi: https://doi.org/10.1016/S0006-3495(61)86902-6

Fonseca, C. G., Dissanayake, A. M., Doughty, R. N., Whalley, G. A., Gamble, G. D., Cowan, B. R., ... Young, A. A. (2004, 01). Three-dimensional assessment of left ventricular systolic strain in patients with type 2 diabetes mellitus, diastolic dysfunction, and normal ejection fraction. *American Journal of Cardiology*, *94*(11), 1391-1395. doi: 10.1016/j.amjcard.2004.07.143

Franzone, P. C., Deuflhard, P., Erdmann, B., Lang, J., & Pavarino, L. F. (2006). Adaptivity

in space and time for reaction-diffusion systems in electrocardiology. *SIAM Journal on Scientific Computing*, *28*(3), 942–962. doi: 10.1137/050634785

Franzone, P. C., Pavarino, L. F., & Scacchi, S. (2014). *Mathematical cardiac electrophysiology* (Vol. 13). Springer.

Galli, A., & Lombardi, F. (2016). Postinfarct Left Ventricular Remodelling: A Prevailing Cause of Heart Failure. *Cardiology Research and Practice*, *2016*. doi: 10.1155/2016/2579832

Gizzi, A., Cherry, E., Gilmour, R., Luther, S., Filippi, S., & Fenton, F. (2013). Effects of pacing site and stimulation history on alternans dynamics and the development of complex spatiotemporal patterns in cardiac tissue. *Frontiers in Physiology*, *4*, 71. doi: 10.3389/fphys.2013.00071

Gokhale, T. A., Medvescek, E., & Henriquez, C. S. (2017). Modeling dynamics in diseased cardiac tissue: Impact of model choice. *Chaos*, *27*(9). doi: 10.1063/1.4999605

Gray, R. A., Jalife, J., Panfilov, A. V., Baxter, W. T., Cabo, C., Davidenko, J. M., & Pertsov, A. M. (1995). Mechanisms of cardiac fibrillation. *Science*, *270*, 1222–1223. doi: 10.1126/science.270.5239.1222

Gray, R. A., & Pathmanathan, P. (2018). Patient-specific cardiovascular computational modeling: Diversity of personalization and challenges. *Journal of Cardiovascular Translational Research*, *11*(2), 80–88. doi: 10.1007/s12265-018-9792-2

Göktepe, S., & Kuhl, E. (2009). Computational modeling of cardiac electrophysiology: A novel finite element approach. *International Journal for Numerical Methods in Engineering*, *79*(2), 156-178. doi: 10.1002/nme.2571

Helm, P., Beg, M. F., Miller, M. I., & Winslow, R. L. (2005). Measuring and mapping cardiac fiber and laminar architecture using diffusion tensor mr imaging. *Annals of the New York Academy of Sciences*, *1047*(1), 296-307. doi: 10.1196/annals.1341.026

Hendrikx, G., Vöö, S., Bauwens, M., Post, M. J., & Mottaghy, F. M. (2016). SPECT and PET imaging of angiogenesis and arteriogenesis in pre-clinical models of myocardial ischemia and peripheral vascular disease. *European Journal of Nuclear*

Medicine and Molecular Imaging, *43*(13), 2433–2447. doi: 10.1007/s00259-016-3480-8

Hill, Y. R., Child, N., Hanson, B., Wallman, M., Coronel, R., Plank, G., ... Bishop, M. J. (2016). Investigating a novel activation-repolarisation time metric to predict localised vulnerability to reentry using computational modelling. *PLOS ONE*, *11*, 1-22. doi: 10.1371/journal.pone.0149342

Hinderer, S., & Schenke-Layland, K. (2019). Cardiac fibrosis – a short review of causes and therapeutic strategies. *Advanced Drug Delivery Reviews*, *146*, 77 - 82. (Wound healing and fibrosis – State of play) doi: https://doi.org/10.1016/j.addr.2019.05.011

Holmes, A. A., Scollan, D., & Winslow, R. L. (2000). Direct histological validation of diffusion tensor mri in formaldehyde-fixed myocardium. *Magnetic Resonance in Medicine*, *44*(1), 157-161. doi: 10.1002/1522-2594(200007)44:1<157::AID-MRM22>3.0.CO;2-F

Holzapfel, G. A., & Ogden, R. W. (2009). Constitutive modelling of passive myocardium: A structurally based framework for material characterization. *Philosophical Transactions of the Royal Society A: Mathematical, Physical and Engineering Sciences*, *367*(1902), 3445–3475. doi: 10.1098/rsta.2009.0091

How crts work. (2017). Boston Scientific. Retrieved from `https://www.bostonscientific.com/en-US/patients/about-your-device/crt-devices/how-crts-work.html`

Hu, Y., Gurev, V., Constantino, J., Bayer, J. D., & Trayanova, N. A. (2013). Effects of mechano-electric feedback on scroll wave stability in human ventricular fibrillation. *PloS one*, *8*(4), e60287-e60287. doi: 10.1371/journal.pone.0060287

Hurtado, D., Castro, S., & Gizzi, A. (2016). Computational modeling of non-linear diffusion in cardiac electrophysiology: A novel porous-medium approach. *Computer Methods in Applied Mechanics and Engineering*, *300*, 70 - 83. doi: https://doi.org/10.1016/j.cma.2015.11.014

Hurtado, D., & Henao, D. (2014). Gradient flows and variational principles for cardiac electrophysiology: Toward efficient and robust numerical simulations of the electrical activity of the heart. *Computer Methods in Applied Mechanics and Engineering*, *273*. doi: 10.1016/j.cma.2014.02.002

Hurtado, D. E., Castro, S., & Madrid, P. (2017). Uncertainty quantification of two models of cardiac electromechanics. *International Journal for Numerical Methods in Biomedical Engineering*, *e2984*, 1–21. doi: 10.1002/cnm.2894

Hurtado, D. E., Jilberto, J., & Panasenko, G. (2020). Non-ohmic tissue conduction in cardiac electrophysiology: upscaling the non-linear voltage-dependent conductance of gap junctions. *PLoS Computational Biology*, *16*(2), e1007232.

Jalife, J. (2000). Ventricular fibrillation: Mechanisms of initiation and maintenance. *Annual Review of Physiology*, *62*(1), 25-50. (PMID: 10845083) doi: 10.1146/annurev.physiol.62.1.25

Kaboudian, A., Cherry, E. M., & Fenton, F. H. (2019). Real-time interactive simulations of large-scale systems on personal computers and cell phones: Toward patient-specific heart modeling and other applications. *Science Advances*, *5*(3). doi: 10.1126/sciadv.aav6019

Kariya, T., Washio, T., Okada, J.-i., Nakagawa, M., Watanabe, M., Kadooka, Y., … Hisada, T. (2020). Personalized perioperative multi-scale, multi-physics heart simulation of double outlet right ventricle. *Annals of Biomedical Engineering*, *48*(6), 1740–1750. doi: 10.1007/s10439-020-02488-y

Karma, A. (1994). Electrical alternans and spiral wave breakup in cardiac tissue. *Chaos: An Interdisciplinary Journal of Nonlinear Science*, *4*(3), 461-472. doi: 10.1063/1.166024

Karma, A. (2011). Physics of Cardiac Arrhythmogenesis. *Annual Review of Condensed Matter Physics*, *4*(1), 313–337. doi: 10.1146/annurev-conmatphys-020911-125112

Katz, A. M. (2008). The ”modern” view of heart failure: how did we get here? *Circulation. Heart failure*, *1*(1), 63–71. doi: 10.1161/CIRCHEARTFAILURE.108.772756

Keener, J., & Sneyd, J. (2009). *Mathematical physiology 1: Cellular physiology* (Vol. 2). Springer.

Kim, R. J., Wu, E., Rafael, A., Chen, E.-L., Parker, M. A., Simonetti, O., ... Judd, R. M. (2000). The use of contrast-enhanced magnetic resonance imaging to identify reversible myocardial dysfunction. *New England Journal of Medicine*, *343*(20), 1445-1453. (PMID: 11078769) doi: 10.1056/NEJM200011163432003

Koitabashi, N., & Kass, D. A. (2012). Reverse remodeling in heart failure-mechanisms and therapeutic opportunities. *Nature Reviews Cardiology*, *9*(3), 147–157. doi: 10.1038/nrcardio.2011.172

Koller, M. L., Maier, S. K., Gelzer, A. R., Bauer, W. R., Meesmann, M., & Gilmour, R. F. (2005). Altered dynamics of action potential restitution and alternans in humans with structural heart disease. *Circulation*, *112*(11), 1542-1548. doi: 10.1161/CIRCULATIONAHA.104.502831

Konstam, M. A., Kramer, D. G., Patel, A. R., Maron, M. S., & Udelson, J. E. (2011). Left ventricular remodeling in heart failure: Current concepts in clinical significance and assessment. *JACC: Cardiovascular Imaging*, *4*(1), 98–108. doi: 10.1016/j.jcmg.2010.10.008

Land, S., & et al. (2015). Verification of cardiac mechanics software: benchmark problems and solutions for testing active and passive material behaviour. *Proc. R. Soc. A*, *471*, 20150641. doi: https://doi.org/10.1098/rspa.2015.0641

Larson, C., Dragnev, L., & Trayanova, N. (2003). Analysis of electrically induced reentrant circuits in a sheet of myocardium. *Annals of Biomedical Engineering*, *31*(7), 768-780. doi: 10.1114/1.1581289

Lee, R. J., Hinson, A., Bauernschmitt, R., Matschke, K., Fang, Q., Mann, D. L., ... Sabbah, H. N. (2015). The feasibility and safety of algisyl-lvr^{TM} as a method of left ventricular augmentation in patients with dilated cardiomyopathy: Initial first in man clinical results. *International Journal of Cardiology*, *199*, 18 - 24. doi: https://doi.org/10.1016/j.ijcard.2015.06.111

Lenarda, P., Gizzi, A., & Paggi, M. (2018). A modeling framework for electro-mechanical interaction between excitable deformable cells. *European Journal of Mechanics - A/Solids*, *72*, 374 - 392. doi: https://doi.org/10.1016/j.euromechsol.2018.06.001

LeVeque, R. J., & Leveque, R. J. (1992). *Numerical methods for conservation laws* (Vol. 132). Springer.

Loppini, A., Gizzi, A., Cherubini, C., Cherry, E. M., Fenton, F. H., & Filippi, S. (2019). Spatiotemporal correlation uncovers characteristic lengths in cardiac tissue. *Phys. Rev. E*, *100*, 020201. doi: 10.1103/PhysRevE.100.020201

Loppini, A., Gizzi, A., Ruiz-Baier, R., Cherubini, C., Fenton, F. H., & Filippi, S. (2018). Competing mechanisms of stress-assisted diffusivity and stretch-activated currents in cardiac electromechanics. *Frontiers Physiology*, *9*, 1714. doi: 10.3389/fphys.2018.01714

Lüderitz, B. (2009). Historical perspectives of cardiac electrophysiology. *Hellenic Journal of Cardiology*, *50*(1), 3–16.

Luo, C. H., & Rudy, Y. (1991). A model of the ventricular cardiac action potential. depolarization, repolarization, and their interaction. *Circulation Research*, *68*(6), 1501-1526. doi: 10.1161/01.RES.68.6.1501

Luo, C. H., & Rudy, Y. (1994). A Dynamic Model of the Cardiac Ventricular Action Potential. *Circulation Research*, *74*(6), 1071–1096.

Luther, S., Fenton, F. H., Kornreich, B. G., Squires, A., Bittihn, P., Hornung, D., ... Bodenschatz, E. (2011). Low-energy control of electrical turbulence in the heart. *Nature*, *475*(7355), 235-239. doi: 10.1038/nature10216

Maclachlan, M. C., Sundnes, J., & Spiteri, R. J. (2007). A comparison of non-standard solvers for ODEs describing cellular reactions in the heart. *Computer Methods in Biomechanics and Biomedical Engineering*, *10*(5), 317–326. doi: 10.1080/10255840701259301

Mancini, D., & Burkhoff, D. (2005). Mechanical device-based methods of managing and treating heart failure. *Circulation*, *112*(3), 438–448. doi: 10.1161/CIRCULATION-AHA.104.481259

Mant, J., Al-Mohammad, A., Davis, M., Dawda, P., Gilmour, J., Hardman, S., ... Price, A. (2010). *Chronic heart failure: National clinical guideline for diagnosis management in primary and secondary care: Partial update*. Royal College of Physicians (UK).

Maqsood, M. H., & Rubab, K. (2019). The role of the cardioversion defibrillator in post myocardial infarction sudden cardiac death: A systematic review of clinical trials and observational studies. *Cureus*, *11*(3).

Mendonca Costa, C., Plank, G., Rinaldi, C. A., Niederer, S. A., & Bishop, M. J. (2018). Modeling the electrophysiological properties of the infarct border zone. *Frontiers in Physiology*, *9*, 356. doi: 10.3389/fphys.2018.00356

Mickleborough, L., Carson, S., & Ivanov, J. (2001). Repair of dyskinetic or akinetic left ventricular aneurysm: results obtained with a modified linear closure. *The Journal of Thoracic and Cardiovascular Surgery*, *121*(4), 675—682. doi: 10.1067/mtc.2001.112633

Mihic, A., Cui, Z., Wu, J., Vlacic, G., Miyagi, Y., Li, S.-H., ... Li, R.-K. (2015). A conductive polymer hydrogel supports cell electrical signaling and improves cardiac function after implantation into myocardial infarct. *Circulation*, *132*(8), 772-784. doi: 10.1161/CIRCULATIONAHA.114.014937

Nash, M. P., Bradley, C. P., Sutton, P. M., Clayton, R. H., Kallis, P., Hayward, M. P., ... Taggart, P. (2006). Whole heart action potential duration restitution properties in cardiac patients: A combined clinical and modelling study. *Experimental Physiology*, *91*(2), 339–354. doi: 10.1113/expphysiol.2005.031070

Niederer, S. A., Aboelkassem, Y., Cantwell, C. D., Corrado, C., Coveney, S., Cherry, E. M., ... Wang, L. (2020). Creation and application of virtual patient cohorts of heart models. *Philosophical Transactions of the Royal Society A: Mathematical, Physical and Engineering Sciences*, *378*(2173), 20190558. doi: 10.1098/rsta.2019.0558

Niederer, S. A., Lumens, J., & Trayanova, N. A. (2019). Computational models in cardiology. *Nature Reviews Cardiology*, *16*(2), 100–111. doi: 10.1038/s41569-018-0104-y

Nielsen, P., Le Grice, I., Smaill, B., & Hunter, P. (1991). Mathematical model of geometry and fibrous structure of the heart. *American Journal of Physiology-Heart and Circulatory Physiology*, *260*(4), H1365–H1378.

Noble, D. (1962). A modification of the hodgkin—huxley equations applicable to purkinje fibre action and pacemaker potentials. *The Journal of Physiology*, *160*(2), 317-352. doi: https://doi.org/10.1113/jphysiol.1962.sp006849

O'Hara, T., Virág, L., Varró, A., & Rudy, Y. (2011). Simulation of the undiseased human cardiac ventricular action potential: Model formulation and experimental validation. *PLoS Computational Biology*, *7*(5). doi: 10.1371/journal.pcbi.1002061

Okajima, M., Fujino, T., Kobayashi, T., & Yamada, K. (1968). Computer simulation of the propagation process in excitation of the ventricles. *Circulation research*, *23*(2), 203–211.

Oliver, R. A., & Krassowska, W. (2005). Reproducing cardiac restitution properties using the fenton-karma membrane model. *Annals of Biomedical Engineering*, *33*(7), 907–911. doi: 10.1007/s10439-005-3948-3

Oresko, J. J., Jin, Z., Cheng, J., Huang, S., Sun, Y., Duschl, H., & Cheng, A. C. (2010). A wearable smartphone-based platform for real-time cardiovascular disease detection via electrocardiogram processing. *IEEE Transactions on Information Technology in Biomedicine*, *14*(3), 734–740.

Panfilov, A., & Pertsov, A. (2001a). Ventricular fibrillation: Evolution of the multiple-wavelet hypothesis. *Philosophical Transactions of the Royal Society A: Mathematical, Physical and Engineering Sciences*, *359*(1783), 1315–1325. doi: 10.1098/rsta.2001.0833

Panfilov, A., & Pertsov, A. (2001b). Ventricular fibrillation: evolution of the multiple-wavelet hypothesis. *Phil. Trans. R. Soc. Lond. A*, *359*, 1315–1325. doi: 10.1098/rsta.2001.0833

Pashaei, A., Romero, D., Sebastian, R., Camara, O., & Frangi, A. F. (2010). Comparison of phenomenological and biophysical cardiac models coupled with heterogenous structures for prediction of electrical activation sequence. *Computing in Cardiology*, *37*, 871–874.

Pathmanathan, P., & Gray, R. A. (2018). Validation and trustworthiness of multiscale models of cardiac electrophysiology. *Frontiers in Physiology*, *9*(FEB), 1–19. doi: 10.3389/fphys.2018.00106

Pathmanathan, P., Mirams, G., Southern, J., & Whitheley, J. (2011). The significant effect of the choice of ionic current integration method in cardiac electrophysiological simulations. *International Journal for Numerical Methods in Biomedical Engineering*, *27*, 1751–1770.

Peirlinck, M., Sahli Costabal, F., Sack, K. L., Choy, J. S., Kassab, G. S., Guccione, J. M., ... Kuhl, E. (2019). Using machine learning to characterize heart failure across the scales. *Biomechanics and Modeling in Mechanobiology*, *18*(6), 1987–2001. doi: 10.1007/s10237-019-01190-w

Peñaranda, A., Cantalapiedra, I. R., Bragard, J., & Echebarria, B. (2012). Cardiac dynamics: A simplified model for action potential propagation. *Theoretical Biology and Medical Modelling*, *9*(1), 1–18. doi: 10.1186/1742-4682-9-50

Perotti, L. E., Krishnamoorthi, S., Borgstrom, N. P., Ennis, D. B., & Klug, W. S. (2015). Regional segmentation of ventricular models to achieve repolarization dispersion in cardiac electrophysiology modeling. *International journal for numerical methods in biomedical engineering*, *31*(8), 10.1002/cnm.2718. doi: 10.1002/cnm.2718

Plank, G., Leon, L. J., Kimber, S., & Vigmond, E. J. (2005). Defibrillation depends on conductivity fluctuations and the degree of disorganization in reentry patterns. *Journal of Cardiovascular Electrophysiology*, *16*(2), 205-216. doi: 10.1046/j.1540-8167.2005.40140.x

Plonsey, R., & Barr, R. C. (2007). *Bioelectricity: A quantitative approach* (Third Edition ed.). New York: Springer.

Potse, M., Dube, B., Richer, J., Vinet, A., & Gulrajani, R. (2006). A comparison of monodomain and bidomain reaction-diffusion models for action potential propagation in the human heart. *IEEE Transactions on Biomedical Engineering*, *53*, 2425–2435.

Propp, A., Gizzi, A., Levrero-Florencio, F., & Ruiz-Baier, R. (2020). An orthotropic electro-viscoelastic model for the heart with stress-assisted diffusion. *Biomechanics and Modeling in Mechanobiology*, *19*(2), 633–659. Retrieved from https://doi.org/10.1007/s10237-019-01237-y doi: 10.1007/s10237-019-01237-y

Quarteroni, A., Lassila, T., Rossi, S., & Ruiz-Baier, R. (2017). Integrated heart—coupling multiscale and multiphysics models for the simulation of the cardiac function. *Computer Methods in Applied Mechanics and Engineering*, *314*, 345 - 407. (Special Issue on Biological Systems Dedicated to William S. Klug) doi: https://doi.org/10.1016/j.cma.2016.05.031

Ramirez, W. A., Gizzi, A., Sack, K. L., Guccione, J. M., & Hurtado, D. E. (2020). In-silico study of the cardiac arrhythmogenic potential of biomaterial injection therapy. *Scientific Reports*, *10*(12990).

Ramírez, W. A., Gizzi, A., Sack, K. L., Guccione, J. M., & Hurtado, D. E. (2020). In-silico study of the cardiac arrhythmogenic potential of biomaterial injection therapy. *Scientific Reports*, *10*, 12990. Retrieved from https://doi.org/10.1038/s41598-020-69900-4 doi: 10.1038/s41598-020-69900-4

Roberts, B. N., Yang, P. C., Behrens, S. B., Moreno, J. D., & Clancy, C. E. (2012). Computational approaches to understand cardiac electrophysiology and arrhythmias. *American Journal of Physiology - Heart and Circulatory Physiology*, *303*(7), 766–783. doi: 10.1152/ajpheart.01081.2011

Roshanbinfar, K., Vogt, L., Greber, B., Diecke, S., Boccaccini, A. R., Scheibel, T., & Engel, F. B. (2018). Electroconductive biohybrid hydrogel for enhanced maturation and beating properties of engineered cardiac tissues. *Advanced Functional Materials*, *28*(42), 1803951. doi: 10.1002/adfm.201803951

Ruschitzka, F., Abraham, W. T., Singh, J. P., Bax, J. J., Borer, J. S., Brugada, J., ... Holzmeister, J. (2013). Cardiac-resynchronization therapy in heart failure with a

narrow QRS complex. *New England Journal of Medicine*, *369*(15), 1395–1405. doi: 10.1056/NEJMoa1306687

Ruvinov, E., & Cohen, S. (2016). Alginate biomaterial for the treatment of myocardial infarction: Progress, translational strategies, and clinical outlook. From ocean algae to patient bedside. *Advanced Drug Delivery Reviews*, *96*, 54–76. doi: 10.1016/j.addr.2015.04.021

Sabbah, H. N., Wang, M., Gupta, R. C., Rastogi, S., Ilsar, I., Sabbah, M. S., ... Lee, R. J. (2013). Augmentation of left ventricular wall thickness with alginate hydrogel implants improves left ventricular function and prevents progressive remodeling in dogs with chronic heart failure. *JACC: Heart Failure*, *1*(3), 252–258. doi: 10.1016/j.jchf.2013.02.006

Sack, K., Aliotta, E., Choy, J. S., Ennis, D. B., Davies, N., Franz, T., ... Guccione, J. M. (in press.). Intra-myocardial alginate hydrogel injection acts as a left ventricular mid-wall constraint in swine. *Acta Biomateralia*.

Sack, K. L., Aliotta, E., Choy, J. S., Ennis, D. B., Davies, N. H., Franz, T., ... Guccione, J. M. (2018). Effect of intra-myocardial Algisyl-LVR^{TM} injectates on fibre structure in porcine heart failure. *Journal of the Mechanical Behavior of Biomedical Materials*, *87*(May), 172–179. doi: 10.1016/j.jmbbm.2018.07.005

Sack, K. L., Aliotta, E., Choy, J. S., Ennis, D. B., Davies, N. H., Franz, T., ... Guccione, J. M. (2020). Intra-myocardial alginate hydrogel injection acts as a left ventricular mid-wall constraint in swine. *Acta Biomaterialia*. doi: 10.1016/j.actbio.2020.04.033

Sack, K. L., Aliotta, E., Ennis, D. B., Choy, J. S., Kassab, G. S., Guccione, J. M., & Franz, T. (2018). Construction and validation of subject-specific biventricular finite-element models of healthy and failing swine hearts from high-resolution dt-mri. *Frontiers in Physiology*, *9*, 539. doi: 10.3389/fphys.2018.00539

Sack, K. L., Davies, N. H., Guccione, J. M., & Franz, T. (2016). Personalised computational cardiology: Patient-specific modelling in cardiac mechanics and biomaterial

injection therapies for myocardial infarction. *Heart Failure Reviews*, *21*(6), 815–826. doi: 10.1007/s10741-016-9528-9

Sahli Costabal, F., Choy, J. S., Sack, K. L., Guccione, J. M., Kassab, G. S., & Kuhl, E. (2019). Multiscale characterization of heart failure. *Acta Biomaterialia*, *86*, 66–76. doi: 10.1016/j.actbio.2018.12.053

Sahli Costabal, F., Yao, J., & Kuhl, E. (2018). Predicting drug-induced arrhythmias by multiscale modeling. *International Journal for Numerical Methods in Biomedical Engineering*, *34*(5), e2964. (e2964 cnm.2964) doi: 10.1002/cnm.2964

Saito, K., Saito, M., Komatu, S., & Ohtomo, K. (2003). Real-time four-dimensional imaging of the heart with multi–detector row ct. *RadioGraphics*, *23*(1), e8-e8. doi: 10.1148/rg.e8

Savarese, G., & Lund, L. H. (2017). Global public health burden of heart failure. *Cardiac failure review*, *3*(1), 7-11.

Seemann, G. (2005). *Modeling of Electrophysiology and Tension Development in the Human Heart* (Unpublished doctoral dissertation). Universitätsverlag Karlsruhe.

Shinde, A. V., & Frangogiannis, N. G. (2014). Fibroblasts in myocardial infarction: A role in inflammation and repair. *Journal of Molecular and Cellular Cardiology*, *70*, 74–82. doi: 10.1016/j.yjmcc.2013.11.015

Stefanelli, G., Bellisario, A., Meli, M., Chiurlia, E., Barbieri, A., & Weltert, L. (2020). Outcomes after surgical ventricular restoration for ischemic cardiomyopathy. *Journal of Thoracic and Cardiovascular Surgery*. doi: 10.1016/j.jtcvs.2020.04.167

Stevens, C., Remme, E., LeGrice, I., & Hunter, P. (2003). Ventricular mechanics in diastole: material parameter sensitivity. *Journal of Biomechanics*, *36*(5), 737 - 748. (Cardiovascular Biomechanics) doi: https://doi.org/10.1016/S0021-9290(02)00452-9

Suarez, S. L., Rane, A. A., Muñoz, A., Wright, A. T., Zhang, S. X., Braden, R. L., … Christman, K. L. (2015). Intramyocardial injection of hydrogel with high interstitial spread does not impact action potential propagation. *Acta Biomaterialia*, *26*, 13 - 22. doi: https://doi.org/10.1016/j.actbio.2015.08.004

Sundnes, J., Fredrik Nielsen, B., Mardal, K.-A., Cai, X., Terje Lines, G., & Tveito, A. (2006). On the computational complexity of the bidomain and the monodomain models of electrophysiology. *Annals of biomedical engineering*, *34*, 1088-97. doi: 10.1007/s10439-006-9082-z

Sundnes, J., Lines, G., Cai, X., Nielsen, B., Mardal, K., & Tveito, A. (2007). *Computing the electrical activity in the heart*. Springer Berlin Heidelberg.

Ten Tusscher, K. H., Hren, R., & Panfilov, A. V. (2007). Organization of ventricular fibrillation in the human heart. *Circulation Research*, *100*(12). doi: 10.1161/CIRCRESAHA.107.150730

Ten Tusscher, K. H., Mourad, A., Nash, M. P., Clayton, R. H., Bradley, C. P., Paterson, D. J., ... Taggart, P. (2009). Organization of ventricular fibrillation in the human heart: Experiments and models. *Experimental Physiology*, *94*(5), 553–562. doi: 10.1113/expphysiol.2008.044065

Ten Tusscher, K. H. W. J., Hren, R., & Panfilov, A. V. (2005). Dynamics of reentrant arrhythmias in the human ventricles. *Heart Rhythm*, *2*(5), S260-S261. doi: 10.1016/j.hrthm.2005.02.818

ten Tusscher, K. H. W. J., & Panfilov, A. V. (2006). Alternans and spiral breakup in a human ventricular tissue model. *American Journal of Physiology-Heart and Circulatory Physiology*, *291*(3), H1088-H1100. (PMID: 16565318) doi: 10.1152/ajpheart.00109.2006

Trayanova, N., Plank, G., & Rodríguez, B. (2006). What have we learned from mathematical models of defibrillation and postshock arrhythmogenesis? application of bidomain simulations. *Heart Rhythm*, *3*(10), 1232 - 1235. doi: https://doi.org/10.1016/j.hrthm.2006.04.015

Trayanova, N. A. (2011). Whole-heart modeling : Applications to cardiac electrophysiology and electromechanics. *Circulation Research*, *108*(1), 113–128. doi: 10.1161/CIRCRESAHA.110.223610

Trayanova, N. A., & Chang, K. C. (2016a). How computer simulations of the human heart can improve anti-arrhythmia therapy. *The Journal of Physiology*, *594*(9), 2483-2502. doi: 10.1113/JP270532

Trayanova, N. A., & Chang, K. C. (2016b). How computer simulations of the human heart can improve anti-arrhythmia therapy. *Journal of Physiology*, *594*(9), 2483–2502. doi: 10.1113/JP270532

Tung, L. (1978). *A bi-domain model for describing ischemic myocardial d-c potentials* (Unpublished doctoral dissertation). Electrical Engineering and Computer Science.

Tusscher, K. H. T., Hren, R., & Panfilov, A. V. (2007). Organization of ventricular fibrillation in the human heart. *Circulation Research*, *100*(12), e87-e101. doi: 10.1161/CIRCRESAHA.107.150730

Viola, F., Meschini, V., & Verzicco, R. (2020). Fluid–structure-electrophysiology interaction (fsei) in the left-heart: A multi-way coupled computational model. *European Journal of Mechanics - B/Fluids*, *79*, 212 - 232. doi: https://doi.org/10.1016/j.euromechflu.2019.09.006

Völler, H., Kamke, W., Klein, H. U., Block, M., Reibis, R., Treusch, S., ... Wegscheider, o. b. o. t. P. I. r. i., Karl (2010). Clinical practice of defibrillator implantation after myocardial infarction: impact of implant time: results from the PreSCD II Registry†. *EP Europace*, *13*(4), 499-508. doi: 10.1093/europace/euq426

Wall, S. T., Walker, J. C., Healy, K. E., Ratcliffe, M. B., & Guccione, J. M. (2006). Theoretical impact of the injection of material into the myocardium. *Circulation*, *114*(24), 2627-2635. doi: 10.1161/CIRCULATIONAHA.106.657270

Walton, R. D., Martinez, M. E., Bishop, M. J., Hocini, M., Haïssaguerre, M., Plank, G., ... Vigmond, E. J. (2014). Influence of the Purkinje-muscle junction on transmural repolarization heterogeneity. *Cardiovascular Research*, *103*(4), 629–640. doi: 10.1093/cvr/cvu165

Weinberg, S. H. (2017). Ephaptic coupling rescues conduction failure in weakly coupled cardiac tissue with voltage-gated gap junctions. *Chaos*, *27*, 093908.

Weiss, J. N., Garfinkel, A., Karagueuzian, H. S., Chen, P.-S., & Qu, Z. (2010). Early afterdepolarizations and cardiac arrhythmias. *Heart Rhythm*, *7*(12), 1891 - 1899. doi: https://doi.org/10.1016/j.hrthm.2010.09.017

Wenk, J. F., Eslami, P., Zhang, Z., Xu, C., Kuhl, E., Gorman, J. H., ... Guccione, J. M. (2011). A novel method for quantifying the in-vivo mechanical effect of material injected into a myocardial infarction. *The Annals of Thoracic Surgery*, *92*(3), 935 - 941. doi: https://doi.org/10.1016/j.athoracsur.2011.04.089

Wenk, J. F., Wall, S. T., Peterson, R. C., Helgerson, S. L., Sabbah, H. N., Burger, M., ... Guccione, J. M. (2009). A method for automatically optimizing medical devices for treating heart failure: Designing polymeric injection patterns. *Journal of Biomechanical Engineering*, *131*(12), 121011-121011-7. doi: 10.1115/1.4000165

Windecker, S., Bax, J. J., Myat, A., Stone, G. W., & Marber, M. S. (2013). Future treatment strategies in ST-segment elevation myocardial infarction. *The Lancet*, *382*(9892), 644–657. doi: 10.1016/S0140-6736(13)61452-X

Winfree, A. (1989). Electrical instability in cardiac muscle: Phase singularities and rotors. *Journal of Theoretical Biology*, *138*(3), 353 - 405. doi: https://doi.org/10.1016/S0022-5193(89)80200-0

Winfree, A. (1994). Electrical turbulence in three-dimensional heart muscle. *Science*, *266*(5187), 1003–1006. doi: 10.1126/science.7973648

Winslow, R. L., Rice, J., Jafri, S., Marbán, E., & O'Rourke, B. (1999). Mechanisms of altered excitation-contraction coupling in canine tachycardia-induced heart failure, ii. *Circulation Research*, *84*(5), 571-586. doi: 10.1161/01.RES.84.5.571

Witzenburg, C. M., & Holmes, J. W. (2017). Biomechanics of myocardial ischemia and infarction. In G. A. Holzapfel & R. W. Ogden (Eds.), *Biomechanics: Trends in modeling and simulation* (pp. 233–269). Springer International Publishing. doi: 10.1007/978-3-319-41475-1_6

Yehia, A. R., Jeandupeux, D., Alonso, F., & Guevara, M. R. (1999). Hysteresis and bistability in the direct transition from 1:1 to 2:1 rhythm in periodically driven single ventricular cells. *Chaos: An Interdisciplinary Journal of Nonlinear Science*, *9*(4),

916-931. doi: 10.1063/1.166465

Young, A. A., & Frangi, A. F. (2009). Computational cardiac atlases: from patient to population and back. *Experimental Physiology*, *94*(5), 578–596.

Yu, J. K., Franceschi, W., Huang, Q., Pashakhanloo, F., Boyle, P. M., & Trayanova, N. A. (2019). A comprehensive, multiscale framework for evaluation of arrhythmias arising from cell therapy in the whole post-myocardial infarcted heart. *Scientific Reports*, *9*(1), 1–16. doi: 10.1038/s41598-019-45684-0

Zhang, S., Joseph, A. A., Voit, D., Schaetz, S., Merboldt, K.-D., Unterberg-Buchwald, C., ... Frahm, J. (2014). Real-time magnetic resonance imaging of cardiac function and flow-recent progress. *Quantitative imaging in medicine and surgery*, *4*(5), 313-329. doi: 10.3978/j.issn.2223-4292.2014.06.03

Zhang, Y., Yip, G. W., Chan, A. K. Y., Wang, M., Lam, W. W. M., Fung, J. W. H., ... Yu, C.-M. (2008). Left ventricular systolic dyssynchrony is a predictor of cardiac remodeling after myocardial infarction. *American heart journal*, *156*(6), 1124-1132. doi: 10.1016/j.ahj.2008.07.019

Zhong, L., Su, Y., Yeo, S.-Y., Tan, R.-S., Ghista, D. N., & Kassab, G. (2009). Left ventricular regional wall curvedness and wall stress in patients with ischemic dilated cardiomyopathy. *American Journal of Physiology-Heart and Circulatory Physiology*, *296*(3), H573-H584. (PMID: 19122166) doi: 10.1152/ajpheart.00525.2008

Zhou, X., Bueno-orovio, A., & Rodriguez, B. (2018). In silico evaluation of arrhythmia. *Current Opinion in Physiology*, *1*, 95–103. doi: 10.1016/j.cophys.2017.11.003

Zhukov, L., & Barr, A. H. (2003). Heart-muscle fiber reconstruction from diffusion tensor mri. In *Ieee visualization, 2003. vis 2003.* (p. 597-602).

APPENDIX

A. APPENDIX A

A.1. tenTusscher-Panfilov (2006) EP model equations

L-type Ca^{+2} current reads:

$$I_{CaL} = 4G_{CaL}f_2df_{\text{cass}}f\frac{(V-15)F^2}{RT}\frac{0.25Ca_{ss}e^{2(V-15)F/RT}-Ca_0}{e^{2(V-15)F/RT}-1}\,, \quad d_\infty = \frac{1}{1+e^{(-8-V)/7.5}}$$

$$\alpha_d = \frac{1.4}{1+e^{(-35-V)/13}}+0.25\,, \qquad \beta_d = \frac{1.4}{1+e^{(V+5)/5}}$$

$$\gamma_d = \frac{1}{1+e^{(50-V)/20}}\,, \qquad \tau_d = \alpha_d\beta_d+\gamma_d$$

$$f_\infty = \frac{1}{1+e^{(V+20)/7}} \qquad \alpha_f = 1102.5e^{-\left(\frac{V+27}{15}\right)^2}$$

$$\beta_f = \frac{200}{1+e^{(13-V)/10}}\,, \qquad \gamma_f = \frac{180}{1+e^{(V+30)/10}}+20$$

$$\tau_f = \alpha_f+\beta_f+\gamma_f\,, \qquad f_{2\infty} = \frac{0.67}{1+e^{(V+35)/7}}+0.33$$

$$\alpha_{f_2} = 600e^{-\frac{(V+25)^2}{170}}\,, \qquad \beta_{f_2} = \frac{31}{1+e^{(25-V)/10}}$$

$$\gamma_{f_2} = \frac{16}{1+e^{(V+30)/10}}\,, \qquad f_{\text{cass}\infty} = \frac{0.6}{1+\left(\frac{Ca_{\text{ss}}}{0.05}\right)^2}+0.4$$

$$\tau_{f\text{cass}} = \frac{80}{1+\left(\frac{Ca_{\text{ss}}}{0.05}\right)^2}+2$$

Slow delayed rectifier currents are:

$$I_{Ks} = G_{Ks}x_s^2(V-E_{Ks})\,, \qquad x_{s\infty} = \frac{1}{1+e^{(-5-V)/14}}\,, \qquad \tau_{xs} = \alpha_{xs}\beta_{xs}+80$$

$$\alpha_{xs} = \frac{1400}{\sqrt{1+e^{(5-V)/6}}}\,, \qquad \beta_{xs} = \frac{1}{1+e^{(V-35)/15}}$$

Calcium dynamics is ruled by:

$$I_{\text{leak}} = V_{\text{leak}}(Ca_{\text{RS}} - Ca_i)\,, \qquad I_{\text{up}} = \frac{V_{\text{maxup}}}{1 + K_{\text{up}}^2/Ca_i^2}$$

$$I_{\text{rel}} = V_{\text{rel}} O (Ca_{\text{SR}} - Ca_{\text{SS}})\,, \qquad I_{\text{xfer}} = V_{\text{xref}}(Ca_{\text{SS}} - Ca_i)$$

$$\frac{d\bar{R}}{dt} = -k_2 Ca_{\text{SS}}\bar{R} + k_4(1-\bar{R})\,, \qquad O = \frac{k_1 Ca_{\text{SS}}^2 \bar{R}}{k_3 + k_1 Ca_{\text{SS}}^2}$$

$$k_1 = \frac{k_{1'}}{k_{\text{casr}}}\,, \quad k_2 = k_{2'} k_{\text{casr}}\,, \qquad k_{casr} = \text{max}_{\text{sr}} - \frac{\text{max}_{\text{sr}} - \text{min}_{\text{sr}}}{1 + (EC/Ca_{\text{SR}})^2}$$

$$\frac{dCa_{\text{itotal}}}{dt} = -\frac{I_{bCa} + I_{pCa} - 2I_{NaCa}}{2V_c F} + \frac{V_{\text{sr}}}{V_c}(I_{\text{leak}} - I_{\text{up}}) + I_{\text{xref}}\,, \qquad Ca_{\text{ibufc}} = \frac{Ca_i \times \text{Buf}_c}{Ca_i + K_{\text{bufc}}}$$

$$\frac{dCas_{\text{SRtotal}}}{dt} = (I_{\text{up}} - I_{\text{leak}} - I_{\text{rel}})\,, \qquad Ca_{\text{srbufsr}} = \frac{Ca_{sr} \times \text{Buf}_{\text{sr}}}{Ca_{\text{SR}} + K_{\text{bufsr}}}$$

$$\frac{dCa_{\text{SStotal}}}{dt} = -\frac{I_{\text{CaL}}}{2V_{\text{ss}}F} + \frac{V_{\text{sr}}}{V_{\text{ss}}} I_{rel} - \frac{V_c}{V_{ss}} I_{xref}\,, \qquad Ca_{\text{ssbufss}} = \frac{Ca_{ss} \times \text{Buf}_{ss}}{Ca_{\text{ss}} + K_{\text{bufss}}}$$